

CALIFORNIA STATE UNIVERSITY, NORTHRIDGE

FFT APPLICATIONS TO PLANE-POLAR NEAR-FIELD ANTENNA MEASUREMENTS

A thesis submitted in partial satisfaction of the
requirements for the degree of Master of Science in

Electrical Engineering

by

Mark S. Gatti

May 1986

The Thesis of Mark S. Gatti is approved:

Dr. Yahya Rahmat-Samii

Dr. Sembiam Rengarajan

Dr. E. S. Gillespie (Chair)

California State University, Northridge

Acknowledgments

The work done on this thesis was a result of several of JPLs deep space exploration projects, particularly the Galileo project which was the main user of the near-field facility.

The managerial support of Al Brejcha, who hired me at JPL, Lee Randolph, and Harry Detweiler has been greatly appreciated over the last 6 years. I hope to always be associated with managers of this caliber.

Thanks to Guy Redenbaugh, Pat Decarolis, Bill Pickett, and Forrest Holdcraft who have helped in the implementation of the near-field range. Special thanks, to Guy Redenbaugh, who made all of the near-field measurements on the Viking antennas used in this thesis, and for his suggestions made in the course of the many measurements we have done together in the near-field facility.

I wish to express my sincere gratitude to Harry Detweiler, who spent considerable time extensively reviewing each chapter of this thesis, for keeping my goals in mind during a difficult work schedule, for allowing me the time to complete the work, and for the continual pressure to finish. Now we can keep our Monday evening racquetball appointments.

Thanks to Yahya Rahmat-Samii for making himself available during the course of the research, and code development. We had uncountable conversations which were always enlightening to me and which, I feel, added considerably more to my understanding of near-field techniques than I could ever write in the limited space of a thesis.

I appreciate the patience and understanding of my committee, who reviewed this thesis and maintained a straight face at some of the atrocious spelling errors which cropped up from time to time and who were always available when discussions were necessary.

To all of my friends who have wanted me to come out and play, thanks for waiting.

My deepest thanks to my wife and companion, Rosana. Thanks for the love and support you provided during the hard times. I would have never, never, finished this without your continual encouragement and aid. Here's to a happy, healthy family.

Table of Contents

Acknowledgements.....	iii
List of Figures.....	vi
List of Tables.....	vii
List of Symbols.....	viii
Abstract.....	xii
 Chapter 1 INTRODUCTION	
Review.....	1
The Radiating Regions About an Antenna.....	2
Planar Near-Field Measurement Techniques.....	3
Thesis Topics.....	4
Plane-Polar Measurement Technique.....	5
Computing Facility.....	6
 Chapter 2 INTERPOLATION BETWEEN POLAR AND CARTESIAN COORDINATES	
Measured Data Coordinate Systems.....	9
Selection of an Appropriate Interpolation Scheme.....	10
Implementation of the Interpolation Scheme.....	12
The Representation of the Complex Measured Data.....	14
Test Data Files.....	15
Measured Data Results.....	16
Computing Requirements.....	19
Conclusions Regarding Interpolation.....	20
 Chapter 3 CALCULATION OF THE FAR-FIELD ANTENNA PARAMETERS	
Background and Far-Field Formulations.....	33
Calculation of the Electric Field Quantities.....	35
Antenna Parameters of Interest.....	37
Results of Calculations Using the FFT.....	39

	Computer Resources.....	40
	Conclusions.....	41
Chapter 4	PARABOLIC REFLECTOR SURFACE DIAGNOSIS FROM NEAR-FIELD MEASUREMENTS	
	Introduction.....	50
	Surface Diagnosis Formulation.....	50
	Implementation.....	53
	Test Case Results.....	54
	Conclusions.....	56
Chapter 5	THESIS CONCLUSIONS	
	Interpolation Results.....	63
	Calculation of the Far-Field Parameters.....	64
	Diagnosis.....	65
	Summary.....	66
	References.....	67
Appendix A	THE BIVARIATE LAGRANGE INTERPOLATION	
	Interpolation Requirements.....	69
	1-Dimensional Interpolation.....	69
	2-Dimensional Interpolation.....	71
Appendix B	FFT ALGORITHMS USED IN ANTENNA CALCULATIONS	
	FFT Algorithms.....	73
	FFT Implementations.....	74
	The 2-Dimensional CFT.....	75
	Interpolation.....	76
	Sampling Criteria.....	78

List of Figures

Figure 1.1a	Illustration of the Distances from an Aperture in the x-y plane to a Point P in Space.....	7
Figure 1.1b	The definitions of the Three Regions Surrounding a Radiating Aperture....	7
Figure 1.2	The Plane-Polar Near-Field Data Acquisition Configuration.....	8
Figure 2.1	The Coordinate System Used for Plane-Polar Measurement.....	21
Figure 2.2	Rectangular Coordinate System for Interpolation.....	22
Figure 2.3	The Three Regions of Interest Regarding the Interpolation to Rectangular Coordinates.....	23
Figure 2.4	Results of interpolating on the Real and Imaginary Parts of the Field Shown is the Amplitude of the Real and Imaginary Parts for the Cut Along the X-axis.....	24
Figure 2.5	Results of Interpolating on the Real and Imaginary Parts of the Field Shown is the Magnitude and Phase Parts for the Cut Along the X-axis.....	25
Figure 2.6	Results of Interpolating on the Magnitude and Phase Parts of the Field Shown is the Amplitude of the Real and Imaginary Parts for the Cut Along the X-axis.....	26
Figure 2.7	Results of Interpolating on the Magnitude and Phase Parts of the Field Shown is the Magnitude and Phase Parts for the Cut Along the X-axis.....	27
Figure 2.8	Results of Interpolating on the Real and Imaginary Parts of the Field Shown is the Amplitude of the Real and Imaginary Parts for the Cut Along the Y-axis.....	28
Figure 2.9	Results of Interpolating on the Real and Imaginary Parts of the Field Shown is the Magnitude and Phase Parts for the Cut Along the Y-axis.....	29
Figure 2.10	Results of Interpolating on the Magnitude and Phase Parts of the Field Shown is the Amplitude of the Real and Imaginary Parts for the Cut Along the Y-axis.....	30
Figure 2.11	Results of Interpolating on the Magnitude and Phase Parts of the Field Shown is the Magnitude and Phase Parts for the Cut Along the Y-axis.....	31
Figure 2.12	The Number of Scans-vs-Time to Perform the Interpolation.....	32
Figure 3.1	Coordinate System for Pattern Calculation and Data Acquisition.....	43
Figure 3.2a	x-y Near-Field Coordinate System.....	44
Figure 3.2b	u-v Far-Field Coordinate System.....	44
Figure 3.3	Magnitude and Phase Plots for the Viking HGA Co-polarized Components - Comparisons Between FFT and Jacobi-Bessel for the $\phi = 0^\circ$ Cut.....	45

Figure 3.4	Magnitude and Phase Plots for the Viking HGA Cross-polarized Components - Comparisons Between FFT and Jacobi-Bessel for the $\phi = 0^\circ$ Cut.....	46
Figure 3.5	Axial Ratio and Tilt Angle for the Viking HGA - Comparisons Between FFT and Jacobi-Bessel for the $\phi = 0^\circ$ Cut.....	47
Figure 3.6	Pictorial Description of the Maximum Value of Theta for Which the Fields are Accurate.....	48
Figure 3.7	Total Time to Calculate the Field Pattern-vs-the Number of Scans: 101 pts.....	49
Figure 4.1	The Coordinate System Used to Define the Far-Field Quantity $T(u,v)$	57
Figure 4.2	The Description of the Surface Error of a Parabolic Reflector.....	57
Figure 4.3	Illustration of the Test Case Showing the Constant Distortions in the Phase, the Maximum Distance of the Measurement and the Square Window Which is viewed in the Figures 4.4 to 4.7.....	58
Figure 4.4	Phase of the Raw Data in the Measurement Plane for the Uniform Test Case.....	59
Figure 4.5	Phase of the Data After the IFFT for the Uniform Test Case.....	60
Figure 4.6	Phase Corrected for Quadratic Errors for the Uniform Test Case.....	61
Figure 4.7	Distortion of the Reflector in Wavelengths for the Uniform Test Case.....	62
Figure A1	The Coordinate System Used for the Bivariate Lagrange Interpolation.....	72
Figure B1	A Continuous Function $f(x)$ Limited in Range to $[-a,a]$ and its Continuous Fourier Transform, Essentially Bandlimited to $[-\alpha,\alpha]$	79
Figure B2	Sampled Versions of the Continuous Functions $f(x)$ and $F(u)$	79
Figure B3	A Causal Function $g(x)$ and its Sampled Version $g(n\Delta x)$	80
Figure B4	A Fourier Transform and its Neighboring Aliases.....	80
Figure B5	The Effects of Aliasing Error on a Fourier Transform Due to Large Sample Size Δx	80

List of Tables

Table 3.1	Total Execution Times to Calculate Field Patterns (min:sec).....	41
Table B1	Relationship Between the FFT Parameters x and u	74

List of Symbols

(In order of appearance in each chapter)

Chapter 1

- P: A specific point in the far-field of a radiating aperture
R: The distance from the phase center of the radiating aperture and the point P
 r_1 : The distance from the first point in the aperture to the point P
 r_2 : The distance from the second point in the aperture to the point P
 λ : The wavelength of the electromagnetic field being measured

Chapter 2

- H_r : The radial component of the magnetic field measured in the near field
 H_ϕ : The circumferential component of the magnetic field measured in the near field
 H_x : The x component of the magnetic field measured in the near field
 H_y : The y component of the magnetic field measured in the near field
 p : The integer which defines the size of the FFT - 2^p
 r : The distance from the center of the coordinate system to the point in question
 r_{max} : The distance from the center of the coordinate system to the last ring of plane-polar measured data
 r_{min} : The distance from the center of the coordinate system to the first ring of plane-polar measured data
 λ : The wavelength of the electromagnetic field being measured
 ϕ : The angle measured from the x-axis of the near-field coordinate system to the measured point in question
 x : The Cartesian coordinate of the point in question along the x-axis
 y : The Cartesian coordinate of the point in question along the y-axis
 Δx : The incremental distance between scans of interpolated data in the x direction
 Δy : The incremental distance between scans of interpolated data in the y direction
 x_{max_m} : The maximum distance in the x direction that measured plane-polar data exists
 y_{max_m} : The maximum distance in the y direction that measured plane-polar data exists

Chapter 3

- \vec{E}_a : The electric field vector quantity of the antenna under test in the far field
- \vec{H}_a : The magnetic field vector quantity of the antenna under test in the far field
- \vec{H} : The magnetic field vector quantity of the measured data in the near field
- $\vec{q}_m(\vec{p})$: The surface current quantity of the measured data in the plane of the measured data = $2\vec{h} \times \vec{H}$ for this thesis
- \vec{h} : The unit normal to the plane of the measured data
- \hat{r} : The unit vector in the direction of the far-field point in question
- \vec{r} : The vector of the far-field point in question
- \hat{x} : The Cartesian direction vector for the x-axis
- \hat{y} : The Cartesian direction vector for the y-axis
- \hat{z} : The Cartesian direction vector for the z-axis
- x : The Cartesian coordinate of the point in question along the x-axis
- y : The Cartesian coordinate of the point in question along the y-axis
- z : The Cartesian coordinate of the point in question along the z-axis
- Δx : The incremental distance between scans of interpolated data in the x direction
- Δy : The incremental distance between scans of interpolated data in the y direction
- \vec{p} : The vector from the origin of the coordinate system to a measured point in the measurement plane
- θ : The angle between the \hat{z} axis and the far-field point in question
- ϕ : The angle between the \hat{x} axis and the projection onto the xy-plane of the far-field point in question
- $E_{a\theta}$: The θ component of the far field of the antenna under test
- $E_{a\phi}$: The ϕ component of the far field of the antenna under test
- $E_{p\phi}^v$: The ϕ component of the probe pattern for the v orientation (x-axis)
- $E_{p\theta}^v$: The θ component of the probe pattern for the v orientation (y-axis)
- u : The transform variable for the use of the FFT corresponding to the x direction
- v : The transform variable for the use of the FFT corresponding to the y direction
- k : The wavenumber of the field = $2\pi/\lambda$
- $T(u, v)$: The far-field quantity of the output from the FFT of the near-field data

- $T_x(\theta, \phi)$: The x component of the $T(u, v)$ quantity calculated by the FFT sinc-sinc interpolation at the point defined by (θ, ϕ)
- $T_y(\theta, \phi)$: The y component of the $T(u, v)$ quantity calculated by the FFT sinc-sinc interpolation at the point defined by (θ, ϕ)
- L_x : The maximum distance in the measurement plane for which data is available
- D_x : The diameter of the antenna under test
- d : The distance from the plane of the reflector to the measurement plane
- θ_0 : The maximum angle from the z-axis for which the far-field data will be accurate
- dB : Decibel - a power ratio, raised to the tenth power

Chapter 4

- $T(u, v)$: The far-field quantity of the output from the FFT of the near-field data
- $J(x', y')$: A function in the scan plane which is related to the surface currents of the reflector
- k : The wavenumber of the field $= 2\pi/\lambda$
- λ : The frequency of the electromagnetic field being measured
- z' : The distance from the top of the distortion to the focal plane of the reflector
- x' : The Cartesian component of the distance to the point in the focal plane along the x-axis
- y' : The Cartesian component of the distance to the point in the focal plane along the y-axis
- r' : The distance from the phase center to the reflector surface
- F : The focal distance of the parabolic reflector
- ϵ : The magnitude of the distortion on the surface of the reflector
- ζ : $1/2$ of the angle between the z-axis of the reflector and the distortion in question on the reflector
- δ : The total phase error due to the distortion on the reflector surface
- $F\{\}$: The Fourier transform operator
- u : The transform variable for the use of the FFT corresponding to the x direction
- v : The transform variable for the use of the FFT corresponding to the y direction
- z_0 : The distance between the focal plane of the reflector and the scan plane of the measured near field data.

- Δx : The incremental distance between scans of interpolated data in the x direction
- Δy : The incremental distance between scans of interpolated data in the y direction
- u_{\max} : The maximum value of u in the uv -plane output from the FFT
- v_{\max} : The maximum value of v in the uv -plane output from the FFT
- θ : The angle between the z axis and the far-field point in question
- ϕ : The angle between the x axis and the projection onto the xy -plane of the far-field point in question
- p' : The point on the surface distortion which intercepts the incident geometrical optics ray
- p : The point on the surface of the reflector which would intercept the geometrical optics ray in the absence of the distortion
- q : The point on the surface distortion which reflects the geometrical optics ray
- r : The radius from the coordinate center to a measured near-field point
- ψ : The phase of the near-field data in the scan plane of the measured data
- H_x : The x component of the magnetic field measured in the near field
- H_y : The y component of the magnetic field measured in the near field

Thesis Abstract

FFT Applications to Plane-Polar Near-Field Antenna Measurements

by

Mark S. Gatti

Master of Science in Electrical Engineering

The Jet Propulsion Laboratory has built a near field antenna measurement facility based on the plane-polar measurement technique which utilizes the Jacobi-Bessel transform for the pattern analysis. This technique is useful because one can very accurately and easily measure antennas which are only slightly smaller than the available room size. This thesis develops the algorithms necessary so that the data measured on the plane-polar facility can be reduced by the use of the Fast Fourier Transform (FFT), which enhances many aspects of antenna pattern calculation from near field measurements. Furthermore, these tools are extended to include the calculation of the surface distortion of a parabolic antenna. This diagnosis technique can prove useful in mapping the contours of surface errors such that a designer may attempt to improve the antenna performance.

The results of applying the FFT to the analysis of polar data show promise in that the accuracy is maintained for greater angles of interest. Also, for principal plane patterns the computer resources required in terms of CPU execution time are much less than the Jacobi-Bessel technique. The areas of savings are a direct result of integrating the radiation integral by the FFT. The results of this technique are compared to those of the Jacobi-Bessel technique, and advantages and disadvantages are compared.

Chapter 1

INTRODUCTION

Review

The characterization of an antenna's radiation properties is a very important part of the antenna engineer's task once a design has been turned into hardware. These radiation properties are often measured on far-field ranges which are built outdoors and are often subject to unfavorable conditions. These conditions include the limited range size, or the need for a large amount of real estate, the ability to isolate the test antenna from the effects of the weather, the ability to define the antenna performance completely, and the interference caused to the measurement by the weather conditions. These concerns may be eliminated by the use of near-field measurement techniques in which the fields of the antenna under test are measured by a probe in the near-field region of the antenna. By using near-field techniques, the antenna engineer may characterize the entire antenna pattern and not just several cuts, and the results can be as accurate or better than the results of far-field measurements if the near field range is built indoors. Accurate measurements may continue to be made during any weather conditions without delaying the test schedule. The problems associated with the near-field techniques are that a more complicated measurement system is required, since the phase and magnitude of the field must be measured, that computing the far field is more difficult than in far-field measurements, and that the final results may not be determined in real time as the measurements occur.

Near-field techniques have come to be used to measure the far-field parameters of antennas which are sensitive to the effects of gravity, such as spacecraft antennas, antennas which must not be exposed to inclement weather, and antennas which are classified for security purposes. For these reasons and others, many researchers have shown an interest in this technique which has been included in the IEEE Standard Test Procedures for Antennas [1979], and which has been thoroughly reviewed by Johnson, Ecker and

Hollis [1973], Appel-Hansen [1982], and more recently by Yaghjian [1986]. In these reviews, three different near-field techniques are discussed, each of which are referred to by the coordinate system in which the data is acquired: planar, cylindrical, and spherical. Of these three types of near-field measurement systems, the planar technique has been the most widely used. This popularity results from several reasons, among which is the fact that the coordinate system is simple to work with, it fits the geometry of many high gain antennas, and a great deal of analysis has been done to understand the various errors involved in the formulations [Yaghjian, 1975].

The far-field patterns of an antenna may be calculated from the near-field measurements in one of several ways. The most widely used technique is that of the modal expansion method which was pioneered by Kerns [1950, 1960, 1981]. This technique uses data measured on a plane in a Cartesian coordinate system. The modal expansion method was soon afterward expanded to account for the effects of the probe on the measured data [Joy, Leach, Rodrigue, and Paris, 1978, and Paris, Leach, and Joy, 1973, 1978]. The near-field ranges which are now widely used are usually based on these techniques since much data has been published describing the results, analytical techniques, and error bounds [Baird, Newell, Wacker, Kerns, 1970].

The Radiating Regions About an Antenna

The definition of the near-field of an antenna is discussed by Johnson, et. al., [1973]. In that paper the terms which are preferred for definitions are the reactive near-field, the radiating near-field, and the radiating far-field. The authors of that paper prefer to use the terms reactive near field, radiating near field, and radiating far field to describe the regions about a radiating element or aperture and to reserve the terms Fresnel and Fraunhofer to describe the approximations used in various analytical techniques. This is because Fresnel and Fraunhofer are terms which come from optics, which have no region similar to the reactive near field. Figure 1.1 illustrates the definitions of the various regions. In Figure 1.1a,

a planar aperture distribution is given in the xy -plane and the point P is separated from the center of the coordinate system by a distance R . The field at the point P is given by the superposition of every radiating element in the aperture, which is an integral in the case of a continuous aperture. In this figure, the distances r_1 and r_2 are seen to change by significantly different amounts as P moves farther away in a fixed direction. Thus, the phase between these points changes significantly. This can be shown for all points in the aperture and thus the radiation pattern will depend on the radius to the observation point. However, at large distances r_1 and r_2 are approximately parallel and do not differ in relative length as P moves away in a fixed direction. Therefore, the pattern is not visibly dependent on the distance R as P moves away in a fixed direction. It is at this point that P is in the far-field of the aperture. Thus the far-field of the aperture is that distance at which the patterns of the antenna no longer change shape as a function of distance from the aperture. Figure 1.1b illustrates the distances defining the three regions for antenna measurements.

Planar Near-Field Measurement Techniques

In the planar near-field measurement technique, the field data is acquired on a plane which is finite in extent but which intercepts the major portion of the radiating field. This data is then used to calculate the far-field quantities of the antenna under test. There are basically two ways to calculate the far-field patterns from the near-field measurements: 1) by using the complete electromagnetic fields surrounding the antenna, called the source distribution method, and 2) by using a modal expansion technique as mentioned in the previous section. In the source distribution method, the probe used to measure the fields must be small with respect to the wavelength and the antenna under test, but there is no means to compensate for the effects of the probe. In the modal expansion technique, the pattern of the probe is transformed to obtain a modal expansion in terms of wavenumbers. Thus, the effects of the probe may be eliminated on a term-by-term basis from the modal expansion. The modal expansion technique has an advantage in that information is obtained which is useful in the calculation of errors and in the elimination of secondary probe/test antenna interactions.

Rahmat-Samii, Galindo-Israel, and Mittra [1980] have devised a technique by which the near-field data is measured in a plane on concentric rings. This is referred to as the plane-polar technique and utilizes a Jacobi-Bessel expansion to describe the far-fields. This technique begins as the modal expansion technique does, with the Lorentz reciprocity theorem, but then a convolutional expression of the antenna pattern and the probe pattern is developed from which a radiation type integral is derived. This integral is similar in form to the first term of the modal expansion as described above and is a Fourier transform. The integral is expanded by the Jacobi-Bessel expansion and the coefficients are found which are used to describe the far-field pattern. Since the equation resulting from the convolution expression is equal to the first term of the modal expansion, the use of probe compensation in the Jacobi-Bessel technique has the same form as used by the modal expansion technique. An alternate algorithm to the solution of the integral expression has been recently given by Bennett [1985] which is based on the use of the Fast Fourier Transform operating on each ring of data.

The plane-polar data acquisition technique is useful for several reasons, among which are the ability to limit the motion of the probe to a single direction, the ability to maintain a uniform load due to gravity on the antenna under test, and that the size of the antenna under test may be large compared to the facility used to measure the data. Figure 1.2 shows the measurement geometry of a plane-polar facility. The data acquired in this facility consists of the measured fields on concentric rings, each of which is evenly spaced from its neighboring rings. One such facility has been developed at the Jet Propulsion Laboratory (JPL) and has proven useful in the measurement of large spacecraft antennas [Rahmat-Samii, and Gatti, 1985].

Thesis Topics

This thesis is concerned with the calculations of the far-field patterns from measured data on a plane-polar coordinate system using alternate techniques than the Jacobi-Bessel technique. Because of the interest in the plane-polar data acquisition technique, it has

been suggested that alternate methods to reduce the data be investigated, particularly the use of the 2-dimensional Fast Fourier Transform (FFT) in the evaluation of the radiation type integral that results from the convolution expression mentioned above. The ability to use near-field data to estimate the distortions on the surface of a parabolic antenna has also been suggested [Rahmat-Samii, 1984] since the FFT has a direct application to this type of analysis. In order to use the FFT algorithms, the data must lie on a rectangular grid system which is related to the x-y coordinate system of the near-field facility. Chapter 2 develops an interpolation which is required to transform the data from a polar to a Cartesian coordinate system. Comparisons between the measured data and the interpolated data are given for the principal plane cuts of the near-field coordinate system. Chapter 3 develops the FFT approach which is used to calculate the patterns of the antenna under test and the results are compared to those of the Jacobi-Bessel technique. Chapter 4 addresses the possibility of using the near-field data in calculating the surface errors of parabolic antennas. An algorithm which uses the FFT techniques from Chapter 3 is conceived and presented which may prove useful in the surface error calculations. Results of applying this algorithm are given for a specific test case. The usefulness of the FFT in this application is that its output provides the far-field information in the particular coordinate system required to begin a surface diagnosis of the reflector.

Plane-Polar Measurement Technique

Since this thesis is using a variation of the techniques described by Rahmat-Samii, et. al., [1980], and the Jet Propulsion Laboratory's plane-polar measurement facility is used to acquire the near-field data, a description of the acquisition technique will be useful. The measurement facility is configured as shown in Figure 1.2 where the antenna under test rotates about the z-axis. For large probes, it may be necessary to also rotate the probe as the antenna rotates to allow for probe compensation. The probe is positioned above the antenna under test and will move in one direction along the x-axis. Measurements are taken when the probe is stationed at a fixed distance on the x-axis and the antenna under test

rotates 360° . The probe then moves to the next location, usually $1/2\lambda$ from the last location, and the process is repeated. A complete data set thus consists of field values measured on concentric rings in the measurement plane. This data may be directly used in the subsequent analysis of the far-field parameters using the Jacobi-Bessel techniques as discussed in Chapter 3.

Computing Facility

In order to calculate the far-field parameters of the antenna under test, a computing facility must be available which has the capability to store large amounts of data and that will execute large programs efficiently. Many comparisons are made in the literature which state the various speeds, storage requirements, accuracies, and other computing resources which are obtained by certain algorithms. These comparisons must be set in the proper perspective. For this thesis, the computing facility which is used is a UNIVAC 1180, which has a 36 bit word size, and the programs are written in ASCII FORTRAN 77.

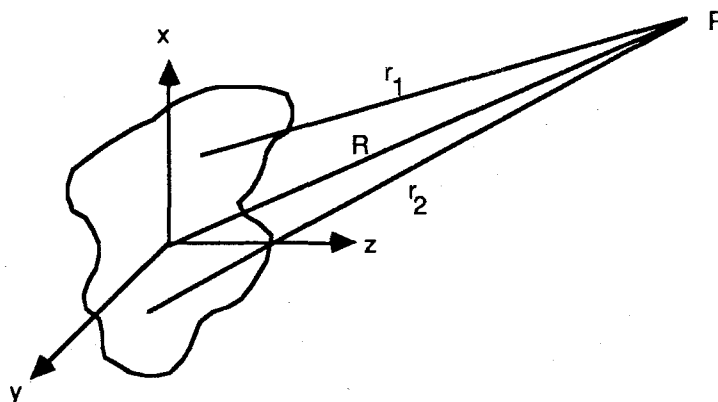


Figure 1.1a Illustration of the Distances from an Aperture in the x-y Plane to a Point P in Space

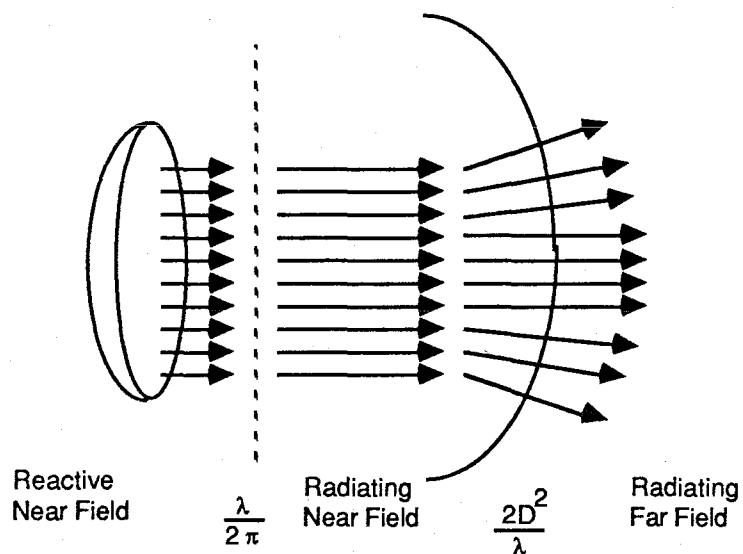


Figure 1.1b The Definitions of the Three Regions Surrounding a Radiating Aperture

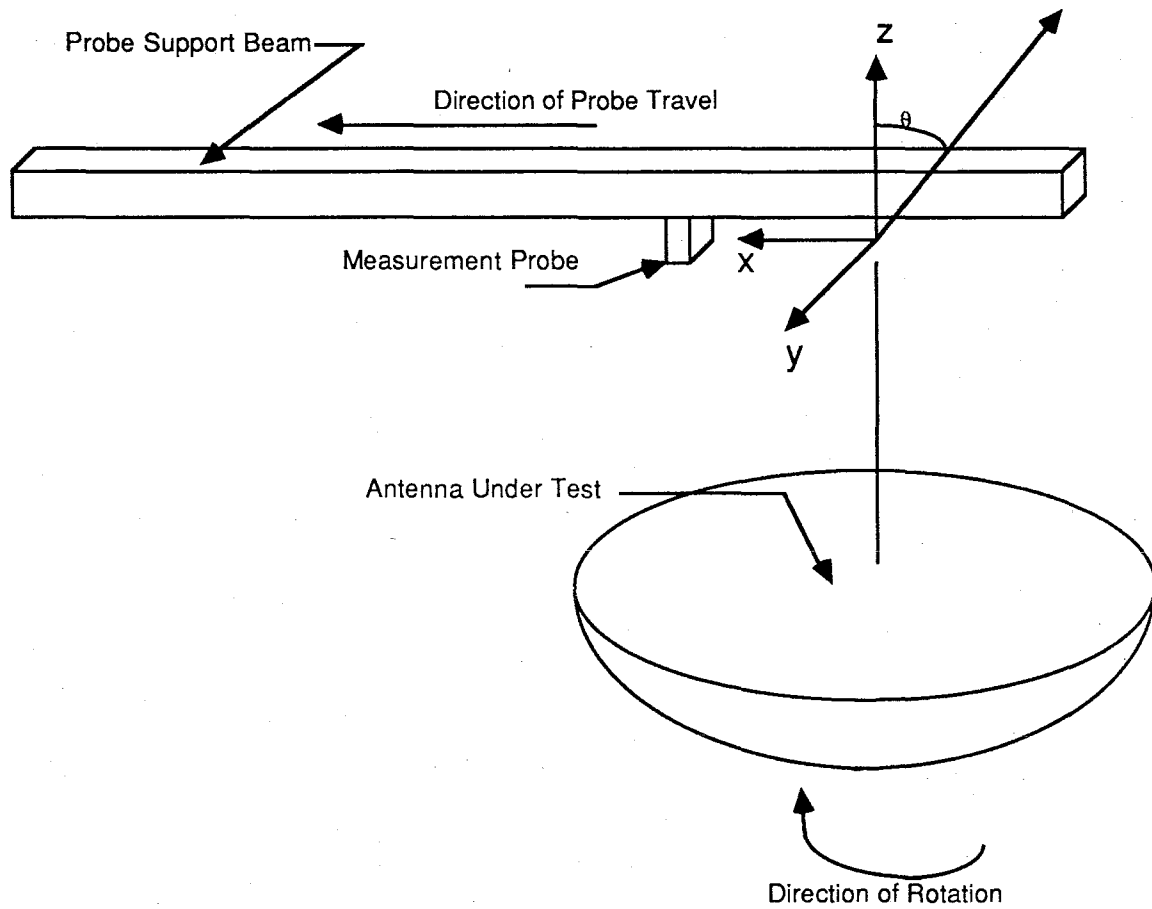


Figure 1.2 The Plane-Polar Near-Field Data Acquisition Configuration

Chapter 2

INTERPOLATION BETWEEN POLAR AND CARTESIAN COORDINATES

Measured Data Coordinate Systems

The near-field data, as obtained from the plane-polar measurement facility at JPL, consists of two complete sets of data for two independent probes. These independent probes are actually two orthogonal positions of the same probe. The two sets of data are required in order to reconstruct the far-field quantities of the test antenna as described in Chapter 3. Each data set consists of the field values measured on concentric rings of a given spacing for both the amplitude and phase of the measured field. Figure 2.1 shows the coordinate system for the measured data. The data measured is proportional to the magnetic field components H_r and H_ϕ . This data is then transformed from the polar to the Cartesian components H_x and H_y required for use by the plane-polar algorithms. Each ring typically consists of 901 points of data evenly spaced between $\phi = 0^\circ$ and 360° , inclusive. The spacing between rings is uniform except for the first ring, which is of a radius approximately $1/4 \lambda$ about the coordinate center. Obviously, the field for the inner rings is very oversampled when compared to the $1/2 \lambda$ criterion as described in Appendix B and by Joy and Paris [1972] for the efficient use of FFTs. However, the measurement algorithm is simplified by this technique since every ring of data is acquired by the same sampling routine. There is no increase in acquisition time since the antenna under test must rotate a full 360° regardless of the radius of the ring. As the outer rings are approached, one can see that the sampling is approaching or, depending on the distance to the outermost ring, exceeding the $1/2 \lambda$ requirement described in Appendix B for the use of the FFT. The Jacobi-Bessel algorithm employed by Rahmat-Samii, Galindo-Israel, and Mittra, [1980] was implemented on the JPL UNIVAC in such a way as to ignore the unnecessary data in the innermost rings and to use increasingly more data in the outermost rings.

In order to utilize the FFT routines, the measured data must lie on a rectangular grid system in the measurement plane and be expressed as H_x and H_y . This grid system will have a uniform spacing between the points on the grid in both the x and y directions. It is critical that this spacing be uniform for a given direction so that the FFT may be properly used; however, the spacing in one direction is allowed to be different than that in the orthogonal direction. This is because the FFT will integrate along one direction first and then perform the integration in the orthogonal direction. Appendix B illustrates the technique of combining two 1-dimensional FFTs to obtain the 2-dimensional Fourier Transform. Figure 2.2 shows the rectangular coordinate system which will be the basis for the following discussions. This figure also shows the boundaries of the measured data from the polar coordinates. Notice that the maximum values in the x and y directions, x_{\max_m} and y_{\max_m} , are limited to be equal to or less than the maximum distance to the outermost ring. This is because there are no values of the field beyond the last ring. As will be shown later, the four corners of this rectangular region will be filled with zeroes for the function value.

Selection of an Appropriate Interpolation Scheme

The situation was thus one of the incompatibility between the polar coordinate system that the data was measured on and the coordinate system used by the FFT algorithm to reduce that data. In particular, one must somehow interpolate the measured polar data onto a rectangular coordinate system. It is necessary that the interpolation meet certain requirements. These are:

- 1) Simplicity,
- 2) Efficiency,
- 3) Accuracy, and
- 4) Reduce to the value of the point at a point which is one of the original given .

The reason for the requirements of simplicity and efficiency are that there will be a large amount of data to interpolate. For example, if there are 63 rings of data, each of which

consisting of 901 points, then one would have to store, look up, and work with 113,526 data points. There is a factor of two included for the two independent measurements. The data is complex valued and thus the computer storage is twice as many words as data points. The accuracy requirement is self evident; the object of the thesis will be compromised if the interpolation is inaccurate. Also note that any interpolation, which is to be a viable candidate, will have to be able to recover the value of the data point when that point is chosen. If this last requirement is ignored, then the interpolation will have built in errors. The interpolation techniques which were investigated were the bivariate Lagrange and the cubic spline [Abramowitz and Stegun, 1964, Ferziger 1981, and Ngai and Profera, 1984]. These techniques are discussed in Appendix A. For the bivariate Lagrange interpolation there is a choice to be made; does one choose a simple linear bivariate interpolation, also known as the 4-point bivariate, or does one choose a higher order bivariate?

The choice for the interpolation is made according to the requirements mentioned above. The cubic spline is very accurate; however, it requires special treatment for the end points [Ferziger, 1981, p. 9] which occur at the edges of the rectangle defining the measurement plane. There has to be continuity in the derivatives at the endpoints for this interpolation to be satisfactory. Since the field will drop abruptly to zero past the outermost ring, one would have to write a special software routine to calculate the derivatives in order to handle this. Sometimes other problems occur which may cause the fit obtained by the spline to "wiggle". The cure would be to use the tension spline in which case the simplicity requirement is breached. For these reasons the spline has been eliminated from further consideration for the purposes of this thesis.

The remaining technique is the bivariate Lagrange interpolation. This technique meets all of the requirements given for an acceptable interpolation routine. An n -point interpolation is only slightly different than the 4-point interpolation. In fact, the latter is a subset of the former. The advantages of using the 4-point interpolation are that the routine will run more quickly compared to higher order forms on the UNIVAC mainframe and may be

more easily implemented. The 4-point technique is used in many areas of interest in antenna related problems [Ngai and Profera, 1984]. In addition, the n-point scheme could cause the implementation difficulties previously mentioned for the spline case for the values near the boundaries. It is shown in Appendix A that the Lagrange interpolation algorithm will recover the value of the function at point where the value is known.

For the reasons of simplicity, efficiency, accuracy and function value return, the 4-point bivariate Lagrange interpolation routine was selected as the routine for the completion of the thesis. Future references to an interpolation scheme refer specifically to the 4-point Lagrange.

Implementation of the Interpolation Scheme

The 4-point Lagrange interpolation algorithm, as discussed in Appendix A, was implemented in FORTRAN on the JPL UNIVAC mainframe. The data to be interpolated exist in a file which was created by a software package written for the plane-polar algorithms. In addition to converting the data to H_x and H_y , this software package converts the complex number representation of the data from the polar form to the Cartesian form, which consists of a real and an imaginary part, by making use of Euler's equations. This was done since the FORTRAN compiler is readily adaptable for use with complex numbers of that form. The FFT algorithm which was used for the integration of the data was also set up to work with this format for a complex number.

For an interpolation routine to work efficiently, the data must be rapidly accessible. This means that if the value of the function at a particular point is desired, one should be able to look that value up directly by the use of various computer lookup indices. In the UNIVAC FORTRAN there are two solutions to the accessibility problem: direct access disk files and arrays in virtual memory. The data in the file from the plane-polar measurements are in a direct access file where each ring of data for both H_x and H_y comprises one record. This meant that a given ring could be directly accessed; but, a particular point would have to be looked up in the given ring. Because direct access files are simple to store, a second file was created

where each record consists of an (H_x, H_y) pair. A lookup scheme was derived so that the program could quickly access a particular point given the radius and angle. The alternative was to read the entire file into data arrays which are in virtual memory. This option would decrease the execution time of the routine at the cost of a larger memory requirement, and therefore a more complex program, since the FORTRAN virtual memory features would have to be used. The execution times for the interpolation based on the use of direct access files will be discussed later; however, one should be aware that quicker interpolations would be obtained by using the virtual memory features.

Assuming that a suitable method exists to access the data one must perform the interpolation to a given rectangular grid system. This grid system is shown in Figure 2.2. Here, x_{\max_m} and y_{\max_m} are chosen as the maximum distances for which measured data exists. In the plane-polar system these distances are equal since the data are in circular format. By selecting these distances to be no larger than the outermost ring of measured data the number of points which must be interpolated is minimized. Given this distance, one may select the Δx and Δy to fully define the measurement plane. The number of scans in each direction is an arbitrary, odd number since the grid is square and the $x = 0$ and $y = 0$ scans are included. For the FFT routine used in this thesis to work, the number of scans must be an integer which is equal to 2^p , where p is an integer. Clearly, the number of measured/interpolated scans do not equal an integer of this type. This situation poses no real problem because the FFT will return accurate results for a given case provided zeros are appended around the entire measurement plane to make the number of scans for the interpolation area equal to an integer 2^p . This is called zero fill and is discussed in Oppenheim and Schaffer, [1975], Rabiner and Gold, [1975] and is the typical technique for satisfying the 2^p requirement. With reference to Figure 2.2, the entire data set which is integrated by the FFT then becomes that region defined by the distances x_{\max_f} and y_{\max_f} , where the subscript f refers to the FFT distance.

With the coordinate system defined as in Figure 2.1, one begins to calculate the values of the measured field along the grid. There are three regions of interest as defined in figure 2.3:

- 1) $r > r_{\max}$,
- 2) $r_{\min} \leq r \leq r_{\max}$,
- 3) $r < r_{\min}$.

The first region is the simple case; the field values along grid points where $r > r_{\max}$ are set equal to zero. The second region is the next in simplicity; here one chooses the rings which bound the point in radius and then finds the two points on each ring which bound it in the angle ϕ , measured from the x-axis. The location of these four points in terms of r and ϕ , and their field values, are passed to the interpolation routine with the result being the value at the desired grid location. For this case it is essential that the spatial description of the field values being interpolated are expressed in terms of r and ϕ . Then one can visualize that the four points represent the four surrounding points in r - ϕ space, along constant lines of r and ϕ , and the application of the bivariate interpolation can be justified [Appendix A, Figure A1]. The third region is a special case; there are not two rings which bound the point of interest. In this case the points chosen to perform the interpolation are those two on the innermost ring which bound the desired point in ϕ and the point at the origin. This is observed to be a degenerate version of case 2, where the point at the origin represents a multiple point on the "inner" ring. It is apparent that the only areas for which $r > r_{\max}$ are the four corners of the measurement grid. It would be simple to increase the interpolation grid to x_{\max_f} or y_{\max_f} and to fill the field values with zeroes beyond the outermost ring, but this would only cause the interpolation to take longer. The increase in grid size was done in the software which calculates the FFT and subsequent far-field quantities.

The Representation of the Complex Measured Data

It was discussed earlier that the data was represented in the computer in the Cartesian form of complex numbers. The interpolation was done on the data in this form.

However, the interpolation was also performed on the the amplitude and phase of the complex field value in polar form. The interpolation will yield different answers for each of these cases since the relationship is nonlinear between the interpolated quantities in the polar form and linear in the case of the Cartesian form. The concern is over the representation to choose. Consider that the data in raw form is measured by a receiving system which returns amplitude and phase. The Cartesian representation occurred in the routine which converted the data to a file usable by the UNIVAC. Possibly it would be more appropriate to interpolate the amplitude and phase for this reason. Conversely, all of the data will be changed to a real and imaginary representation for use by all the subsequent FORTRAN routines. In this case there may be an ambiguity from interpolation in amplitude and phase for data which will be handled as real and imaginary. This situation is addressed and resolved in the section which discusses the results of the interpolation on test and measured data.

Test Data Files

In order to write, debug, verify and test the software routines which were generated, it would be convenient to have a data file which represents a known radiation field. This data file can be any set of measured data from one of the many available from the JPL near-field range, or it can be a simple simulated field which is generated by the computer. The advantage of a simulated field was that any small problems which occur would be the result of the interpolation algorithm and not of the measured data. However, a simulated field will not yield substantial information regarding the overall accuracy of the interpolation routine.

The simplest simulated field is that of a uniform amplitude with the orthogonal components of the field being in phase quadrature. For example, if the field is given by:

(2.1)

$$H_x = 1/\sqrt{2} + j0$$

$$H_y = 0 - j/\sqrt{2} = H_x e^{-j\pi/2},$$

then the resultant far field would be a right-hand circularly polarized field with a peak value equal to the area of the circle defined by the outermost ring. This file could be used to examine the computing requirements of all the subsequent software routines with respect to time, storage, and data handling, and still yield some information regarding accuracy. A FORTRAN program was written to generate this simple test field. This program allowed the user to vary the number of rings of data. Throughout the course of the thesis study, this program was used to generate the test fields used to perform various timing runs, etc.

The second type of test data was obtained from actual measurements from the Viking Project High Gain Antenna (HGA), during the Galileo antenna testing. The data consists of 63 rings of 901 points apiece for both H_x and H_y , at an operating frequency of 8.415 GHz. This particular HGA has been used continually over the last five years and is well characterized in both the far-field and the near-field. It is known that the antenna radiates a field which is right elliptical polarized at the operating frequency. The antenna was used to provide the evidence that the Jacobi-Bessel near-field reduction technique was correct. Many different comparisons between the far-field and near-field using this antenna were made and very good results were obtained. Therefore, a comparison between the far-field patterns as calculated by the Jacobi-Bessel and the FFT algorithms can be made to evaluate the performance of the FFT algorithm.

Measured Data Results

The computer programs were generated to perform the interpolation in accordance with the interpolation technique described in the previous section. The program was tested with the simulated uniform test case and the Viking HGA. The results of the simple simulated test case showed that the routine performed the algorithm to completion and that the amplitude and phase of the results matched that of the input file. This indicated that the algorithm was ready to be applied to the measured Viking HGA data.

The Viking Data was interpolated and checked by comparing the resulting data on the rectangular coordinates to the given data on the concentric rings. The comparison was

made on the $\phi = 0^\circ$ and 90° scans (x and y axes) in the measurement plane. These particular scans were chosen because each coordinate system lines up at this orientation and it is an easy matter to display the results accordingly.

The following questions are of interest in making the comparisons:

- 1) How does the data compare as a function of distance from the center of the coordinate system?
- 2) Which is the better complex number representation to interpolate - that of the Cartesian or polar form?
- 3) Was the coordinate system of the software properly aligned with that of the measured data?
- 4) Does the output match better if the real and imaginary parts are displayed or if the amplitude and phase parts are displayed?
- 5) What is the computer execution time as a function of the number of scans?

With the above questions in mind, a systematic approach can be made in the data processing. The data was interpolated twice; once by using the real and imaginary parts of the complex field values, and once by using the amplitude and phase parts of the same field values. For each of these test runs the data is displayed on a plot of the quantity in question - vs - the distance from the center of the coordinate system. The quantity in question will be the real and imaginary parts, or the amplitude and phase parts of the fields. This approach was followed for both of the principal axes and the results are given in Figures 2.4 - 2.11. In these figures are plotted two curves, each of which is independent. One curve is generated by plotting the interpolated field value at the scan locations along the x or y axis, and the other curve is generated by plotting the measured field value at the ring locations in the $\phi=0^\circ$ or 90° direction. The ring spacing does not necessarily equal the grid spacing, so the points plotted for each curve do not necessarily occur at the same value of distance from the center of the coordinate system.

Figures 2.4 and 2.5 show the real and imaginary parts of the H_x field for the $\phi=0^\circ$ scan. However, Figure 2.4 shows the field as the result of an interpolation on the real and imaginary parts of the input data, and Figure 2.5 shows the field as a result of an interpolation on the amplitude and phase of the input data. Figures 2.8 and 2.9 show the same relationship for the $\phi = 90^\circ$ scan. Figure 2.6 and Figure 2.7 show the amplitude and phase parts of this same H_x field. Again, the difference in the figures is the method of interpolation. Figures 2.10 and 2.11 show this relationship in the $\phi = 90^\circ$ scan. Similar results were found for the H_y fields in both scan planes.

Some observations to be made are that the interpolation routine does an excellent job of matching the measured data in the region of the inner rings for all quantities of interest, regardless of the field representation that is interpolated. However, it is seen that the match begins to deteriorate towards the outermost rings. This error is most pronounced by the phase plots. The explanation for this is fairly simple; the data is densely packed in the inner rings, so the interpolation chooses between points which are very closely spaced in r and ϕ . The closer the points are to each other, the more accurate the interpolation can be. Another reason for the high accuracy in the innermost region is that the fields are strong, and the phase is fairly uniform. For the outermost rings, the properties which helped in the case of the inner rings both vanish; the spacing becomes large and the fields are much lower. In particular, the phase past the edge of the reflector begins to change very rapidly as a function of distance. In this case the edge of the reflector is at 20.66λ . It seems that while both representations of the output data can be useful, the amplitude and particularly the phase give a better feel for the reason a deviation from the measured data exists.

The question about which field representation is most appropriate to interpolate by may be addressed. By careful study of the graphs one sees that both methods agree with each other to the resolution of the graph, but that the results of the interpolation from the polar representation show a few anomalies at various points. If studied carefully, these anomalies may be understood. Notice that they occur in the amplitude of the real and

imaginary parts of the field, interpolated from the polar representations, such as in Figure 2.5, and that they seem to be of the proper magnitude but of the negative sign. Notice also that they do not seem to appear in the plots of the amplitude of the field, such as in Figure 2.7, but that they do exist in the phase plots of these same figures. Careful inspection of these figures indicates that the phase anomaly is 180° . The conclusion is that there may be an ambiguity in defining the phase of the field, given the Cartesian representation, as is done in the interpolation routine. This is done because the data which is given to the routine is in the Cartesian format from the previous software which supplied the data from the JPL near-field test facility. If the data was not converted to the Cartesian form prior to the interpolation routine, then the results may not show these anomalies. For this reason it is felt that the anomalies should be of no concern, and that the results show for all practical purposes that the interpolation is independent of the input format of the fields. The patterns generated from this data were compared during the development of Chapter 3 and there was no discernible effect.

Computing Requirements

The various interpolation computer runs were timed for a simple simulated 15 ring case with 31 scans, and with the Viking 63 ring data and 129 scans. The interpolation algorithm is independent of all factors except the number of scans, and that dependency is a linear one, so the two data points given above should be enough to define a relationship between the required CPU time and the number of scans. This relationship is shown in Figure 2.12. In this figure is a line representing the CPU time requirement and one representing the overall run time. As was stated at the beginning of this chapter, the execution time is subject to decrease if the storage technique is changed from direct access files to virtual memory. If the virtual memory feature is used then the data which is on the disk file will be stored in a special area of the core and require special programming techniques; however, the execution time would be much faster due to the decreased data access time.

This would cause a downward shift in the overall run time line. This is one of the areas open for further investigation.

Conclusions Regarding Interpolation

In this chapter, the various algorithms for the interpolation of the plane-polar data to a rectangular coordinate system were discussed and one was selected. This algorithm is the 4-point bivariate Lagrange interpolation. It was applied to both a set of simulated data which was of uniform amplitude with phase quadrature, and to a set of data which was measured at the JPL plane-polar facility. The application of this algorithm shows promise as an all purpose algorithm for antenna measurements as was suggested by Ngai, and Profera [1984]. The accuracy of the data was shown to be very good for the inner region of the measurement plane, and to decrease slightly as the distance from the center of the coordinate system increased. This phenomenon was explained as due to the amount of data available in each region. It seems not to matter whether the complex data interpolated is in the Cartesian format or the polar format, given the $1/2 \lambda$ spacing, but that there may be an ambiguity in the definition of the phase of the polar form when calculated from the Cartesian form. This phase ambiguity may be the result of the discontinuity of the function at $\pm 180^\circ$ which is only a problem in the software and which may be easily overcome. For this reason, and because the data is given originally as real and imaginary, the data reduction on the near-field data by the FFTs will be done on the results of the interpolation on the real and imaginary parts of the field.

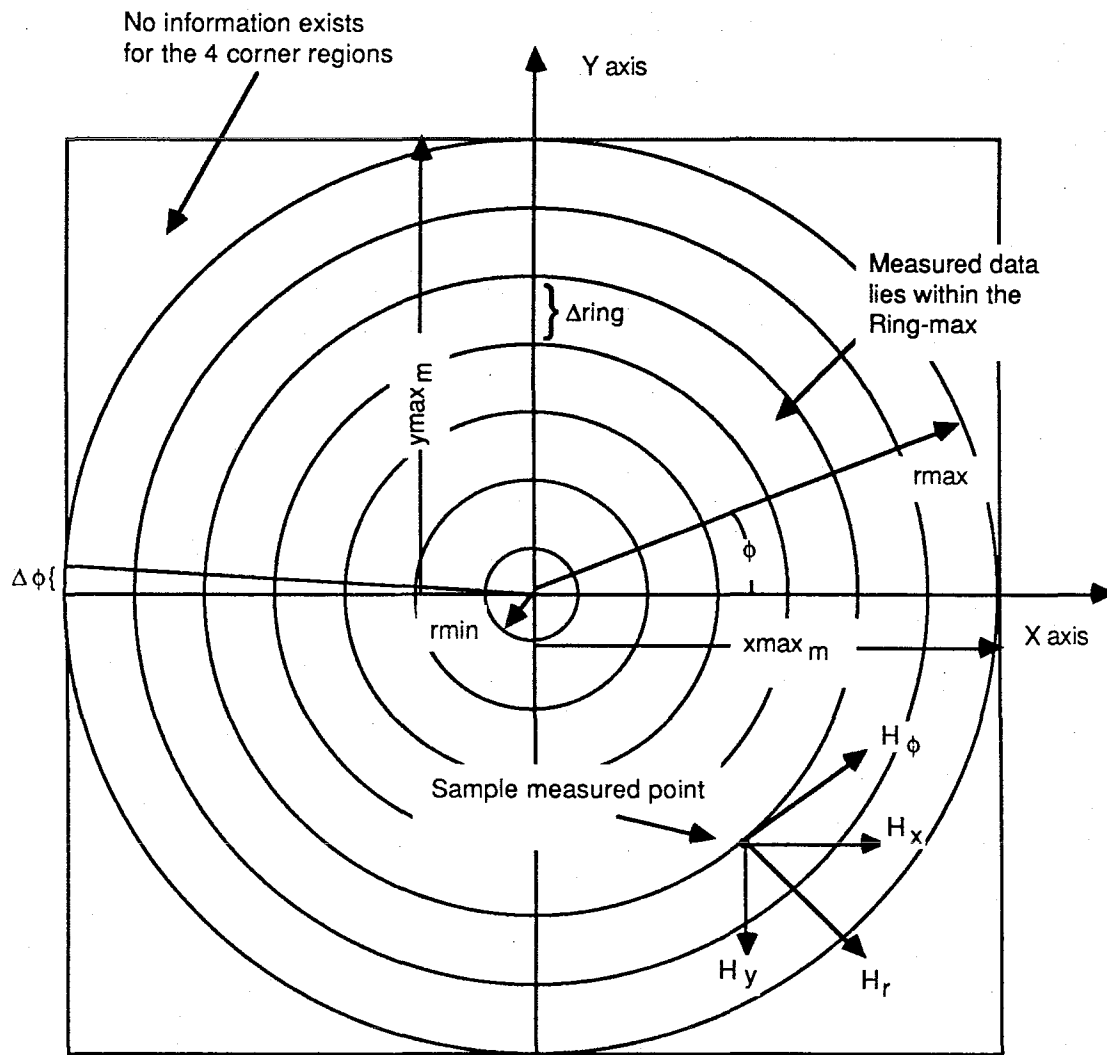


Figure 2.1. The Coordinate System Used for Plane-Polar Measurement

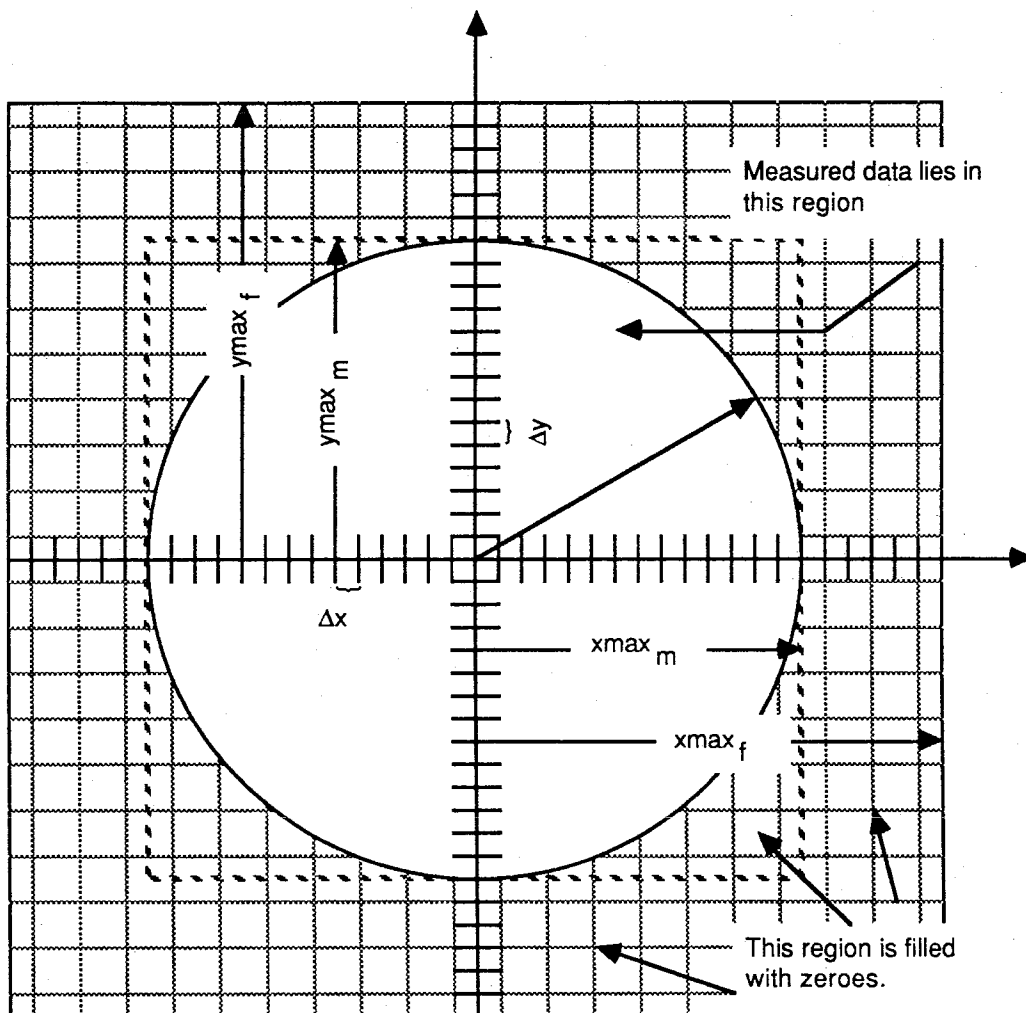


Figure 2.2. Rectangular Coordinate System for Interpolation

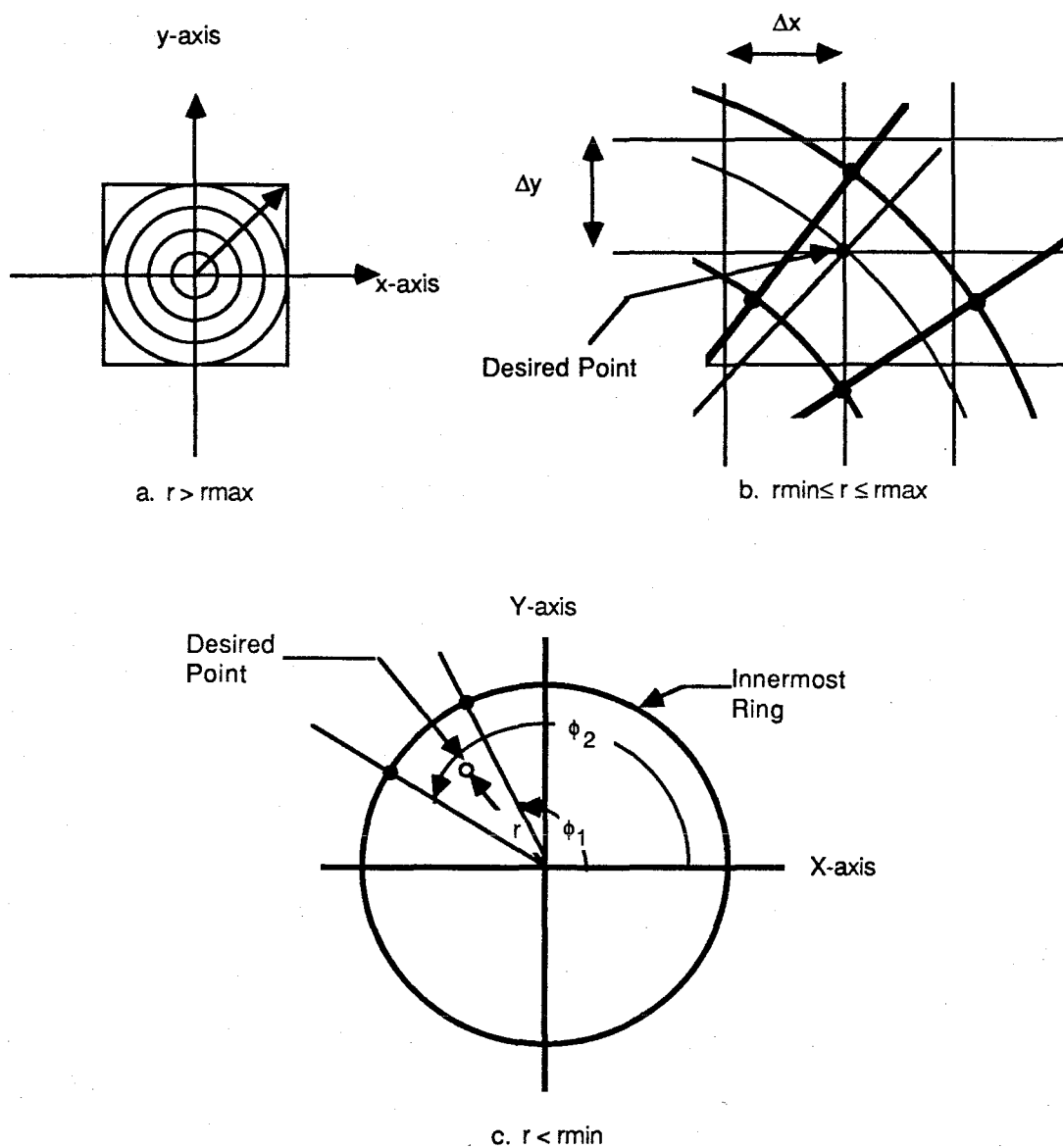


Figure 2.3. The Three Regions of Interest Regarding the Interpolation to Rectangular Coordinates.

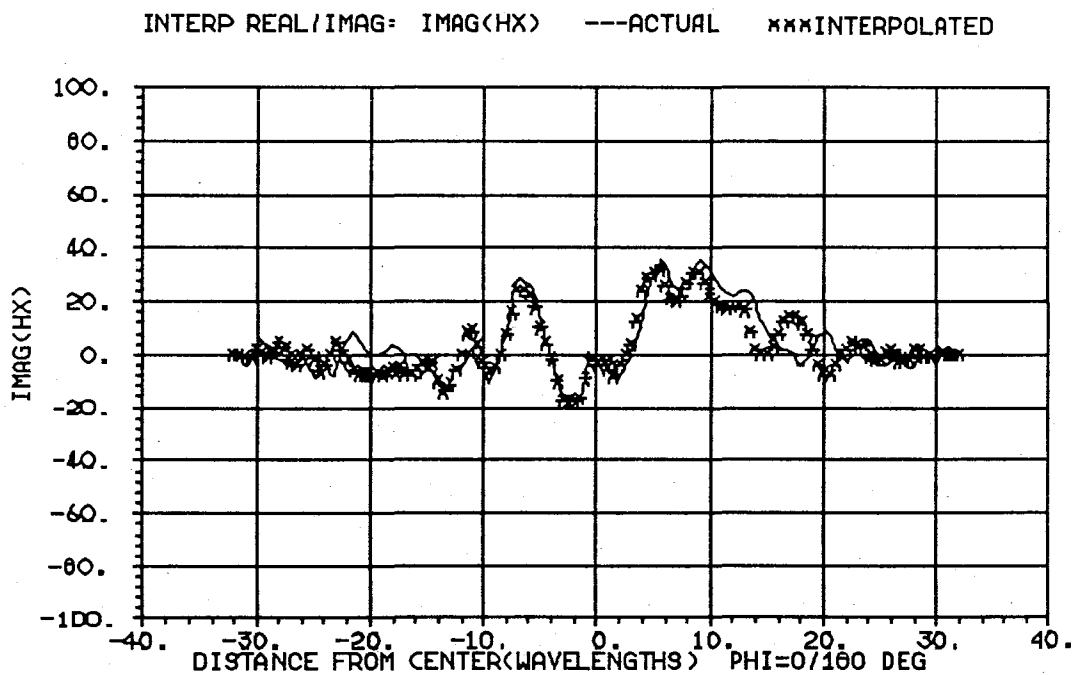
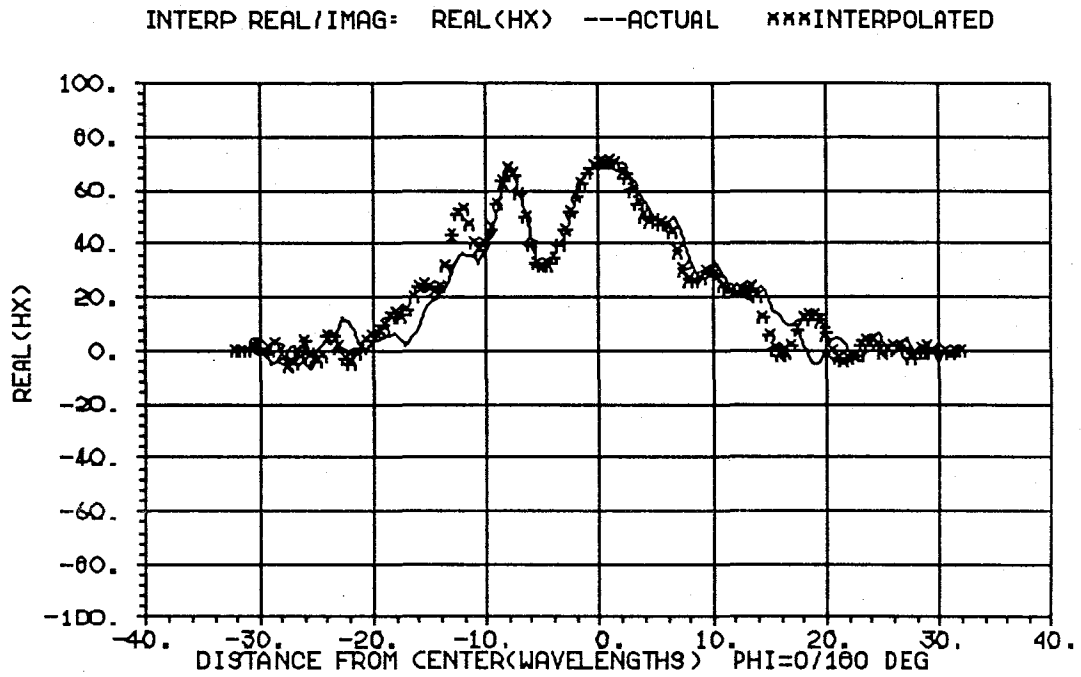


Figure 2.4 Results of Interpolating on the Real and Imaginary Parts of the Field
Shown is the Amplitude of the Real and Imaginary Parts for the Cut Along the X-axis

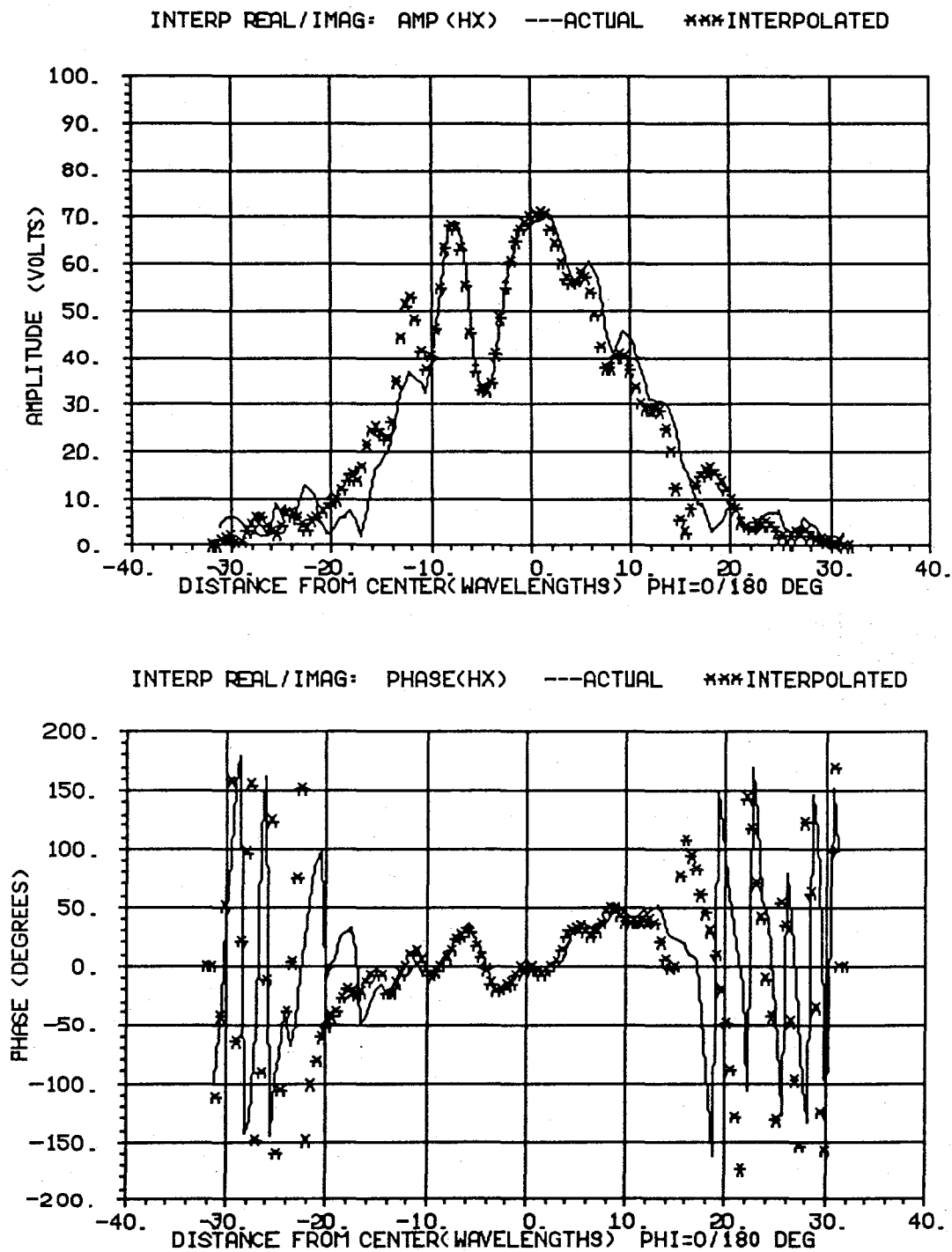


Figure 2.5 Results of Interpolating on the Real and Imaginary Parts of the Field
Shown is the Magnitude and Phase Parts for the Cut Along the X-axis

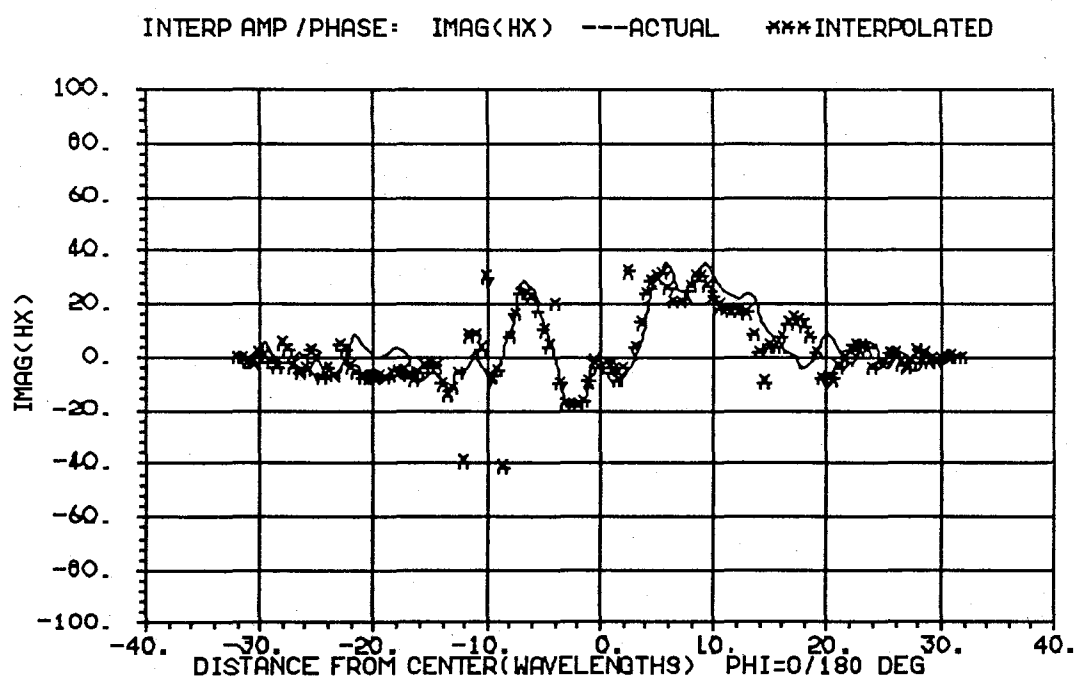
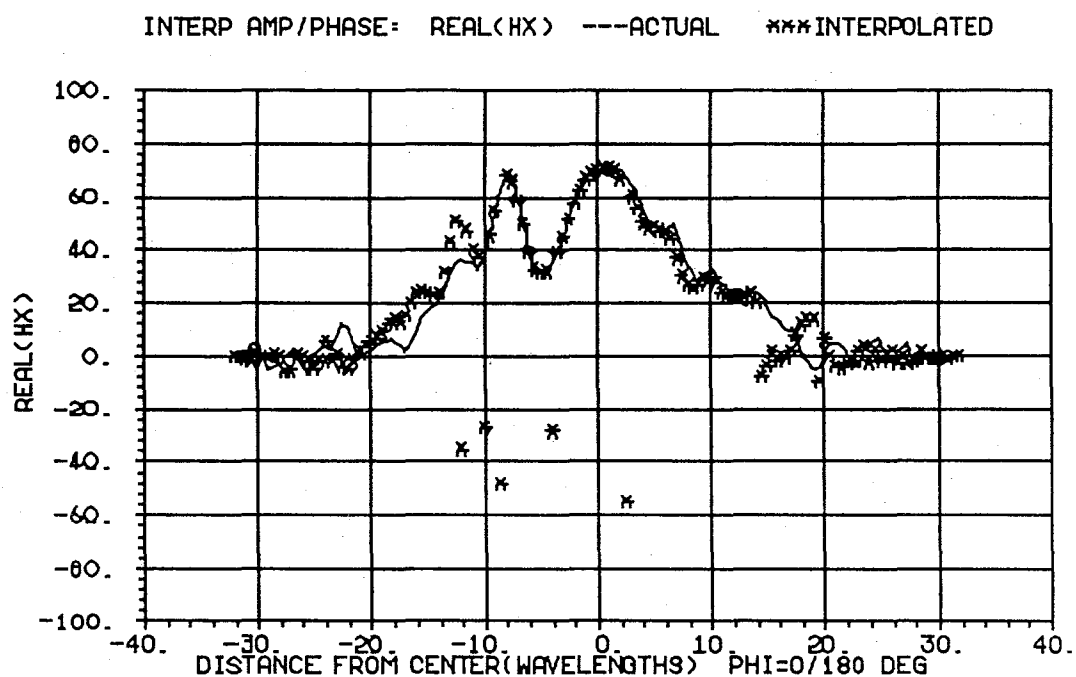


Figure 2.6 Results of Interpolating on the Magnitude and Phase Parts of the Field
Shown is the Amplitude of the Real and Imaginary Parts for the Cut Along the X-axis

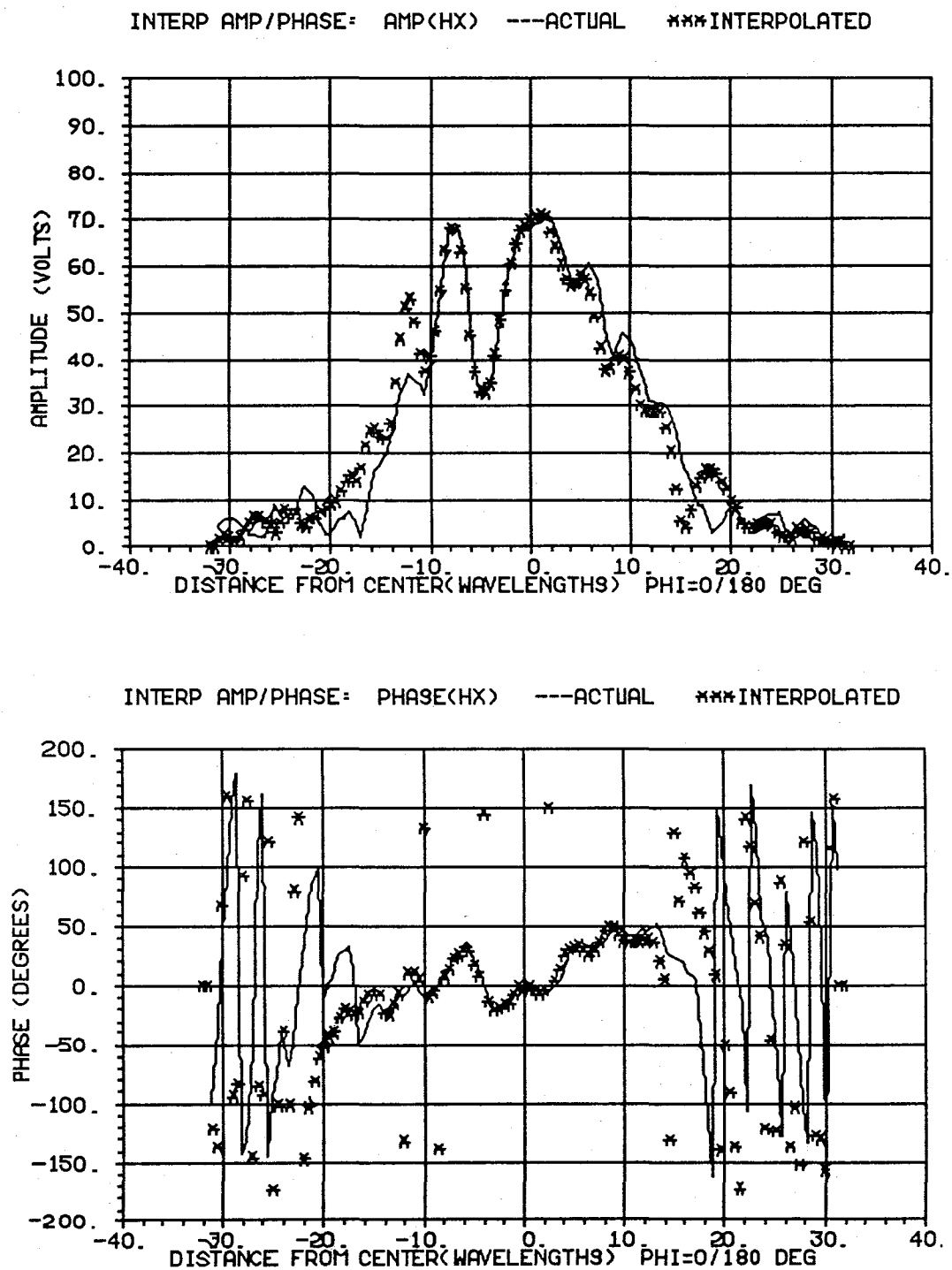


Figure 2.7 Results of Interpolating on the Magnitude and Phase Parts of the Field
Shown is the Magnitude and Phase Parts for the Cut Along the X-axis

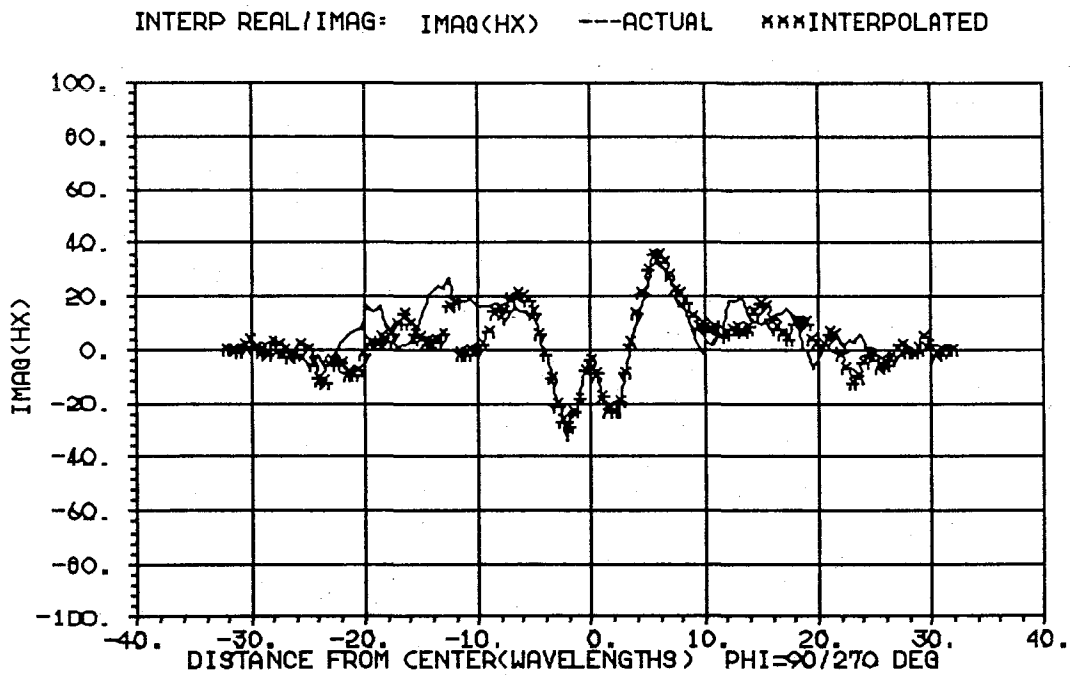
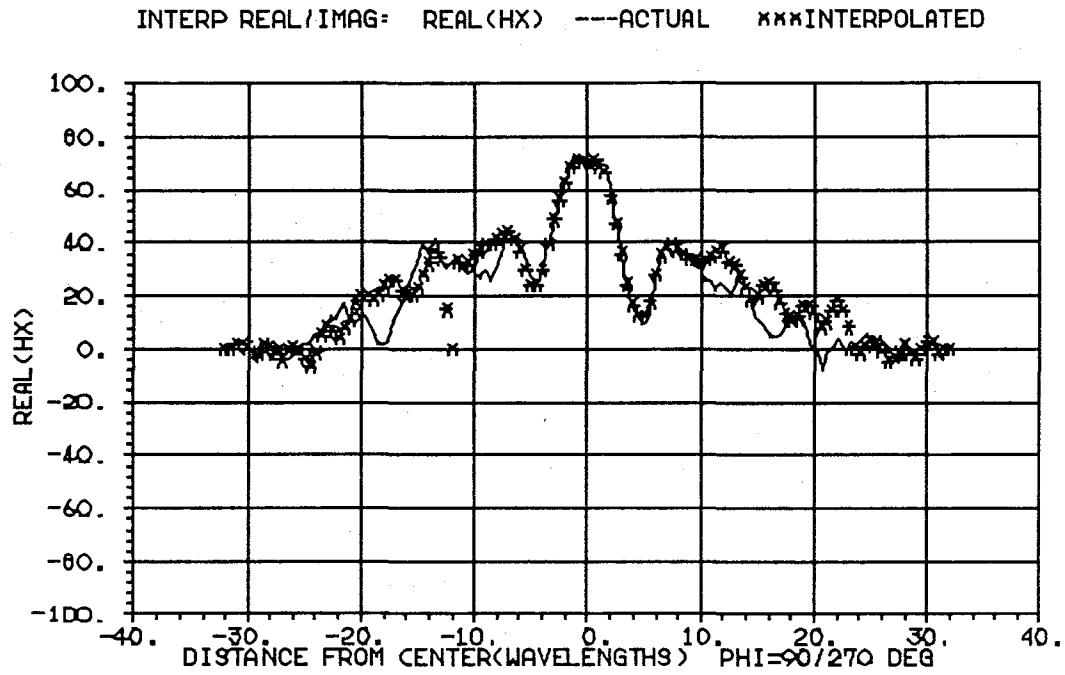


Figure 2.8 Results of Interpolating on the Real and Imaginary Parts of the Field
Shown is the Amplitude of the Real and Imaginary Parts for the Cut Along the Y-axis

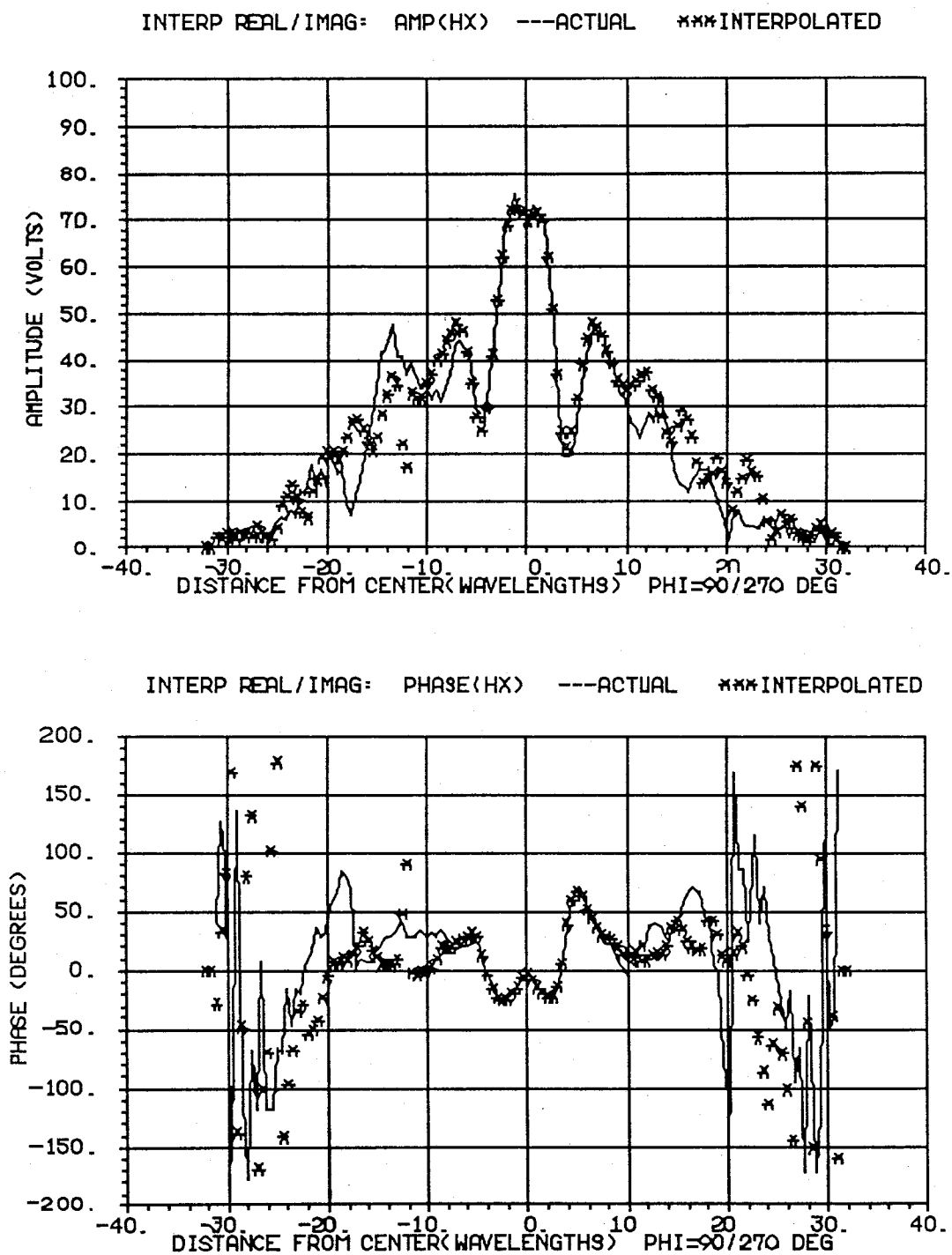


Figure 2.9 Results of Interpolating on the Real and Imaginary Parts of the Field
Shown is the Magnitude and Phase Parts for the Cut Along the Y-axis

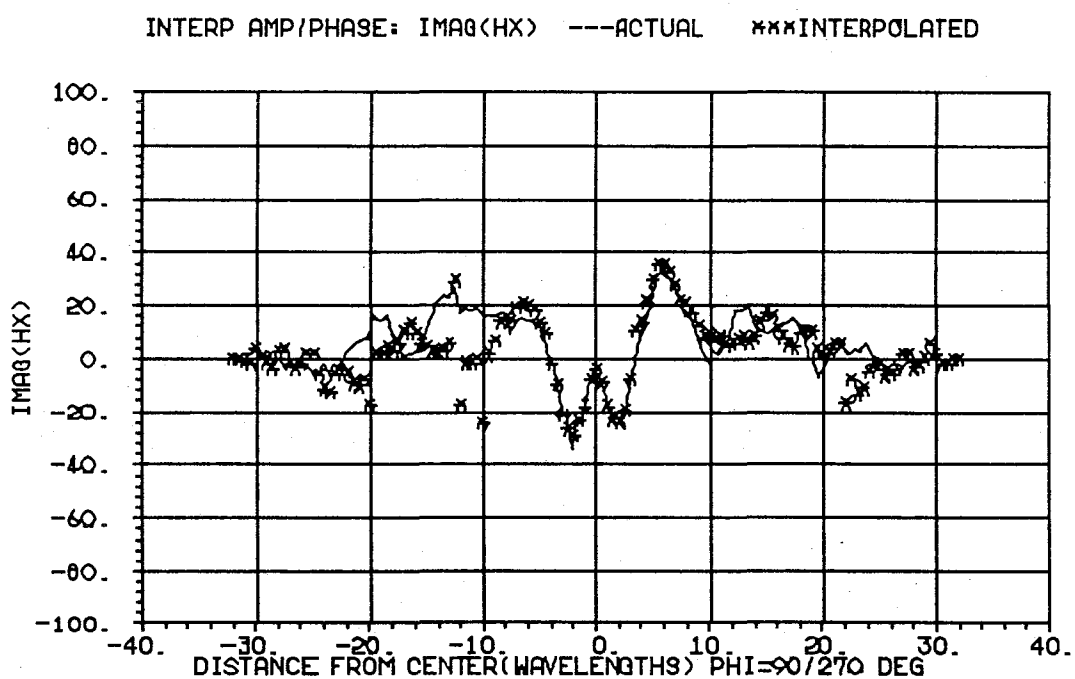
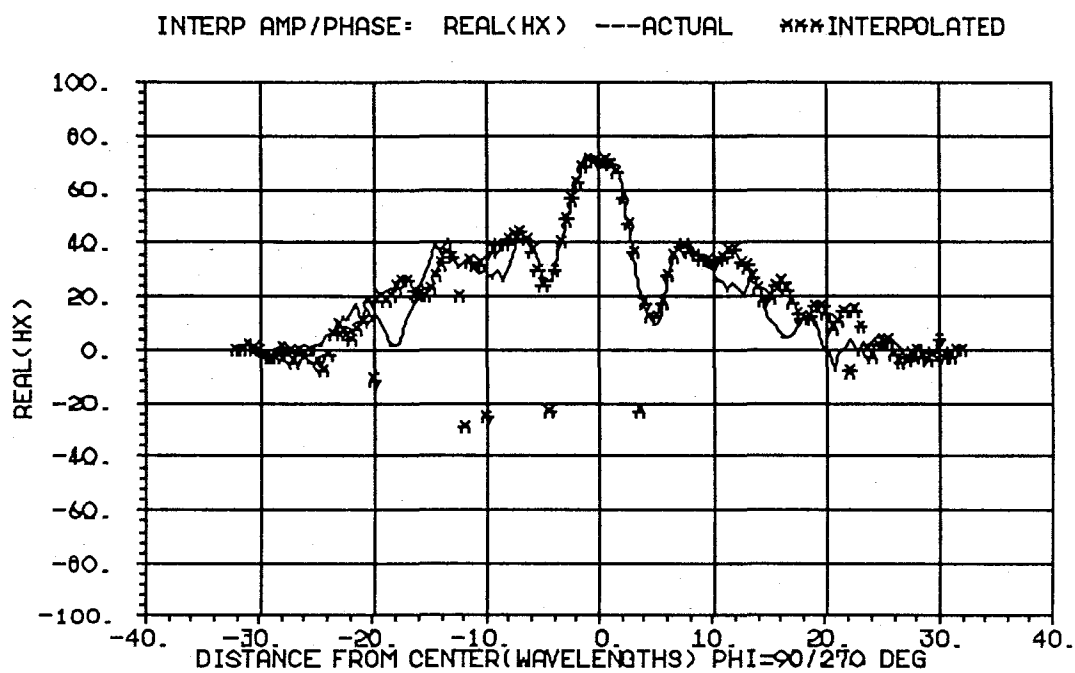


Figure 2.10 Results of Interpolating on the Magnitude and Phase Parts of the Field
Shown is the Amplitude of the Real and Imaginary Parts for the Cut Along the Y-axis

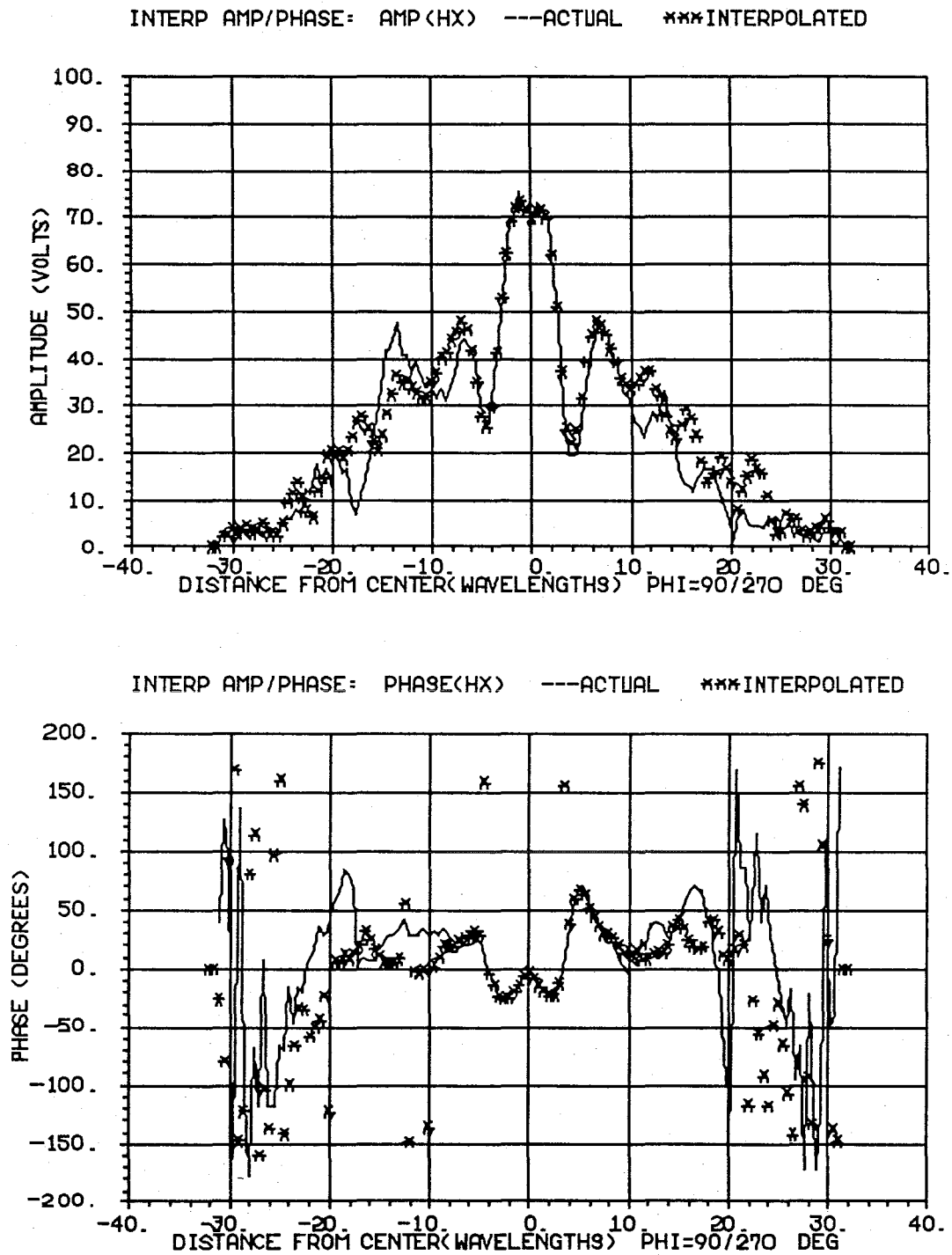


Figure 2.11 Results of Interpolating on the Magnitude and Phase Parts of the Field
Shown is the Magnitude and Phase Parts for the Cut Along the Y-axis

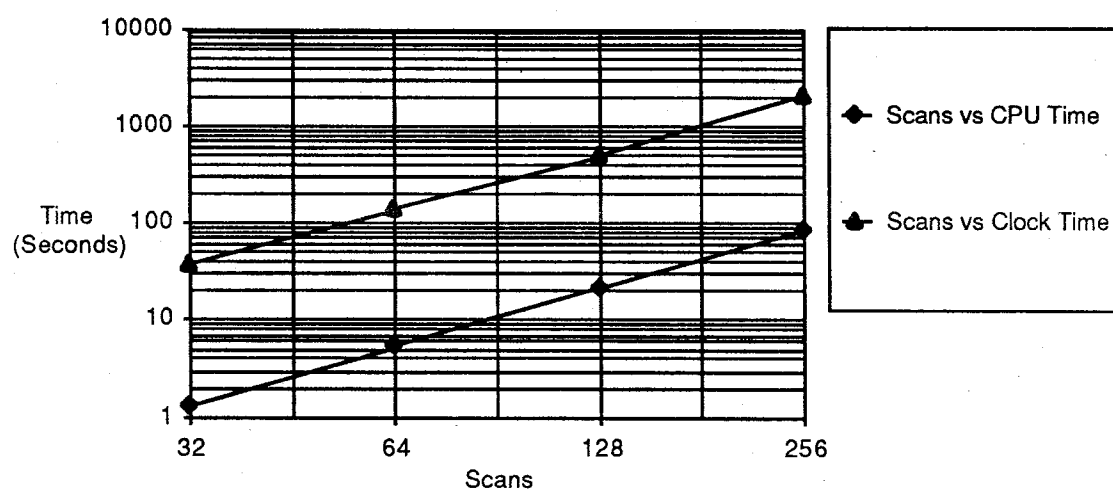


Figure 2.12 The Number of Scans vs Time to Perform the Interpolation

Chapter 3

CALCULATION OF THE FAR-FIELD ANTENNA PARAMETERS

Background and Far-Field Formulations

Once the measured plane-polar near-field data is available, and it has been interpolated onto a rectangular coordinate system as described in Chapter 2, the processing to calculate the far-field quantities can begin. The primary interest is to calculate the normalized co-polarized and cross-polarized components of the electric far field. These fields values are complex and are usually expressed in polar form as magnitude and phase. In this chapter, the formulations representing these fields are shown and the techniques used to calculate them demonstrated. The basis for the far field calculations comes from the techniques described by Rahmat-Samii, Galindo-Israel, and Mittra [1980]. This reference is the basis for the Jacobi-Bessel formulation and will be heavily cited in this chapter, therefore, in order to maintain continuity in the text, it will be referred to as the near-field reference.

It can be shown by application of the Lorentz reciprocity theorem that the output voltage of the near field measurement probe is proportional to the antenna electric and magnetic fields, \bar{E}_a and \bar{H}_a . The near-field reference has taken this result and shown that the relation between the motion of the probe in the measurement plane and the antenna is a convolution expression of the probe fields and the antenna fields \bar{E}_a and \bar{H}_a . Furthermore, the near-field reference defines an apparent induced current in the scan plane, $\bar{q}_m(\bar{r}')$, and a radiation equation which is in the form of a Fourier transform. This integral is given by:

(3.1)

$$T(\theta, \phi) = \iint_{-\infty - \infty}^{\infty \quad \infty} \bar{q}_m(\bar{r}') e^{jk(\hat{r} \cdot \bar{r}')} dx' dy'$$

where the θ and ϕ dependence is found in the exponent of the kernel. The probe is an open-ended waveguide and can be modeled as a loop which measures the magnetic field,

\vec{H} . The near-field reference shows that the $\vec{q}_m(\vec{r})$ term in Equation 3.1 is related to the measured near-field data by the relation $2\hat{n} \times \vec{H}$ where \hat{n} is the unit normal in the scan plane. In general, the probe may be any type, as long as the user knows the quantities which are being measured. The $\vec{q}_m(\vec{r})$ term in Equation 3.1 will be modified accordingly to account for both the \vec{H} and the \vec{E} fields. Figure 3.1 shows the coordinate system which defines the various terms in this equation. Specifically, the primed variables refer to the source or antenna coordinates, and the unprimed refer to the far field or observation coordinates.

In the Jacobi-Bessel technique, Equation 3.1 is rewritten in such a manner that the integrand may be expanded into a series which is integrable in closed form. The coefficients of this series are themselves integrals, however, they are easier to integrate numerically than the highly oscillatory Fourier transform. The Jacobi-Bessel technique is unique in that the coefficients of this expansion are independent of the observation angles in the far field, thus, once they are calculated the radiation integral becomes a simple summation of a polynomial equation for any far field point. This is very efficient because Equation 3.1 must be calculated for every far field point desired.

While the Jacobi-Bessel technique reduces the radiation integral into a series and then evaluates this series for each far field point, this thesis took a more direct approach; integration of Equation 3.1 via the FFT. Equation 3.1 is a Fourier transform, however, it does not resemble the form of Equation B-8 in Appendix B, which is the form that the FFT algorithm used in this thesis will integrate efficiently. Therefore, we must be able to write Equation 3.1 in the form shown in the appendix in order to apply the FFT and to understand the results. To do this we use Figure 3.1 and see that,

$$\begin{aligned} \hat{r} &= \frac{\vec{r}}{|\vec{r}|} = (x\hat{x} + y\hat{y} + z\hat{z})/|\vec{r}| \\ &= \sin(\theta)\cos(\phi)\hat{x} + \sin(\theta)\sin(\phi)\hat{y} + \cos(\theta)\hat{z} \end{aligned} \quad (3.2)$$

and that,

$$\vec{r}' = x'\hat{x} + y'\hat{y} + z'\hat{z} \quad (3.3)$$

thus,

$$\hat{r} \cdot \bar{r}' = x' \sin(\theta) \cos(\phi) + y' \sin(\theta) \sin(\phi) \quad (3.4)$$

Now, one may define transform variables u and v , as

$$\begin{aligned} u &= \sin(\theta) \cos(\phi) \\ v &= \sin(\theta) \sin(\phi) \end{aligned} \quad (3.5)$$

and using $k = 2\pi/\lambda$, Equation 3.1 may be written as

$$T(u,v) = \int_{-\infty}^{\infty} \int_{-\infty}^{\infty} \bar{q}_m(\bar{r}') e^{i2\pi(x'_\lambda u + y'_\lambda v)} dx' dy' \quad (3.6)$$

where x'_λ and y'_λ are the positions in the measurement plane in terms of λ .

At this time, it is worthwhile to point out that the approach taken by Kerns at NBS [1950,1960,1981], Paris, Leach and Joy [1973,1978], and Joy, Leach, Rodrique, and Paris [1978] at the Georgia Institute of Technology, utilize the plane-wave spectrum to describe the relationship between the near-field and the far-field quantities instead of the convolution approach as in the near field reference. These authors begin with the Lorentz reciprocity theorem, then assume negligible multiple reflections between the probe and antenna under test, and use only the first term of the plane wave spectrum. It should be recognized that the results obtained by that technique are the same as shown above.

Calculation of the Electric Field Quantities

A typical far-field pattern is generated by selecting a constant ϕ and calculating many points along θ by repeated integration of Equation 3.1. The FFT algorithm takes an entire set of discrete values of the measured near field data, $\bar{q}_m(\bar{r}')$, as its input and returns an entire set of values for $T(u,v)$ at discrete values of u and v . This means that once the FFT of the near-field data has been calculated, the result may be stored or used immediately to calculate a particular pattern. This set of far-field FFT points is along constant lines of a grid system which is shown in Figure 3.2. The coordinate system is in u - v space and not directly in terms

of θ - ϕ space. The relationship between these variables is given in Equation 3.5. It is apparent from this equation that the relationship between these two spaces is non-linear. In other words, the typical far-field pattern cannot be calculated by directly looking up the values of $T(u,v)$; for a particular choice of ϕ , the locus of points of varying θ does not necessarily lie at the known points of $T(u,v)$. When this happens an interpolation must be applied. The interpolation used is the sinc · sinc type in 2 dimensions, which is described in Appendix B, and has the property of reproducing the exact value of the field at the point in question, if the $1/2 \lambda$ sampling requirement is satisfied. This sampling requirement is discussed in Appendix B.

In order to calculate the far field of the antenna pattern, the field must be related to the integral in Equation 3.1. This relationship is derived in the near-field reference by a convolution of the antenna fields and the probe patterns [Equation 2.19-2.20] and is repeated here for reference:

(3.7a &b)

$$E_{a\theta}(\theta, \phi) = \frac{-1}{\Delta} \cos(\theta) [\tilde{E}_{p\phi}^V(\pi - \theta, -\phi - \pi/2) T_x(\theta, \phi) + \tilde{E}_{p\phi}^V(\pi - \theta, -\phi) T_y(\theta, \phi)]$$

$$E_{a\phi}(\theta, \phi) = \frac{-1}{\Delta} \cos(\theta) [\tilde{E}_{p\theta}^V(\pi - \theta, -\phi - \pi/2) T_x(\theta, \phi) + \tilde{E}_{p\theta}^V(\pi - \theta, -\phi) T_y(\theta, \phi)]$$

where the term Δ is given by

(3.8)

$$\Delta = \tilde{E}_{p\phi}^V(\pi - \theta, -\phi - \pi/2) \tilde{E}_{p\theta}^V(\pi - \theta, -\phi) - \tilde{E}_{p\phi}^V(\pi - \theta, -\phi) \tilde{E}_{p\theta}^V(\pi - \theta, -\phi - \pi/2)$$

In these equations, the T_x and T_y are complex and are the results of applying the sinc-sinc interpolation to the FFT of the \bar{H}_x and \bar{H}_y fields. The actual integration is performed on the x and y components of the currents $\bar{q}_m(\vec{r})$, which are proportional to $2\hat{n} \times \bar{H}_x$ and $2\hat{n} \times \bar{H}_y$. The superscript v in the equations represents one of the probe orientations, and the

second orientation is represented as a $-\pi/2$ factor in ϕ for the v orientation. These details are discussed in the near field reference. Once the orthogonal components of the far-field pattern are known, the total field may be calculated by combining them in the following way:

$$\vec{E}_a(\theta, \phi) = \hat{\theta} E_{a\theta}(\theta, \phi) + \hat{\phi} E_{a\phi}(\theta, \phi) \quad (3.9)$$

Antenna Parameters of Interest

Once these basic electric field quantities are known, many other parameters may be calculated using the proper combinations of the basic quantities. The following are the parameters which were calculated in this thesis once the total electric field was known:

- 1) Gain
- 2) Amplitude and phase patterns
- 3) Polarization Properties
 - a) Axial Ratio
 - b) Tilt Angle
 - c) Sense of Rotation

The software which was generated for this thesis to calculate the radiation patterns relied heavily on the routines which were written for the Jacobi-Bessel algorithm. The test antenna amplitude and phase patterns were calculated from Equation 3.9 using a combination of new and existing software. Also, the existing software had the capability of calculating the polarization parameters which are suggested above. The polarization parameters are important in communications because they define the amount of power which is transferred between the antenna and an electromagnetic field. These parameters are defined as follows:

Axial Ratio:

The ratio of the semi-minor axis to the semi-major axis of the polarization ellipse. In the software, this was calculated from the magnitude of the complex circular polarization ratio. In particular:

$$AR = |(1 - |CPR|) / (1 + |CPR|)|$$

where

$$CPR = (E_{a\theta} + jE_{a\phi}) / (E_{a\theta} - jE_{a\phi})$$

It is recognized that this quantity is the reciprocal of the definition accepted as the IEEE standard [1983], however, it is used in several of the earlier texts and in the Jacobi-Bessel software, so this definition is retained in order to make a comparison to the Jacobi-Bessel technique. In terms of dB, the value has the same magnitude but is negative instead of positive.

Tilt Angle:

The tilt angle is defined as the angle from the x-axis to the semi-major axis of the polarization ellipse, measured towards the y-axis. In the software, this is calculated from the information of the phase of the complex circular polarization ratio. In particular:

$$TA = -1/2 \text{ Phase}(CPR).$$

Sense of Rotation:

The sense of rotation may be obtained from the sign of the axial ratio prior to the final absolute magnitude operation; however, in these programs the fields are calculated and the right- and left-circular components of the fields are plotted. The sense becomes apparent when these plots are inspected.

The gain is an important parameter in any antenna system. It may be measured by one of several techniques which are described in the literature. Among these techniques, the method of gain by comparison is employed in the JPL near-field facility [Rahmat-Samii and Gatti, 1985]. Other techniques include the insertion loss method described by Newell [1985], an application of the three antenna method, and other methods described in the literature [Newell, Baird, and Wacker, 1973]. It should be pointed out that while the three antenna method is theoretically possible for near-field measurements, it requires the probe to be one of the antennas characterized in the near field with the antenna under test acting

as the probe. This is a difficult procedure and has not yet been done in a near-field configuration.

The important parameter which is used from the near-field calculations for the gain measurement is the value of the far-field peak field. In order to verify that the software used in this thesis may recover the correct gain, this peak field may be compared to the value generated by the Jacobi-Bessel technique.

Results of Calculations using the FFT

Given the formulations described in the previous sections, a complete set of software routines were written to calculate the co-polarized and cross-polarized fields in the standard θ - ϕ coordinate system, and the polarization properties of a measured data set. The Viking antenna test data described in the previous chapter was then used to validate the software and techniques. The Viking HGA data is useful since the comparisons between the patterns from direct far-field measurements and from near-field measurements using the Jacobi-Bessel technique have been made many times at JPL and are well documented [Rahmat-Samii, and Gatti, 1985]. The patterns for this antenna are calculated for angles in θ from -10° to $+10^\circ$ for $\phi = 0^\circ$ using the FFT and the Jacobi-Bessel techniques. These results are given in Figures 3.3-3.5. In these figures the size of the FFT used was 128×128 , which was required to meet the $1/2\lambda$ sampling requirement and to use the entire set of 63 rings. A comparison is made to the results of the same calculations on the same data set by the Jacobi-Bessel algorithm, using 10 coefficients in both the n and m indices of the summation.

In Figures 3.3-3.5, the results of the Jacobi-Bessel algorithm converge between $\theta = \pm 5^\circ$. This convergence was verified by a systematic variation of the number of coefficients used to calculate the patterns until the patterns no longer changed for $\theta \leq 5^\circ$. For larger angular regions more coefficients would be needed. For the FFT results, no check of convergence was required since the fields are sampled at separations less than $1/2 \lambda$ and are therefore correct to the angle θ_0 as defined in Figure 3.6 [Newell, 1985]. This figure shows the maximum angle to which the far-field results will be accurate even though the θ_{\max}

from the FFT may be larger depending on the Δx and Δy [See Appendix B for these relationships]. For the Viking test data, the distances $L_x = 64\lambda$, $D_x = 41.32\lambda$ and $d = 63.41\lambda$; therefore, the maximum value of θ for which reasonable results may be expected is $\theta_0 = 10.14^\circ$. Similar results are found for the $\phi = 45^\circ$ and 90° pattern cuts.

The maximum far-field electric field strength is calculated by both the FFT and the Jacobi-Bessel algorithms. The value calculated for this parameter is a function of the setting of the receiver and the signal to the computer which measured the data in the near-field facility. As such, this value is only relative and it suffices to say that the values calculated by each technique were the same to within 0.03 dB. This result indicates that the normalization parameters which were derived for the FFT output are correct, and the FFT technique will be accurate in a gain measurement. Also notice that the comparison gain measurement may be done by using a mix of both techniques with the proper results being calculated since the same field is calculated in both techniques.

Often, the overall pattern of an antenna in the forward radiating region is of interest to an antenna engineer. This pattern can be plotted in 2 dimensions as a contour plot or in 3 dimensions as a surface plot. The integral $T(u,v)$ contains useful information about the sidelobe levels, sidelobe locations, beamwidths, etc., without transforming to the θ - ϕ space; therefore, the resultant FFT output may be immediately used to present useful information.

Computer Resources

The computer resources used to produce the pattern results may be used to indicate a level of computational efficiency. Table 3.1 summarizes the total computer execution times required for both the Jacobi-Bessel technique and the FFT technique. In this table, the total run time is given for the calculation of the $\phi = 0^\circ$ and $\phi = 45^\circ$ cuts of the Viking data set so that one may see the effects to the speed of the FFT technique of calculating patterns off the principal planes. Recall that the sinc-sinc interpolation as described in Appendix B is used for the FFT technique, and that the points are along the main grid line $v = 0$ for the $\phi = 0^\circ$ cut; therefore, the interpolation is a single summation of the

points along the grid line. For the $\phi = 45^\circ$ cut, the points are not necessarily along main grid lines, so the interpolation will be a double summation of all the data at each one of these points. In the case of the Jacobi-Bessel technique, the time required to create a pattern cut is independent of the angle ϕ , and only dependent on the number of coefficients in the polynomial used. There is a non-recurring time expenditure in Table 3.1. In particular, the time to calculate the FFT in one case, and the time to calculate the coefficients in the other. This should be accounted for if one is interested in estimating the run times for repeated pattern calculations at cuts other than discussed. Figure 3.7 illustrates the execution time for a pattern calculation of 101 points for $\phi=0^\circ$ and $\phi=45^\circ$ as a function of the size of the FFT. Also shown in this figure is the time required to calculate a pattern of 101 points using the Jacobi-Bessel technique for $n=m=10$ coefficients.

Table 3.1 Total Execution Times to Calculate Field Patterns (min:sec)

	<u>FFT</u>	<u>Jacobi-Bessel</u>
Reformat Data	0:1.17	X
Interpolate Data to Grid System	8:21	X
Calculate FFT [T(u,v)]	0:40	X
Calculate Coefficients 10 x 10	X	14:15
Create Pattern $\phi = 0^\circ$ for 101 points	0:17	0:19
Create Pattern $\phi = 45^\circ$ for 101 points	3:26	0:19
Total Time	12:48	14:50

Conclusions

An important conclusion from this chapter is that the FFT technique will rapidly produce the final far-field pattern results for those patterns which will lie on main grid lines. The two normal cuts for $\phi = 0^\circ$ and $\phi = 90^\circ$ lie along the $v = 0$ and $u = 0$ grid lines respectively. If one is interested in a quick look at the patterns of a test antenna, and the amount of data is small, then the FFT technique is a viable way to proceed. There is a drawback to the FFT technique. If one wants to calculate many cuts, to calculate directivity from the patterns for

instance, then a significant amount of CPU time will be required since many of the points will not lie along grid lines. For this case the Jacobi-Bessel technique will be faster since the fields are calculated at any point at the same speed. However, if one is interested in seeing an overall pattern, then the direct FFT output may be used for 2- and 3-dimensional plots and results rapidly generated. Some time will be required to estimate the optimum number of coefficients to use for the Jacobi-Bessel technique to converge. This does not need to be done in the case of the FFT technique if the $1/2 \lambda$ requirement is met. Each case is special in that the sinc-sinc interpolation is very sensitive to the number of grid lines in the 2 dimensional FFT. A little analysis and reference to Table 3.1 and Figure 3.7 would be necessary to estimate the execution time required for each case before any recommendation is made as to the best algorithm to use.

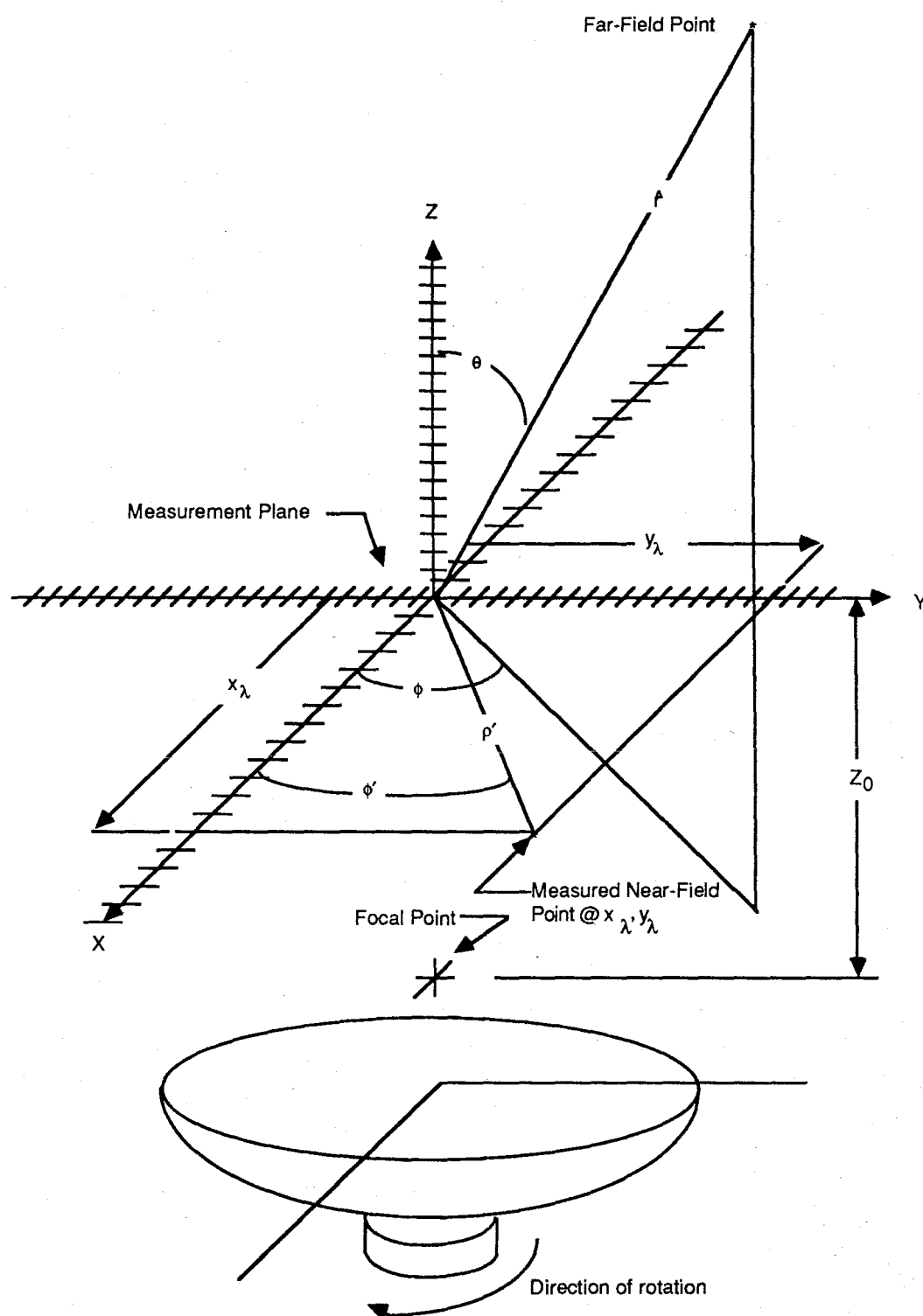


Figure 3.1 Coordinate System for Pattern Calculation and Data Acquisition

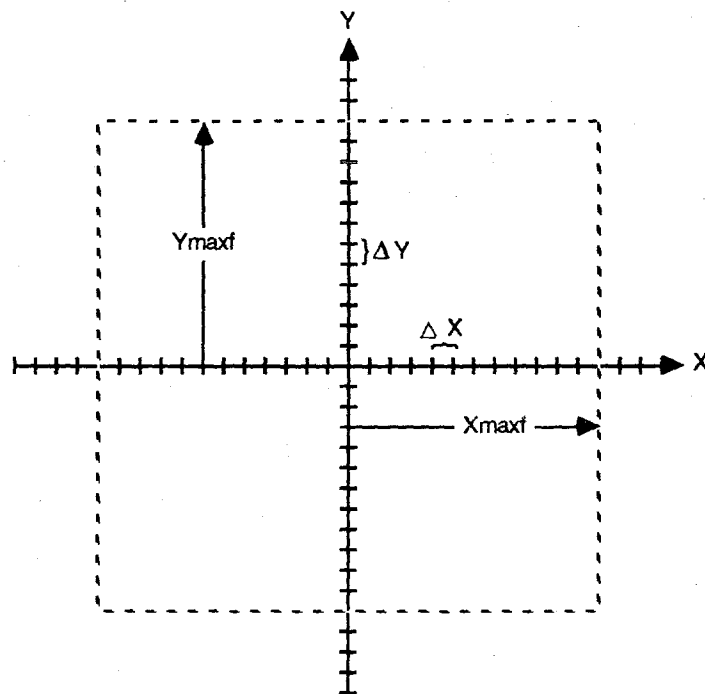


Figure 3.2a x-y Near-Field Coordinate System

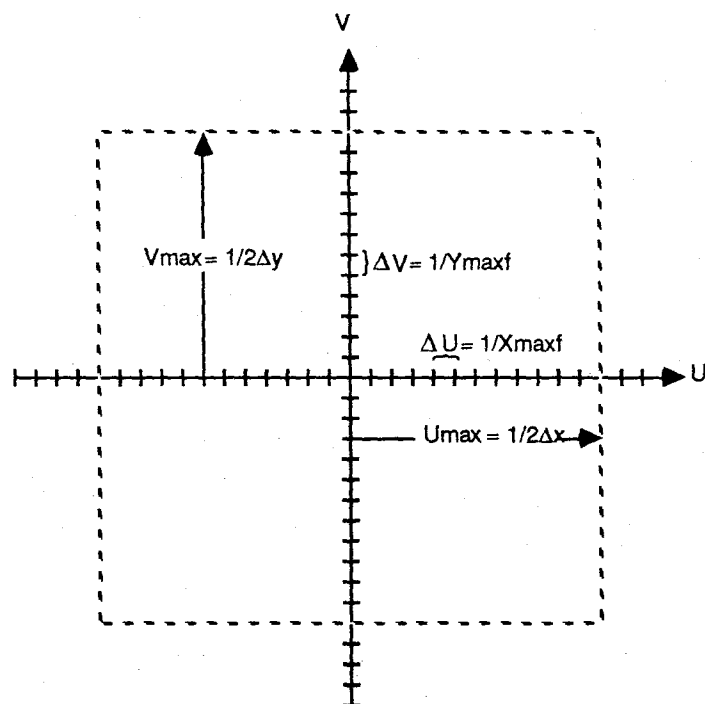


Figure 3.2b u-v Far-Field Coordinate System

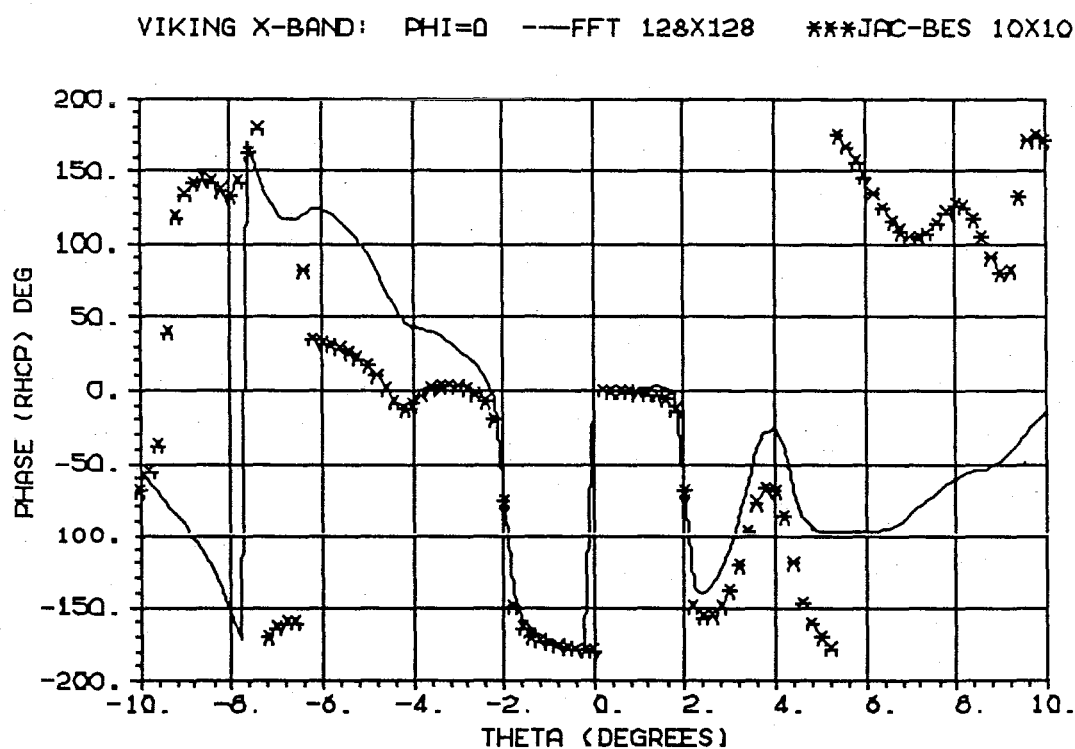
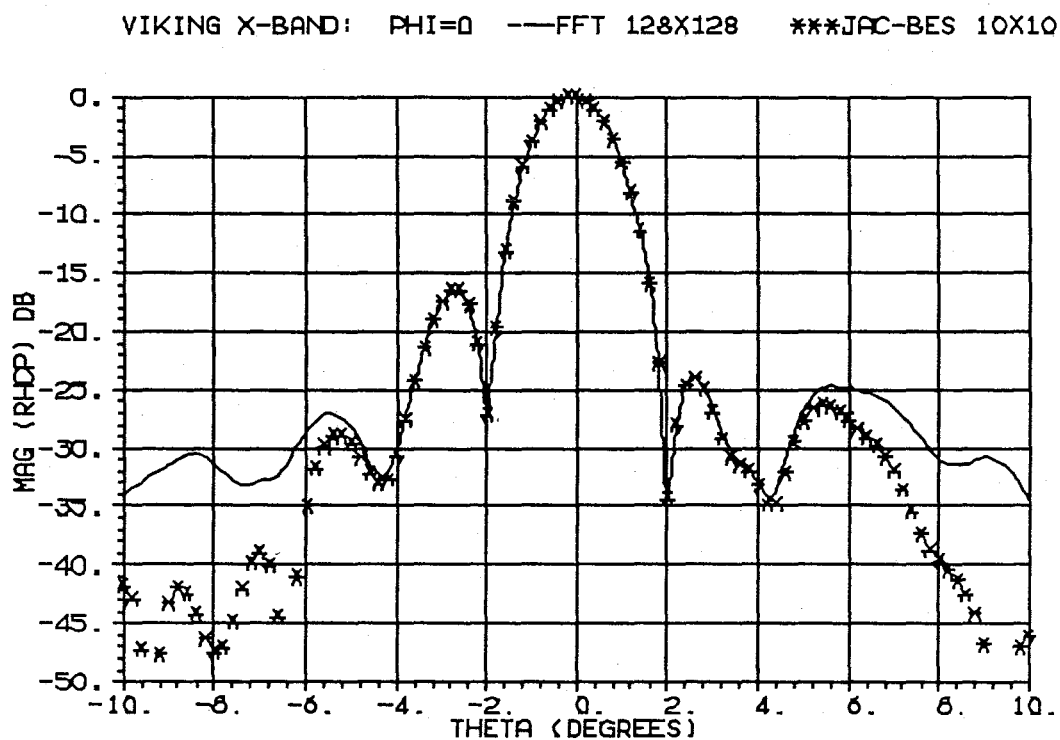
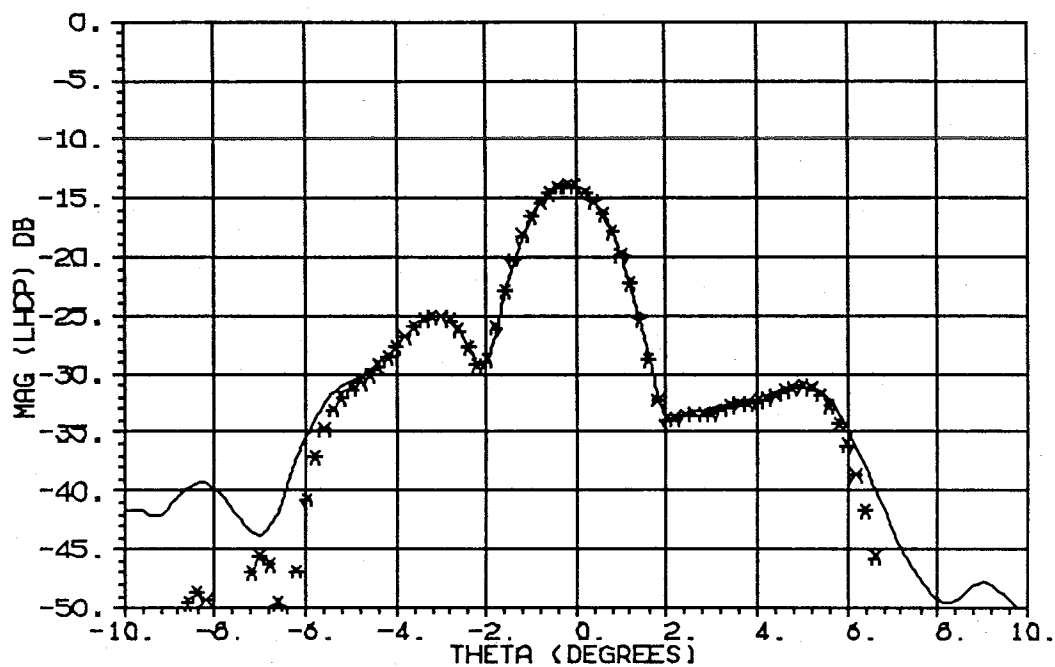


Figure 3.3 Magnitude and Phase Plots for the Viking HGACo-Polarized Components - Comparisons Between FFT and Jacobi-Bessel for the $\varphi = 0^\circ$ Cut
Jacobi-Bessel Coefficients Chosen For Convergence to $\theta = \pm 5^\circ$

VIKING X-BAND: PHI=0 ---FFT 128X128 ***JAC-BES 10X10



VIKING X-BAND: PHI=0 ---FFT 128X128 ***JAC-BES 10X10

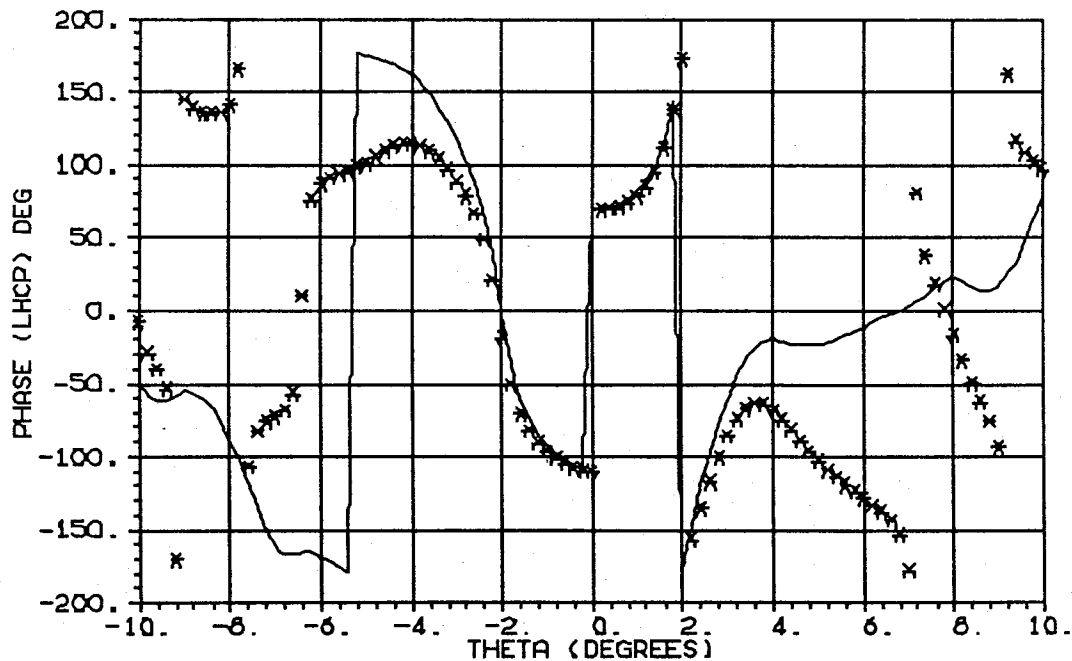
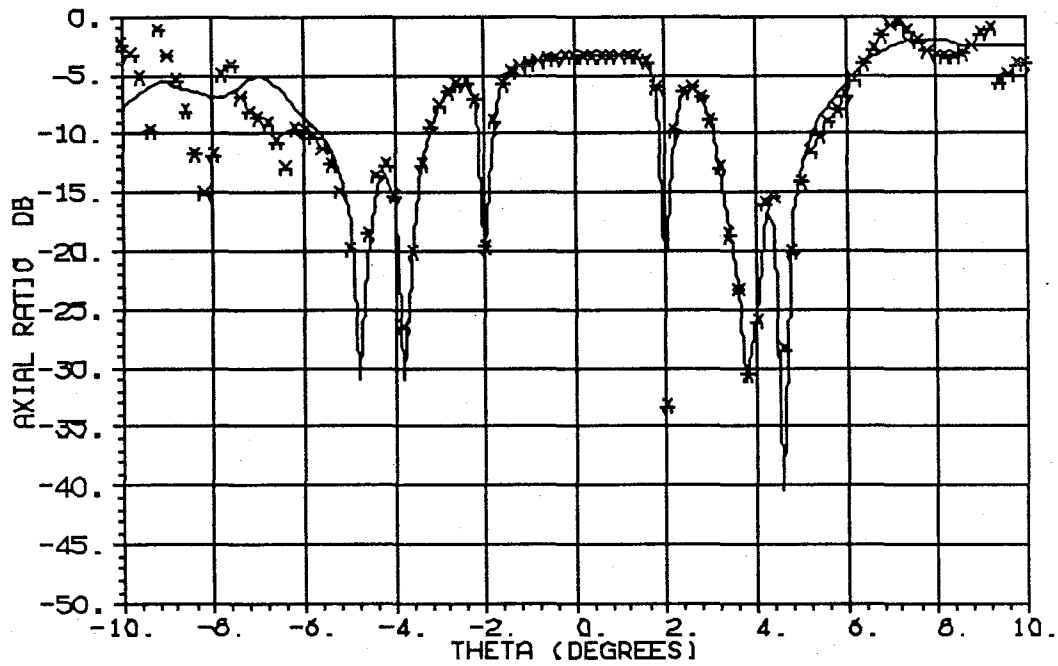


Figure 3.4 Magnitude and Phase Plots for the Viking HGA Cross-Polarized Components- Comparisons Between FFT and Jacobi-Bessel for the $\phi = 0^\circ$ Cut
Jacobi-Bessel Coefficients Chosen For Convergence to $\theta = \pm 5^\circ$

VIKING X-BAND: PHI=0 ---FFT 128X128 ***JAC-BES 10X10



VIKING X-BAND: PHI=0 ---FFT 128X128 ***JAC-BES 10X10

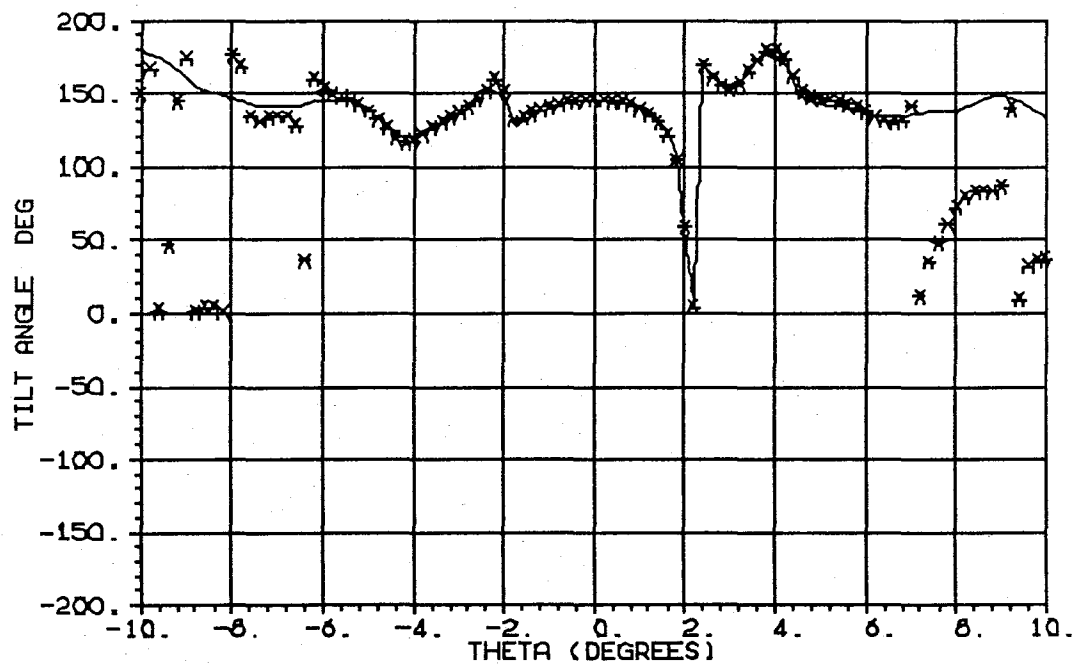


Figure 3.5 Axial Ratio and Tilt Angle for the Viking HGA -
Comparisons Between FFT and Jacobi-Bessel for the $\varphi = 0^\circ$ Cut
Jacobi-Bessel Coefficients Chosen For Convergence to $\theta = \pm 5^\circ$

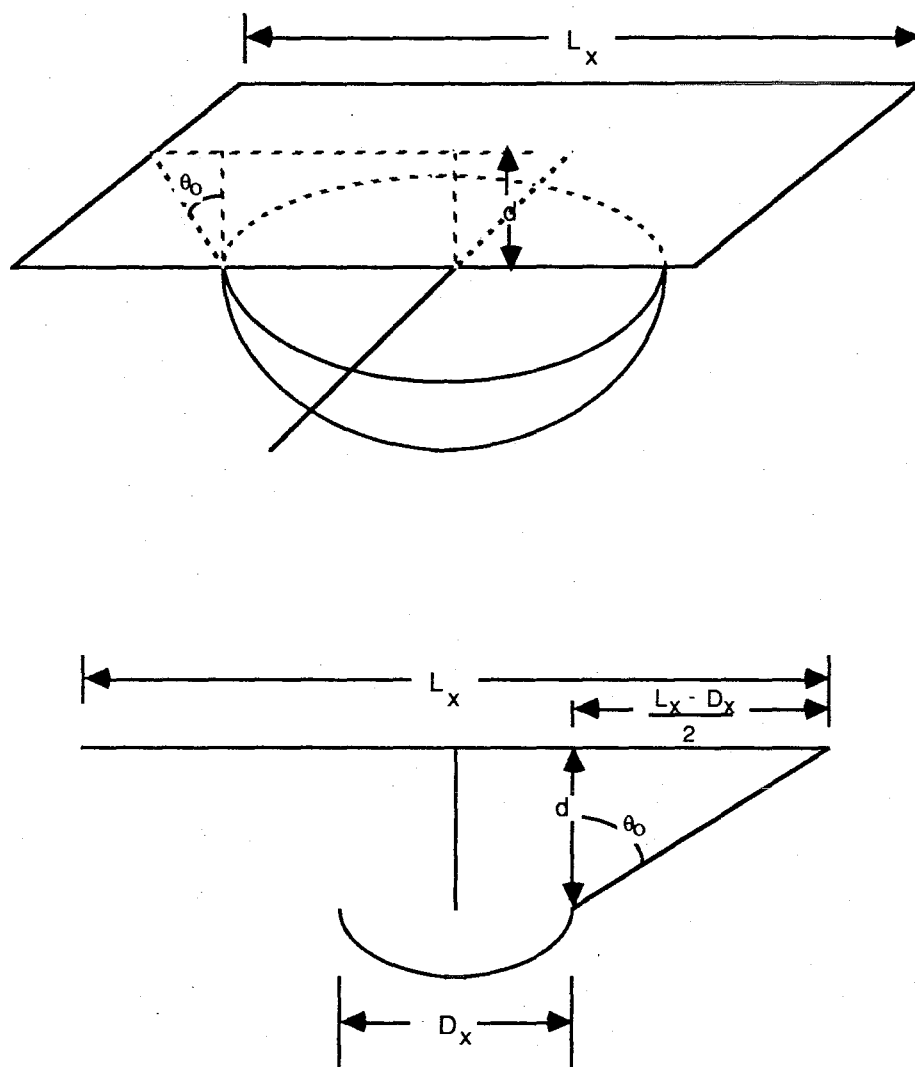


Figure 3.6 Pictorial Description of the Maximum Value of Theta for Which the Fields are Accurate

$$\tan \theta_0 = \frac{L_x - D_x}{2d}$$

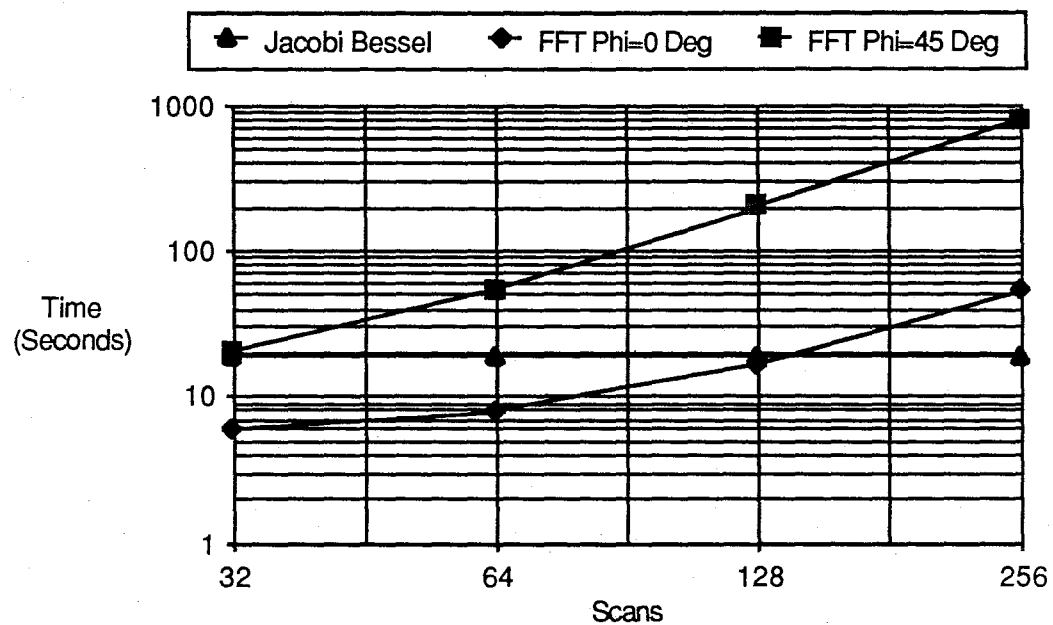


Figure 3.7 Total Time to Calculate the Field Pattern-vs-the Number of Scans: 101 pts

Chapter 4

PARABOLIC REFLECTOR SURFACE DIAGNOSIS FROM NEAR-FIELD MEASUREMENTS

Introduction

Parabolic reflector antennas are widely used in microwave communications, radio science, and radar applications. Each of these applications has specific requirements; however, one common requirement is that the reflector surface be of a good quality measured in terms of its deviation from a paraboloid as a function of wavelength. Surface distortions of a parabolic reflector antenna can cause a loss in the expected performance of the antenna system, unless those distortions are part of the design, as in dual reflector shaping.

Often, the designer of an antenna system believes that all aspects of an efficient design have been considered, only to find that the hardware does not achieve the expected performance. The cause does not always lie in the design, nor in the measurement of the antenna parameters; it could be fabrication errors, assembly errors or even the mishandling of an antenna at any time. When an expensive antenna system does not meet performance specifications, it is usually the responsibility of the designer and test engineer to discover why. To assist in the diagnosis of the problem, near-field measurements may prove useful. In this chapter, the measurement of the surface distortions will be discussed, and a technique presented whereby the measured phase data is used to aid in the distortion measurements for parabolic reflector antennas.

Surface Diagnosis Formulation

The amplitude and phase of the antenna under test is normally measured in near-field scanning techniques. Therefore, it is easy to look at the raw amplitude and phase data via surface plots or contour plots to obtain some knowledge about any gross errors in the antenna system. One would expect, for example, to observe the shadowing effects of the feed and feed support structure of a parabolic reflector antenna in both the amplitude and

phase of the raw data. However, if one is interested in more detailed information regarding the reflector, this near-field data must be manipulated.

A microwave holographic technique has been recently given by Bennett, Anderson, McInnes and Whitaker [1976] that applies a Fourier transform relationship to relate the measured far-field data to the currents on the surface of a parabolic reflector. Rahmat-Samii [1984] has described a technique whereby an iterative approach is used to describe the surface distortions which may exist. This paper is the basis for the following discussions. Rahmat-Samii derives an integral equation given by

$$T(u,v) = \int_{-\infty}^{\infty} \int_{-\infty}^{\infty} J(x', y') e^{jkz'} e^{jk(ux' + vy')} dx' dy' \quad (4.1)$$

where the u and v are the same quantities as previously defined in Equation 3.5, $T(u,v)$ is the same as defined in Equation 3.6, and $k = 2\pi/\lambda$. The various parameters in this equation are illustrated in Figure 4.1. As in Chapter 3, the primed coordinates relate to the source or measured near-field quantities, and the unprimed coordinates relate to the observation or far-field quantities.

Equation 4.1 is the leading term of a Taylor series which describes the entire far-field pattern. Subsequent terms in this series are significant only for wide angle observations and laterally displaced feeds. In this equation, the $J(x', y')$ is referenced in the scan plane and is related to the currents on the surface of the reflector by way of the surface projection Jacobian transformation [Rahmat-Samii and Galindo-Israel, 1980]. Since phase is of most interest for this application, further discussion of each quantity in Equation 4.1 will be omitted.

To show how to apply this to the analysis of the surface errors of reflectors, Rahmat-Samii expresses $J(x', y') e^{jkz'}$ as:

$$J(x', y') e^{jkz'} = |J(x', y')| e^{-jkr'} e^{jkz'} \quad (4.2)$$

where the phase center is referenced to the origin of the coordinate system in Figure 4.1. With reference to Figure 4.2, a purely geometrical analysis will show that the exponent in Equation 4.2 may be expressed as

$$e^{-jkr'} e^{jkz'} = e^{jk(-2F + 2\epsilon \cos \zeta)} \quad (4.3)$$

from which the total distortion phase error is defined as

$$\delta = k2\epsilon \cos \zeta = 4\pi(\epsilon/\lambda) \cos \zeta = 4\pi\epsilon_\lambda \cos \zeta \quad (4.4)$$

For a parabolic reflector it can be shown that the $\cos \zeta$ term is given by

$$\cos \zeta = (1 + (x^2 + y^2)/4F^2)^{1/2} \quad (4.5)$$

Thus, the integral in Equation 4.1 may be written as

$$T(u,v) = e^{-j2kF} \iint_{-\infty}^{\infty} |J(x',y')| e^{j\delta} e^{jk(ux' + vy')} dx' dy' \quad (4.6)$$

In Equation 4.6, the constant phase term e^{-j2kF} resulted from using the origin of the coordinate system as the phase reference. Since it is a constant value for all x,y , it may be accounted for when looking at the phase results. If the Fourier transform operation is expressed by $F\{g(x)\}$, then one can write Equation 4.6 as

$$T(u,v) = e^{-j2kF} F\{|J(x,y)| e^{j\delta}\} \quad (4.7)$$

By applying an inverse Fourier transform, δ may be written as

$$\delta = 2kF \text{ phase}[F^{-1}\{T(u,v)\}] \quad (4.8)$$

from which $\epsilon_\lambda(x, y)$ can be found to be

$$\epsilon_\lambda(x, y) = 1/4\pi [1 + (x^2 + y^2)/4F^2]^{1/2} \text{ phase}[e^{j2kF} F^{-1}\{T(u,v)\}] \quad (4.9)$$

Equation 4.9 is the basis for the measurement of the surface deviation from a perfect parabolic shape; that is, the equation was developed assuming that the initial shape was a paraboloid. Therefore, with the far-field parameter $T(u,v)$ referenced to the focal plane known, the inverse Fourier transform may be calculated and the error as a function of wavelength may be calculated. A second assumption for the development of Equation 4.9

was that the phase distribution at the focal plane was uniform. If it is not, a correction factor would have to be included to account for this condition.

The phase of the inverse Fourier transform of $T(u,v)$ in Equation 4.9, referenced in the focal plane, may have not only the error due to a non-uniform phase over the focal plane. It may also have a linear error due to lateral displacement of the feed and a quadratic error due to defocus of the feed. These errors can be calculated in a least-squared sense and eliminated from the data to produce only those phase errors due to the surface deviation.

Implementation

Near-field data can be applied to the calculation of the surface deviation if one observes that the output of the FFT algorithm, which was developed in the previous chapter, yields $T(u,v)$, as described both in Equation 3.6 and Equation 4.6, with the exception of a phase constant. This resulted from the particular selection of integration variables u and v as described in Equation 3.5. This means that no special changes have to be made to the FFT in order to apply it to the surface diagnosis problem.

In order to apply the measured near-field data to the diagnostic problem the data must be referenced at the focal plane, not the scan plane which is located a distance z_0 above the focal plane as shown in Figure 3.1. This is accomplished by calculating the far-field quantity $T(u,v)$ as in Chapter 3, and then multiplying by a factor of $e^{jkz_0\cos(\theta)}$. The inverse Fourier transform may then be calculated by the IFFT routine. The phase of the IFFT output is then used in Equation 4.9 to calculate the surface deviation.

There are two considerations in calculating the IFFT of the $T(u,v)$. The first is that the value of θ is not known directly for the calculation of $e^{jkz_0\cos(\theta)}$; instead, u and v are given. The value of θ must be calculated from a knowledge of u and v . This is not a straightforward task for (u,v) outside the unit circle and also because the relationship between (u,v) and (θ,ϕ) is nonlinear. The second consideration is that the $T(u,v)$ calculated from a direct application of the FFT does not include any compensation for the probe. The probe compensation can be included once the values of θ and ϕ are known.

The first of the considerations is to find (θ, ϕ) given (u, v) . It is shown in Appendix B that the range of the variables u and v are related to the Δx and Δy by an inverse relationship: $u_{\max} = 1/2\Delta x$ and $v_{\max} = 1/2\Delta y$. Therefore, if the $1/2 \lambda$ sampling requirement is maintained for Δx and Δy , the values of u_{\max} and v_{\max} are unity. From Equation 3.5 it is seen that

$$u^2 + v^2 = \sin^2(\theta) \quad (4.10)$$

which indicates that when

$$(u^2 + v^2)^{1/2} \geq 1 \quad (4.11)$$

the value of θ is a complex number and that the factor $e^{jkz_0 \cos(\theta)}$ will have a decaying component that approaches zero. It can be shown that the complex value of θ in this case is pure imaginary, so that the entire factor will approach zero. Thus, one could assume zeroes for values of the $T(u, v)$ when u and v satisfy Equation 4.11, and when u and v do not satisfy Equation 4.11, the calculation of θ and ϕ become easier for the computer implementation. For values of u and v which lie within the unit circle, the values of θ and ϕ may be derived from Equation 3.5 as

$$\begin{aligned} \theta &= \sin^{-1}[(u^2 + v^2)^{1/2}] & 0 \leq \theta \leq \pi/2 \\ \phi &= \tan^{-1}(v/u) & -\pi/2 \leq \phi \leq \pi/2 \end{aligned} \quad (4.12)$$

The steps to follow in calculating the surface error are therefore:

- 1 - Interpolate the data from a polar to a cartesian coordinate system.
- 2 - Perform the FFT on the interpolated data.
- 3 - Perform the phase shift by multiplying by $e^{jkz_0 \cos(\theta)}$.
- 4 - Perform the probe compensation calculations to achieve the true $T(u, v)$.
- 5 - Perform the IFFT on the $T(u, v)$.
- 6 - Find the least-squared quadratic, linear and the constant offset phase errors.
- 7 - Calculate the ϵ_λ of the data.

Test Case Results

The theory and implementation techniques discussed in the previous sections were tested on special cases of near-field data. In order to verify the software, a set of near-field

data from a parabolic reflector with a known distortion is desirable. Because of the lack of any measured near-field data with a known distortion, a test file of uniform amplitude and phase was chosen. This test file is similar to the ones used in previous chapters to verify operation of the interpolation and far-field parameter software. In addition, the type of distortions which are simulated are similar to the displaced panel tests which are used by Rahmat-Samii [1985] in the algorithm verification for distortions on large reflectors. The expected value of distortion to be calculated for a test file of this type would be uniformly equal to zero. This simple experiment was performed and the results indicated the expected value of zero.

The next case which could be of any use would be one in which the phase of the uniform test field was perturbed a known amount in the scan aperture. If the scan aperture is not located far from the feed aperture, the expected phase difference due to the surface of the reflector would be $1/2$ that in the aperture: $1/2$ for each direction of a round trip path from point p' to p to q as shown in figure 4.2. A test file of uniform amplitude and phase as described by Equation 2.1 which consisted of data on 63 rings was created. The phase of this uniform data, ψ , between rings $7.25\lambda \leq r \leq 9.75\lambda$ was shifted by $\psi = 30^\circ$ for $30^\circ \leq \phi \leq 60^\circ$, and by $\psi = 60^\circ$ for $280^\circ \leq \phi \leq 290^\circ$. It was then interpolated to a cartesian coordinate system which consisted of 129×129 scans spaced $1/2\lambda$ apart. The value of distance from the scan plane to the focal plane was chosen to be $z_0 = \lambda/4$ and the probe was an ideal dipole. This is illustrated in Figure 4.3. The results are shown in Figures 4.4 through 4.7 as contour plots of phase-vs-location in the xy -plane.

The phase of the H_x and H_y fields as generated are shown in Figure 4.4. This figure shows the constant contours of the phase for $\psi = 0.5^{\text{rad}}$ and $\psi = 0.8^{\text{rad}}$ for the H_x field, and constant contours of the phase for $\psi = -1.2^{\text{rad}}$ and $\psi = -0.6^{\text{rad}}$ for the H_y field. The contours are reasonable since the phase of the H_x was shifted from $\psi = 0^{\text{rad}}$ to $\psi = 0.52^{\text{rad}}$ in one location, and from $\psi = 0^{\text{rad}}$ to $\psi = 1.05^{\text{rad}}$ in the other location. For the H_y field, the phase was increased from $\psi = -\pi/2$ to values of $\psi = -\pi/2 + 0.52$ and $\psi = -\pi/2 + 1.05$.

Figure 4.5 shows the resultant phase of the field upon return from the IFFT routine after the $e^{jkz_0\cos(\theta)}$ and probe compensation factors have been applied. The results match the input to the FFT and are as expected, given the small value of aperture separation, z_0 .

Figure 4.6 shows the resultant phase after the quadratic, linear, and constant phase errors have been eliminated. At this point, the phase contours of each plot are identical due to the removal of the constant phase difference.

Figure 4.7 shows the final result of the surface deviation as a function of the wavelength. The $\lambda = 0.04$ and $\lambda = 0.08$ contours are shown. These values correspond to phase errors on the reflector surface of 14.4° and 28.8° , which are approximately equal to the $1/2$ factor of the phase difference in the aperture as discussed in above.

For all of the figures, a double contour is seen at the $280^\circ \leq \phi \leq 290^\circ$ location. This is due to the fact that both the $\psi = 30^\circ$ and $\psi = 60^\circ$ phase difference both appear at that location. Only the $\psi = 30^\circ$ phase difference appears at the $30^\circ \leq \phi \leq 60^\circ$ location. This is one reason that the different values of phase change were chosen.

Conclusions

Since a set of controlled test data which consists of real measurements and which used a feed of known illumination pattern is not available, the ability to completely verify that the software implementation is correct was not possible. However, the test runs using the perturbed phase uniform amplitude data demonstrated a good degree of confidence that the technique will recover the assumed distortions on the surface of the reflector. Using this technique, the antenna designer may better understand the various ways in which the reflector may be distorted: by feed support strut loads, temperature gradients, assembly techniques, mishandling, and others. Thus, the use of near-field data may prove to be a useful diagnostic tool for the future.

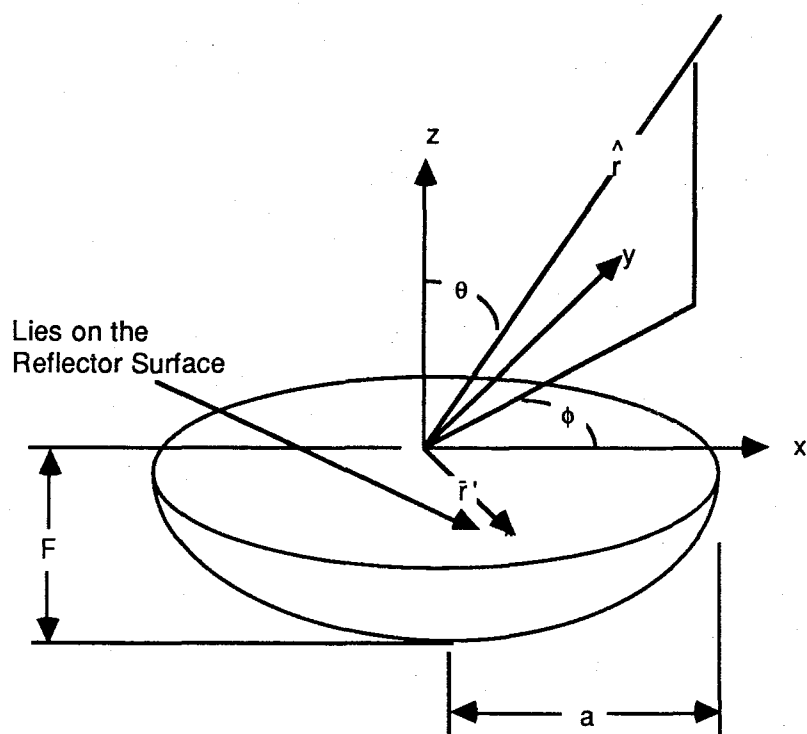


Figure 4.1 The Coordinate System Used to Define the Far-Field Quantity $T(u,v)$

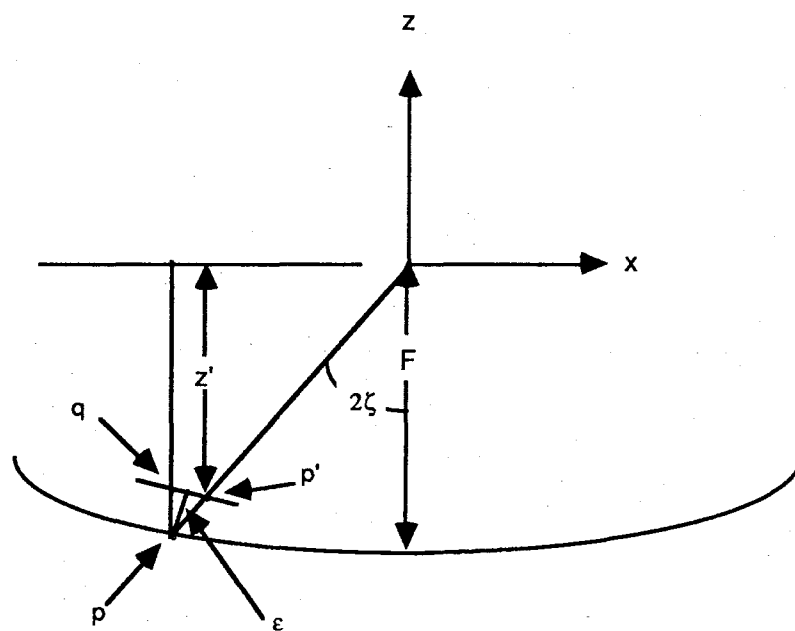


Figure 4.2 The Description of the Surface Error of a Parabolic Reflector

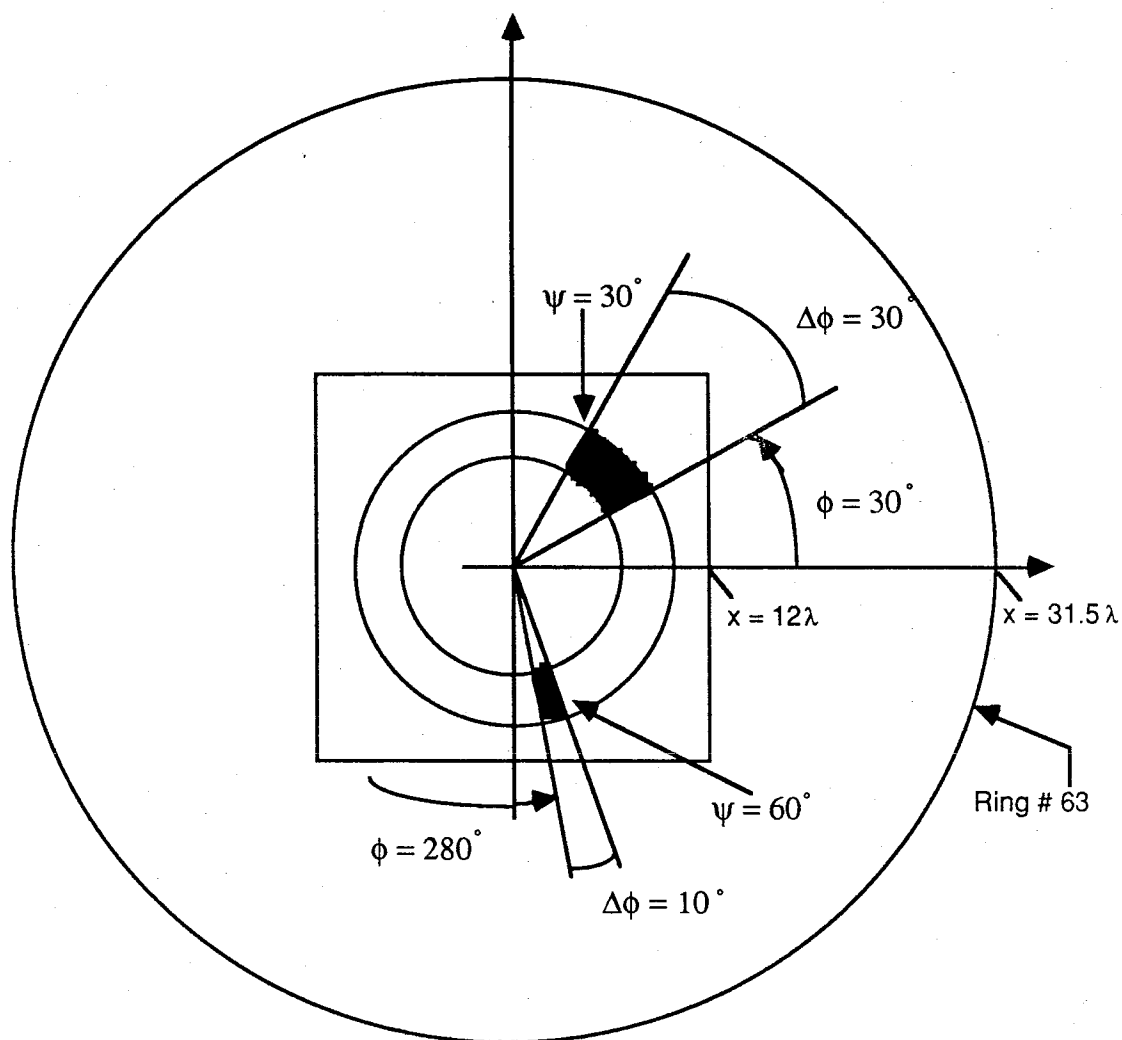


Figure 4.3 Illustration of the Test Case Showing the Constant Distortions in the Phase, the Maximum Distance of the Measurement and the Square Window Which is Viewed in the Figures 4.4 to 4.7

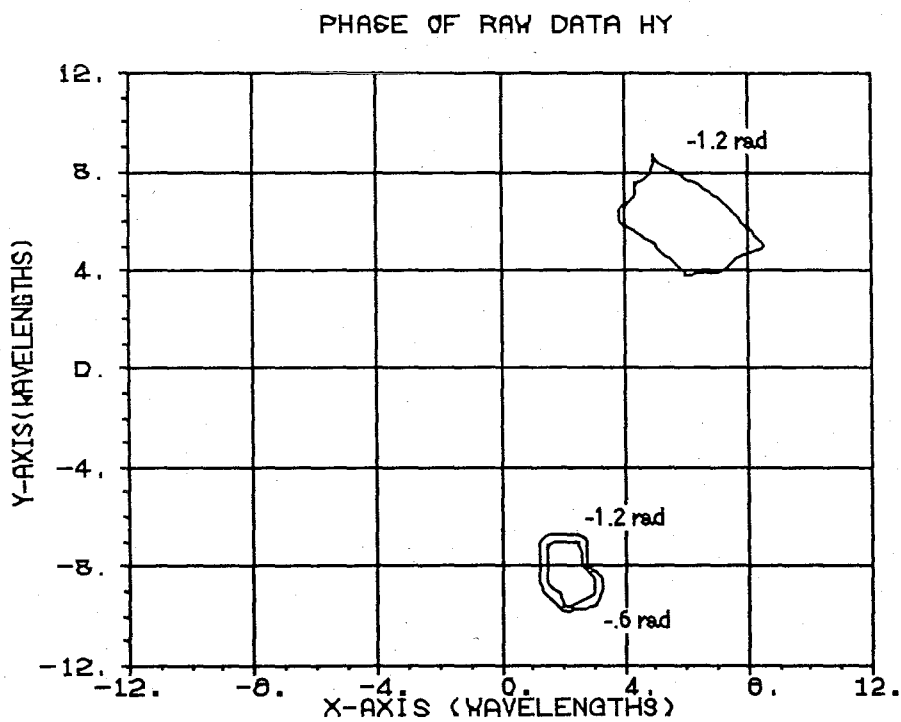
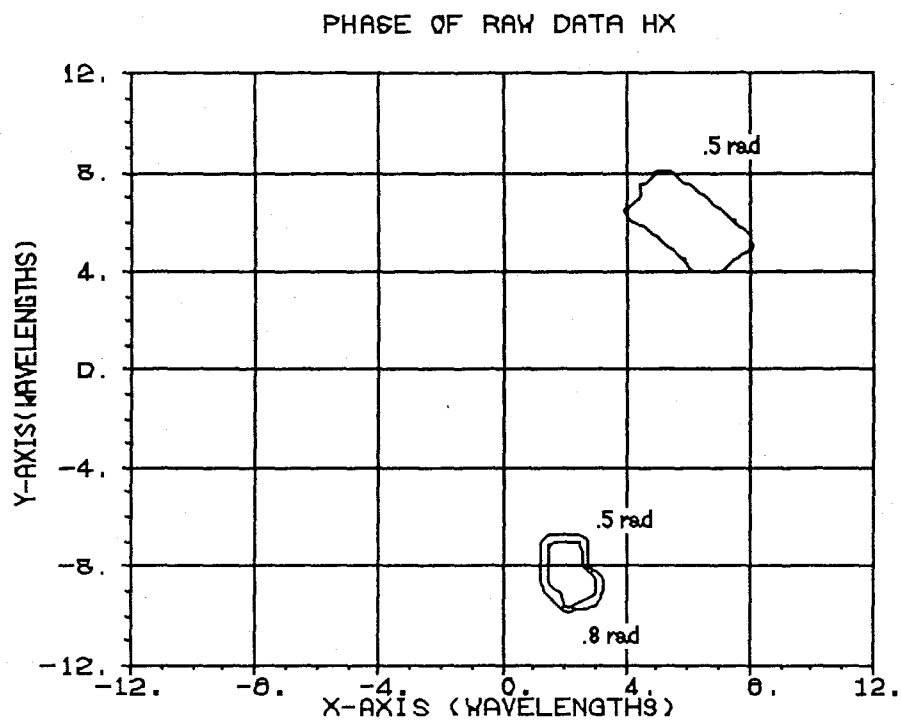


Figure 4.4 Phase of the Raw Data in the Measurement Plane for the Uniform Test Case

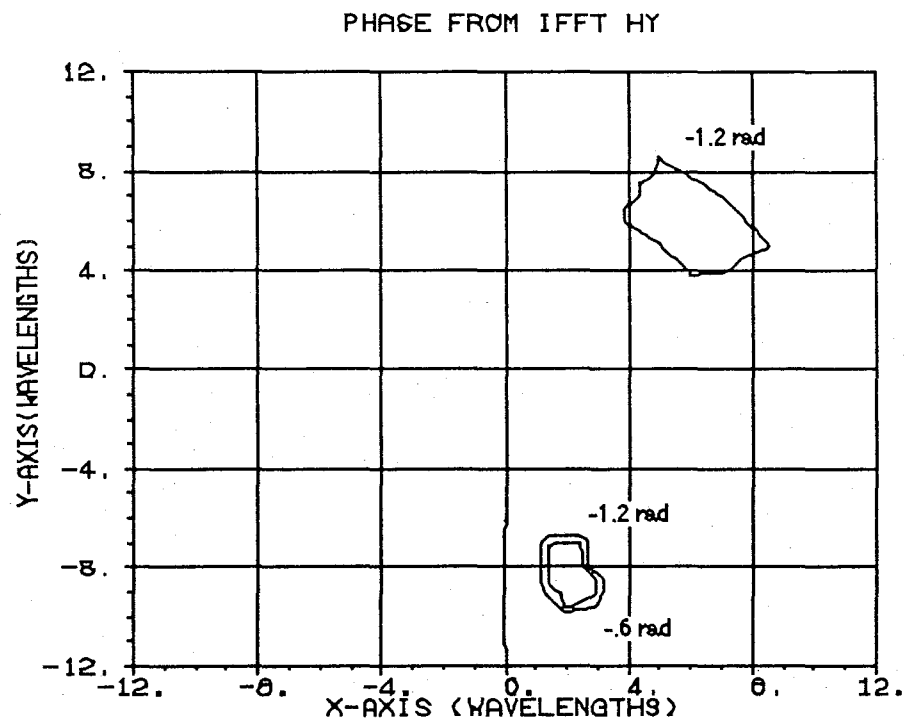
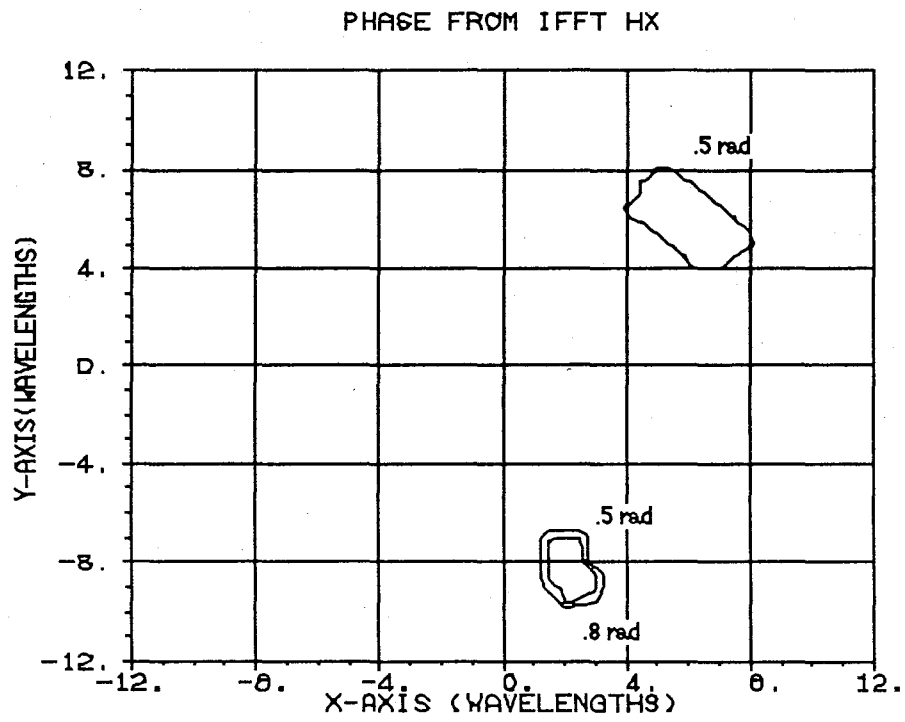


Figure 4.5 Phase of the Data After the IFFT for the Uniform Test Case

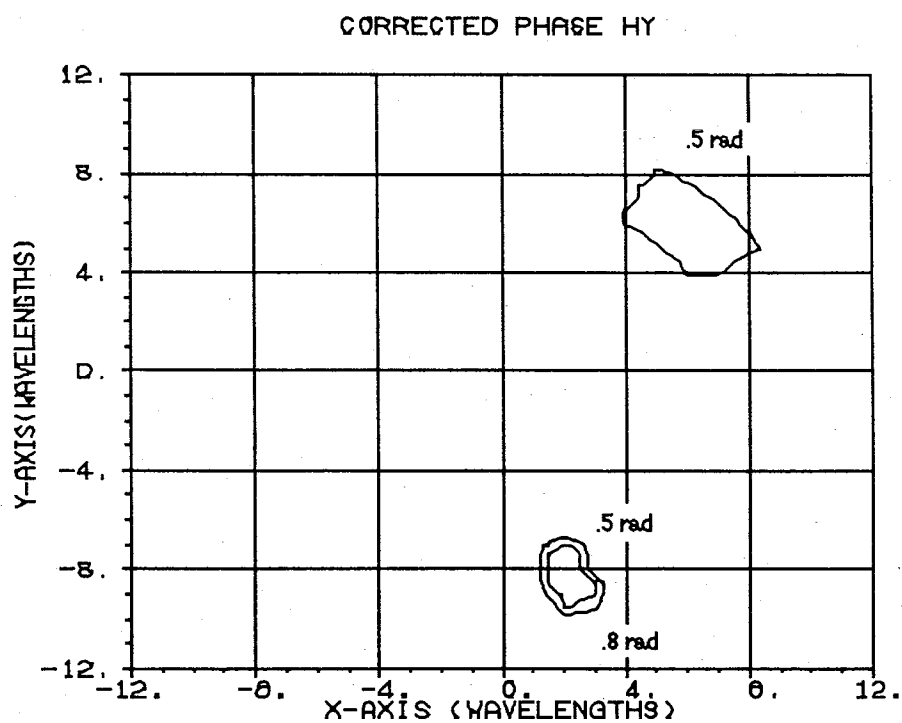
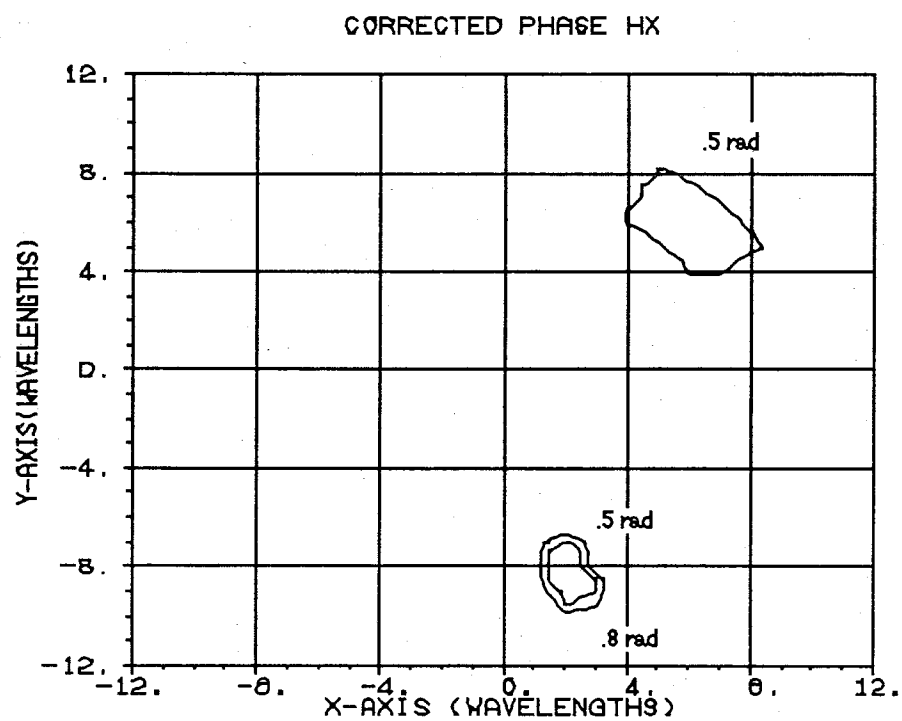


Figure 4.6 Phase Corrected for Quadratic Errors for the Uniform Test Case

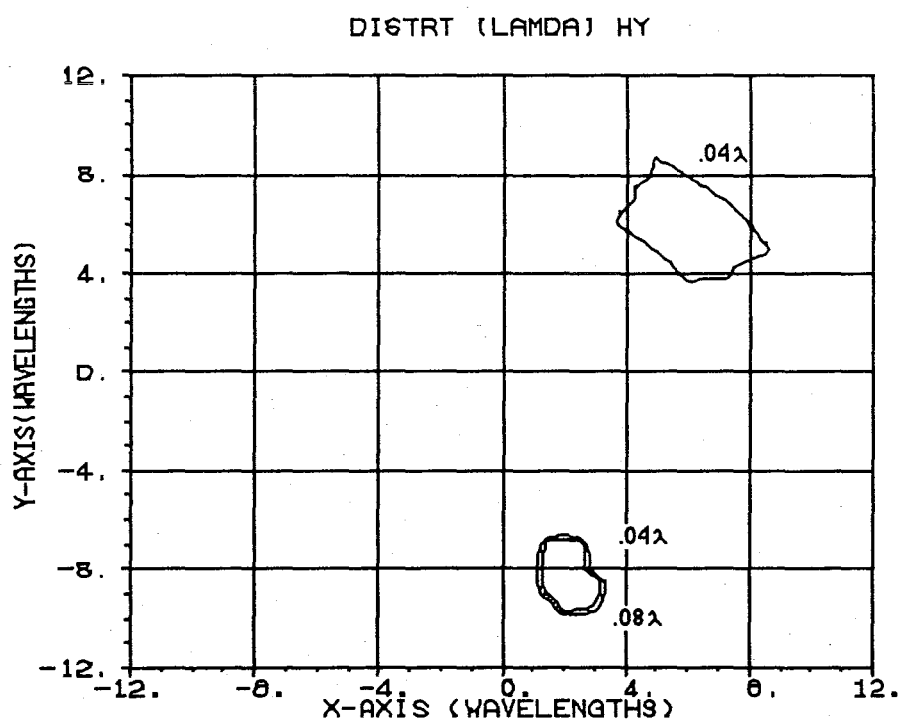
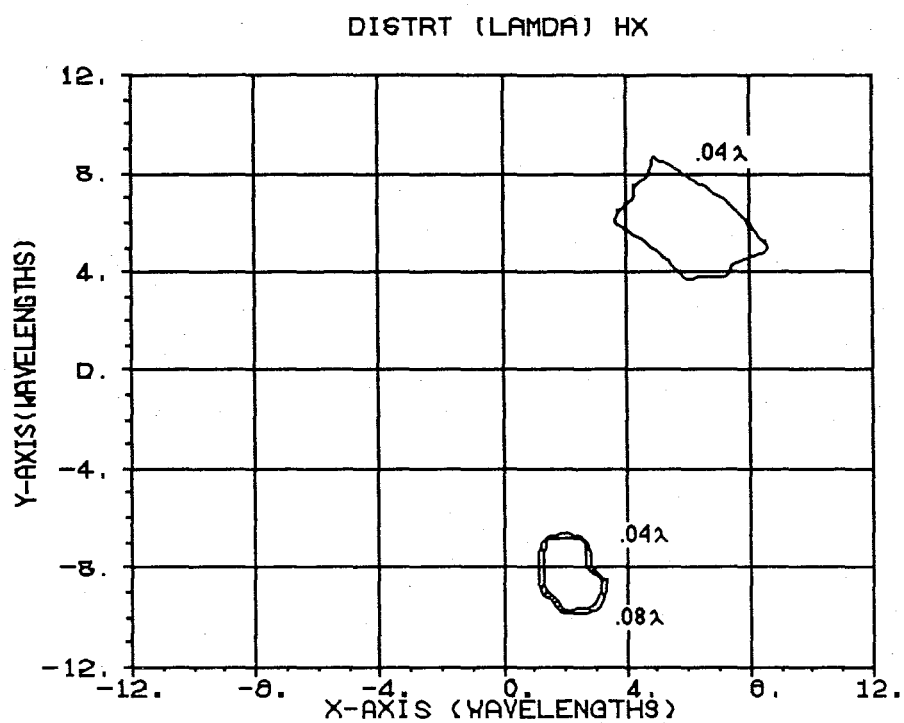


Figure 4.7 Distortion of the Reflector in Wavelengths for the Uniform Test Case

Chapter 5

THESIS CONCLUSIONS

The primary purpose of this thesis was to utilize the FFT in the calculation of the far-field patterns of an antenna which was measured on a plane-polar near-field antenna range. This capability would be in addition to the use of the Jacobi-Bessel technique which is specifically designed for the plane-polar coordinate system. The discussions of the different ways in which the near-field data could be measured were presented in Chapter 1. The planar measurement techniques were discussed in more detail, and in particular the plane-polar technique was defined. The planar near-field facility at the JPL is only capable of measuring data in the plane-polar format, thus, the data which exists from previous measurements of the Viking high gain antenna may be used to compare the results of the calculations by both the FFT and the Jacobi-Bessel techniques.

Interpolation Results

In order to use the FFT algorithm in calculating the far-field of the antenna under test, the measured data has to lay on grid lines of a rectangular coordinate system. The data obtained from the actual near-field measurements is in polar form on concentric rings. An interpolation was developed in Chapter 2 which was capable of defining the complex field values on the rectangular coordinate system given the field values on the polar coordinate system. The interpolation which was chosen was the 4-point bivariate Lagrange technique. This technique was chosen on the basis of simplicity, efficiency, speed, and accuracy. The interpolation was applied to an actual set of near-field data of the Viking high gain antenna. In addition, the interpolation was performed on the data in the Cartesian form of the complex field value and the polar form of the complex field value. The interpolation was checked by comparisons of the data as measured from the polar coordinate system to the interpolated value in the rectangular coordinate system. These comparisons were carried out for the principal plane cuts of the coordinate system, namely the x-axis ($\phi=0^\circ$) and the y-axis ($\phi=90^\circ$).

It was demonstrated that either representation of the data was acceptable for purposes of the interpolation; however, since the Cartesian form is linear in the interpolated variables, and the polar form could cause ambiguities in the phase of 180° , the Cartesian form was recommended as the desirable form to interpolate. Finally, the CPU and total run times of the interpolation on the UNIVAC were given, and suggestions made as to a technique whereby the total time could be reduced, namely the use of virtual memory features of the ASCII FORTRAN compiler.

Calculation of the Far-Field Parameters

Chapter 3 developed the equations which were necessary to use the FFT in the calculation of the radiation integral which resulted from the convolution of the probe with the antenna under test. The transform variables u and v were defined, and their relationship to the FFT output were given. In particular, these variables are the ones which are useful for the calculation of the far-field quantities from the near-field data. It was shown that the input to the FFT was the near-field data which lay on the rectangular grid, and that the positions on the grid were in terms of the wavelength. The electric far-field co- and cross-polarized pattern was then defined, and its use in calculating other quantities such as the polarization properties of the antenna were shown. A comparison of the far-field patterns of the Viking HGA as calculated by the FFT and the Jacobi-Bessel techniques was made. The results indicated that the FFT technique could reproduce the results for which the Jacobi-Bessel technique converged. The Jacobi-Bessel technique has been proven to reproduce the far-field results of the antenna under test in the past. In fact, the Jacobi-Bessel technique converged to an angle which was less than the maximum possible angle as shown in Figure 3.6, given the edge of the data for the coefficients $n=m=10$. More coefficients would allow convergence up to this angle. Since the FFT technique matched the Jacobi-Bessel technique in the region of the convergence of the Jacobi-Bessel polynomial, it may be assumed that the FFT technique will therefore reproduce the actual far field to the maximum

possible angle as defined in Figure 3.6, assuming that the sampling criteria was observed in the measurement. Also this accuracy is achieved without the need for an iteration to determine the region of convergence.

The FFT routine will provide accurate results along the principal plane cuts very rapidly, however, for any off principal plane cuts, the routine requires a much greater time to yield results. This is because of the interpolation used to find the field value at a point which does not lie on the grid system. For these cuts the Jacobi-Bessel technique will require the same amount of computer time as the principal plane cuts. The total time required to calculate the far-field pattern for the principal plane and the $\phi = 45^\circ$ cuts were calculated for both the FFT and the Jacobi-Bessel technique for the Viking HGA. The total time favored the FFT technique by 2 minutes. For this antenna the principal plane cuts are more rapidly calculated by the FFT technique. For larger antennas this would not necessarily be true. In fact, if the FFT size is 256×256 , the time to calculate the field pattern alone will increase by a factor of 4. The interpolation time would also increase by this factor.

Diagnosis

The ability to use the near-field data to calculate the surface distortions of a parabolic reflector antenna was discussed in Chapter 4. The equations which are useful in this calculation were shown and the use of the FFT was illustrated. By properly defining the transform variables u and v , as shown in Chapter 3, the FFT algorithm previously developed could be used with no change. A series of steps were detailed which could be followed to calculate the surface distortions. These steps were then integrated into a FORTRAN program and tested on a hypothetical set of near-field data. The phase of the test data was perturbed slightly and the effects of the perturbation were calculated at the surface of a hypothetical reflector. The effects which were calculated were as predicted, given the phase distortion in the measurement plane. A good degree of confidence was shown that this technique would be useful in determining the various ways in which the reflector may be distorted.

Summary

To summarize, this thesis has demonstrated that the use of the FFT to calculate the far-field parameters of an antenna from a plane-polar near-field measurement is feasible. The interpolation from the polar coordinate system to the rectangular coordinate system may be done in a reasonable amount of computer time. This number represents 256 scans spaced $1/2 \lambda$ apart and centered about the rectangular coordinate system. The results of the far-field patterns agree well with techniques which have been previously proven accurate. In addition, the use of the near-field data in calculating the surface distortions of parabolic reflector antennas has been demonstrated.

References

- Abramowitz, M., and Stegun, I. A., ed., Handbook of Mathematical Functions, National Bureau of Standards, Applied Mathematics Series-55, 1964.
- Appel-Hansen, J., in Chapter 8, Vol 1, The Handbook of Antenna Design, Rudge, A. W., Milne, K., Olver, A. D., and Knight, P., editors, Peter Peregrinus, London, 1982.
- Baird, R. C., Newell, A. C., Wacker, P. F., Kerns, D. M., Recent Experimental Results in Near-Field Antenna Measurements, Electronics Letters, Vol 6, 349-351, May 28, 1970.
- Bennett, J. C., Anderson, A. P., McInnes, P. A., and Whitaker, A. J. T., Microwave Holographic Metrology of Large Reflector Antennas, IEEE Transactions on Antennas and Propagation, Vol AP-24, 295-303, 1976.
- Bennett, J. C., The Plane-Polar Approach to Near-Field/Far-Field Transformation - An Alternate Algorithm, IEE Colloquium on New Developments and Techniques in Antenna Measurements, 29 Jan 1985, London, Digest p. 2/1-2/4.
- Cooley, J. W., and Tukey, J. W., An Algorithm for the Machine Calculation of Complex Fourier Series, Math. Computation, Vol 19, 297-301, April 1965.
- Ferziger, J. D., Numerical Methods for Engineering Application, John Wiley and Sons, 1981.
- IEEE Standard Definitions of Terms for Antennas, IEEE STD 145-1983, The Institute of Electrical and Electronics Engineers, 1983.
- IEEE Standard Test Procedures for Antennas, IEEE STD 149-1979, The Institute of Electrical and Electronics Engineers, 1979.
- Johnson, R. C., Ecker, H. A., and Hollis, J. S., Determination of Far Field Antenna Patterns from Near Field Measurements, Proceedings of the IEEE, Vol 61, No 12, 1668-1694, Dec 1973.
- Joy, E. B., and Paris D. T., Spatial Sampling and Filtering in Near Field Measurements, IEEE Transactions on Antennas and Propagation, Vol AP-20, 253-261, May 1972.
- Joy, E. B., Leach, W. M., Rodrigue, G. P., and Paris, D. T., Application of Probe-Compensated Near-Field Measurements, IEEE Transactions on Antennas and Propagation, Vol AP-26, No 3, 379-389, May 1978.
- Kerns, D. M., Correction of Near-Field Antenna Measurements Made With An Arbitrary but Known Measuring Antenna, Electronics Letters, Vol 6, 11-17, January 1950.
- Kerns, D. M., and Dayhoff, E. S., Theory of Diffraction in Microwave Interferometry, Journal Res. National Bureau of Standards, Vol 64B, 1-13, January-March 1960.
- Kerns, D. M., Plane-Wave Scattering-Matrix Theory of Antennas and Antenna-Antenna Interactions, NBS Monograph 162, U.S. Govt Printing Office, Washington, DC, June 1981.
- Kreyszig, E., Advanced Engineering Mathematics, 4th Ed., John Wiley & Sons, New York, 1979.
- Newell, A. C., Baird, R. C., and Wacker, P. F., Accurate Measurement of Antenna Gain and Polarization at Reduced Distances by an Extrapolation Technique, IEEE Transactions on Antennas and Propagation, Vol AP-21, 418-431, July 1973.

Newell, A. C., Planar Near-Field Measurements, NBS Lecture Notes, Boulder, Co, June 1985.

Ngai, E. C., and Profera, C. E. Application of Bivariate Interpolation To Antenna Related Problems, IEEE Transactions on Antennas and Propagation, Vol AP-31, No 7, July 1984.

Oppenheim, A. V., and Schafer, R. W, Digital Signal Processing, Prentice Hall, Englewood Cliffs, NJ, 1975.

Rabiner, and Gold, Theory and Application of Digital Signal Processing, Prentice Hall, Englewood Cliffs, NJ, 1975.

Paris, D. T., Leach, W. M., and Joy, E. B., Probe-Compensated Near-Field Measurements on a Cylinder, IEEE Transactions on Antennas and Propagation, Vol AP 21, 435-445, 1973.

Paris, D. T., Leach, W. M., and Joy, E. B., Basic Theory of Probe-Compensated Near-Field Measurements, IEEE Transactions on Antennas and Propagation, Vol AP-26, No 3, 373-379, May 1978.

Rahmat-Samii, Y., Galindo-Israel, V., and Mittra, R., A Plane-Polar Approach for Far-Field Construction from Near-Field Measurements, IEEE Transactions on Antennas and Propagation, Vol AP-25, No 2, 216-230, March 1980.

Rahmat-Samii, Y., Surface Diagnosis of Large Reflector Antennas Using Microwave Holographic Metrology: An Iterative Approach, Radio Science, Vol 19, No 5, 1205-1217, Sept/Oct 1984.

Rahmat-Samii, Y., and Gatti, M. S., Far-Field Patterns of Spaceborne Antennas from Plane-Polar Near-Field Measurements, IEEE Transactions on Antennas and Propagation, Vol AP-33, No 6, 638-648, June 1985.

Rahmat-Samii, Y., Microwave Holography of Large Reflector Antennas - Simulation Algorithms, IEEE Transactions on Antennas and Propagation, Vol AP-33, No 11, 1194-1203, November 1985.

Ransom, P. L., Evaluation of the Fourier Integral Using the Fast Fourier Transform, University of Illinois Dept of Electrical Engineering, Antenna Laboratory Report No 72-9, September 1972.

Yaghjian, A. D., Upper Bound Errors in Far-Field Antenna Parameters Determined from Planar Near-Field Measurements, Part 1, NBS Technical Note 667, October 1975.

Yaghjian, A. D., An Overview of Near-Field Antenna Measurements, IEEE Transactions on Antennas and Propagation, Vol AP-34, No 1, 30-45, January 1986.

Appendix A

THE BIVARIATE LAGRANGE INTERPOLATION

Interpolation Requirements

The basic problem of the interpolation required is that if one is given a set of data (x_i, y_i, z_i) , it is desired to find a smooth curve $z = F(x, y)$ which passes through the data. A typical interpolation algorithm has the following characteristics [Ferziger, 1981]:

1. $F(x_i, y_i) = z_i$
2. Easy evaluation
3. Easy to integrate & differentiate
4. Linear in the adjustable parameters

Two interpolation techniques are often considered: the Lagrange and the cubic spline. The cubic spline has some advantages over the Lagrange interpolation. The cubic spline is more accurate as more points are used, i.e., in higher orders, and its first two derivatives are continuous. However, this technique is more difficult to implement at the end points where the definition of the end condition will affect the results. Ngai and Profera [1984] have suggested that the Lagrange interpolation is useful and sufficiently accurate in the various aspects of antenna calculations. The Lagrange interpolation will be discussed in detail and its applications to this thesis shown.

1-Dimensional Interpolation

Begin by considering the 1-dimensional case where there are only ordered pairs of data (x_i, y_i) and we desire $f(x_i) = y_i$. The interpolation formula is

$$f(x) = a_{n-1}x^{n-1} + a_{n-2}x^{n-2} + \dots + a_1x + a_0 \quad (A1)$$

We desire the coefficients, a_i , of this equation. One could use the data points, and the definition:

$$f(x_i) = y_i \quad (A2)$$

to arrive at a set of $n-1$ equations in $n-1$ unknowns. The solution to this matrix is easy; however for $n > 5$ the system often becomes ill conditioned [Kreyszig, 1979]. Instead, note that from Equation A1 that the a_i are linear combinations of the y_i . The general expression for a linear equation in x of degree $n-1$ is:

$$f(x) = \sum_{k=1}^n L_k(x) y_k \quad (A3)$$

Substitution of this into Equation A2 yields

$$\begin{aligned} L_k(x_i) &= 1 \quad i = k \\ &= 0 \quad i \neq k \\ i &= 1, 2, \dots, n \end{aligned} \quad (A4)$$

In this equation, the choice of k is arbitrary, so it must hold for all k . Therefore $L_k(x_i)$ is a polynomial that is zero for all x_i , $i \neq k$, and is unity for x_i , $i = k$, and one can write the $L_k(x_i)$ as a multiple of the $n-1$ factors of its zeroes,

$$L_k(x_i) = C_k (x-x_1) (x-x_2) \dots (x-x_{k-1}) (x-x_{k+1}) \dots (x-x_n) \quad (A5)$$

where the C_k is a constant. This constant is determined by the requirement that the $L_k(x_k) = 1$ as given by Equation A4. Therefore, one can write C_k as

$$C_k = [(x_k-x_1) (x_k-x_2) \dots (x_k-x_{k-1}) (x_k-x_{k+1}) \dots (x_k-x_n)]^{-1} \quad (A6)$$

and finally the polynomial may be expressed as,

$$L_k(x) = \prod_{\substack{i=1 \\ i \neq k}}^n \left(\frac{x-x_i}{x_k-x_i} \right) \quad (A7)$$

The interpolation formula defined by Equations A3 and A7 comprises the n -point Lagrange interpolation. This formula is guaranteed to pass smoothly through the data points given. It seems obvious that the higher the order of interpolation, i.e., the more points used, the more time consuming the algorithm becomes. In the limiting case where 2 points are used, the interpolation is linear. For this case, the Lagrange polynomials are:

$$\begin{aligned} L_1(x) &= (x-x_2) / (x_1-x_2) \\ L_2(x) &= (x-x_1) / (x_2-x_1) \end{aligned} \quad (A8)$$

and the interpolation formula is

$$f(x) = \frac{(x-x_2)}{(x_1-x_2)} y_1 + \frac{(x-x_1)}{(x_2-x_1)} y_2 \quad (A9)$$

2-Dimensional Interpolation

The natural extension to the 1-dimensional Lagrange formula is the 2-dimensional formula. In this case, the data consists of ordered triplets (x_i, y_i, z_i) . For this thesis the x_i and y_i are the positions of the field quantity in the r, ϕ plane at constant values of r and ϕ , and the z_i is a complex number representing the value of the field quantity at that point. The formula for the bivariate Lagrange interpolation can be written in a form similar to Equation A3 as shown by Ngai and Profera [1984] and Abramowitz and Stegun [1964]. This form is:

$$f(x, y) = \sum_{m=1}^M \sum_{n=1}^N X_{m,i}(x) Y_{n,j}(y) f(x_i, y_j) \quad (A10)$$

where

$$X_{m,i}(x) = \prod_{\substack{k=1 \\ k \neq i}}^m \left(\frac{x-x_k}{x_i-x_k} \right) \quad Y_{n,j}(y) = \prod_{\substack{k=1 \\ k \neq j}}^n \left(\frac{y-y_k}{y_j-y_k} \right) \quad (A11)$$

$$i = 1, 2, \dots, m \quad j = 1, 2, \dots, n$$

If $N=M=2$, then the bivariate linear Lagrange interpolation results. The formula which results from this choice of N and M is given below, where the indices are illustrated in Figure A1.

$$f(x, y) = \left(\frac{x-x_2}{x_1-x_2} \right) \left(\frac{y-y_2}{y_1-y_2} \right) f(x_1, y_1) + \left(\frac{x-x_2}{x_1-x_2} \right) \left(\frac{y-y_1}{y_2-y_1} \right) f(x_1, y_2) \\ + \left(\frac{x-x_1}{x_2-x_1} \right) \left(\frac{y-y_2}{y_1-y_2} \right) f(x_2, y_1) + \left(\frac{x-x_1}{x_2-x_1} \right) \left(\frac{y-y_1}{y_2-y_1} \right) f(x_2, y_2) \quad (A12)$$

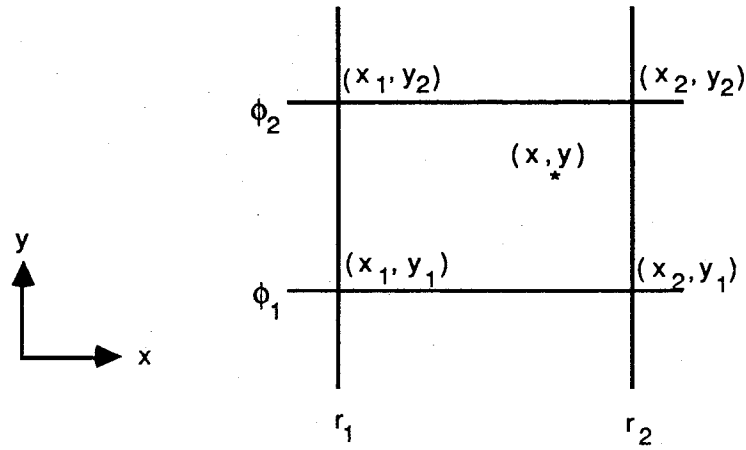


Figure A1. The Coordinate System Used for the Bivariate Lagrange Interpolation

Appendix B

FFT ALGORITHMS USED IN ANTENNA CALCULATIONS

FFT Algorithms

The one dimensional Continuous Fourier Transform (CFT) is typically defined in electromagnetic theory by:

$$F(u) = \int_{-\infty}^{\infty} e^{j2\pi ux} f(x) dx \quad (B1)$$

The integration of this equation may become tedious because of the oscillatory nature of the kernel. One of the techniques is the use of the Discrete Fourier Transform (DFT) which is given by:

$$F(m\Delta u) = \Delta x \sum_{n=-N/2}^{N/2-1} f(n\Delta x) e^{j2\pi nm/N} \quad -N/2 \leq m \leq N/2 \quad (B2)$$

where $f(n\Delta x)$ and $F(m\Delta u)$ are sampled versions of the continuous functions $f(x)$ and $F(u)$. Notice in this definition that the number of sample points of $F(u)$ is equal to the number of sample points of $f(x)$. By using the DFT representation of the CFT one may use the efficient Fast Fourier Transform (FFT) algorithm [Cooley and Tukey, 1965] for the computation of the CFT.

For the FFT to be applied, the function $f(x)$ must be band limited to a given range, i.e.,

$$f(x) = 0 \quad |x| > a \quad (B3)$$

It can be shown that $F(u)$ will not be strictly limited to any band in u , but that if $f(x)$ is smooth enough, the magnitude $|F(u)|$ will be essentially contained in a band $[\alpha, \alpha]$. These relationships are shown in Figure B1.

In order to apply the FFT algorithm to the function $f(x)$, this function must be appropriately sampled. Let the number of samples be N , and let $f(x)$ be sampled at intervals of Δx over a range $[-T/2, T/2]$ such that

$$N = T / \Delta x \quad (B4)$$

This is shown in figure B2. Since the sampling indices n and m in equation B2 take on values between $-N/2$ and $N/2 - 1$, Equation B4 can be used to show the relationship between the parameters x and u [Ransom, 1972, p4]

Table B1. The Relationship Between the FFT Parameters x and u

	x	u
Sampling Range	T	$1/\Delta x$
Sampling Interval	Δx	$1/T$

FFT Implementations

FFT implementations of Equation B2 may be found in many literature discussions. However, most of these discussions deal with digital processing of signals which are causal, i.e., which do not exist for negative values of the parameter x . In this case, the function $g(x)$ which is shown in Figure B1 would appear as given in figure B3. The Fourier transform of $g(x)$, denoted $G(u)$, will have a magnitude which is equal to the magnitude of $F(u)$; however, the phase of $G(u)$ will not equal the phase of $F(u)$. This means that if one were to use any FFT which is designed for causal systems to solve the Equation B1 where the $f(x)$ is not causal, incorrect phase results would be calculated. This is the situation in antenna theory where the aperture distribution is the function $f(x)$ and is in the range $[-a, a]$. To utilize these FFTs, one would have to perform a phase shift of the output data. The phase shift is done in the following manner: given a sequence

$$f(n\Delta x) : n = -N/2, -N/2+1, \dots, N/2-1 \quad (B5)$$

$$f(-N/2) = -T/2 \text{ and } F(N/2) = T/2$$

If this sequence is shifted to the right by $N/2 \Delta x$, a causal sequence results as given in figure B3. The Fourier transform of this sequence is [Oppenheim and Schaffer, 1975, p92]

$$\begin{aligned} F\{g(n\Delta x)\} &= F\{f(n\Delta x - N/2 \Delta x)\} \\ &= e^{-j\omega N/2} F\{f(n\Delta x)\} \end{aligned} \quad (B6)$$

so that

$$F\{f(n\Delta x)\} = e^{j\omega N/2} F\{g(n\Delta x)\} \quad (B7)$$

and to correct for the phase error one would use the exponential factor at each point where the digital frequency, ω , is given by $\omega = u\Delta x$. The FFT algorithm used in this thesis is from Ransom [1972] and already accounts for this shift on the output so that the user does not have to.

An interesting point to note is that in most communication and digital signal processing applications, the definition of the CFT includes a negative sign in the exponent of the kernel of Equation B1 instead of a positive sign. This definition poses no problem since the DFT and its inverse, IDFT, have a very similar form with the exception to the sign of the exponent and a constant factor. As such the FFT may be used in evaluation of the IDFT as well as the DFT. Therefore, if the FFT implementation used is based on a definition which is different than the one of interest, the user may just choose to perform a synthesis instead of an analysis. Again, the algorithm used in this thesis allows for this difference in definitions.

The 2-Dimensional CFT

The CFT as shown in Equation B1 is a 1-dimensional transform. In the work done in this thesis, the transforms are 2-dimensional in nature. In this case the CFT is given by:

$$F(u,v) = \int_{-\infty}^{\infty} \int_{-\infty}^{\infty} f(x,y) e^{j2\pi(xu + yv)} dx dy \quad (B8)$$

It can be shown that the associated 2-dimensional DFT is given by:

(B9)

$$F(p\Delta u, q\Delta v) = \Delta x \Delta y \sum_{n=-N_u/2}^{N_u/2-1} \sum_{m=-N_v/2}^{N_v/2-1} f(n\Delta x, m\Delta y) e^{i2\pi(np/N_u + mq/N_v)}$$

$$-N_u/2 \leq p \leq N_u/2$$

$$-N_v/2 \leq q \leq N_v/2$$

It can also be shown that the evaluation of this equation may be accomplished by a repeated application of the FFT. First the transform of the columns of the data in the x-y plane is performed, then a transformation of the rows. For this situation the 1-dimensional FFT may be applied by using a second subroutine which performs a bookkeeping function. One such subroutine is used in the evaluation of the 2-dimensional CFTs which occur in this thesis. The parameters in Equations B8 and B9 are very similar to those of Equation B1 and B2. In fact all of the relationships defined previously for the sample spacing and sample interval will hold in the 2-dimensional case as well.

Interpolation

The output of the FFT routine will be the sampled version of the CFT as given by Equation B2. This means that for an input function the CFT is calculated at different discrete values of u and that Equation B1 does not have to be calculated repeatedly for each u of interest. Unfortunately, the values of u for which the CFT is calculated may not be the ones in which one is interested. The solution to this problem is the use of an interpolation algorithm. All of the references for this appendix discuss one such interpolation. It is given in 2 dimensions by:

$$F(u, v) = \sum_{n=-N_u/2}^{N_u/2-1} \sum_{m=-N_v/2}^{N_v/2-1} F(n\Delta u, m\Delta v) \text{sinc}[\pi(u/\Delta u - n)] \text{sinc}[\pi(v/\Delta v - m)] \quad (\text{B10})$$

where the interpolation will be valid for any u - v combination as long as the function $f(x, y)$ is bandlimited as described by Equation B3.

It becomes obvious that as the number of samples in each direction increase, the interpolation will become slower since a double summation of all the points is being evaluated and there will be an evaluation of a trigonometric function at each step. Fortunately, there is a way to move the evaluation of the sine term outside the summation. Also, careful study of the equation will show that a complete double summation is not required when the point in question lays on a major grid line defined by the locations of the known values. In addition, if the point in question is on a given point from the FFT, no summation occurs as would be expected from a good interpolation formula. These principles are shown below. Note that:

$$\text{sinc}[\pi(u/\Delta u - n)] = \frac{\sin[\pi(u/\Delta u - n)]}{\pi(u/\Delta u - n)} = \frac{(-1)^n \sin(\pi u/\Delta u)}{\pi(u/\Delta u - n)} \quad (\text{B11})$$

This relationship will hold for both of the sine terms in Equation B10 and so each sine term may be calculated outside the summation and thus be evaluated only one time. By carrying out this manipulation Equation B10 may be rewritten as:

$$F(u, v) = \frac{1}{\pi^2} \sin(\pi u/\Delta u) \sin(\pi v/\Delta v) \sum_{n=-N_u/2}^{N_u/2-1} \sum_{m=-N_v/2}^{N_v/2-1} (-1)^{n+m} \frac{F(n\Delta u, m\Delta v)}{(u/\Delta u - n)(v/\Delta v - m)} \quad (\text{B12})$$

Careful inspection of Equation B12 will show that $u/\Delta u = n$ and $v/\Delta v = m$ represent points along given grid lines in the array. When this occurs the associated sinc term becomes unity and the associated summation disappears. The resulting equations to be used when this occurs are:

$$F(u, v) = \frac{1}{\pi} \sin(\pi u/\Delta u) \sum_{n=-N_u/2}^{N_u/2-1} (-1)^n \frac{F(n\Delta u, v)}{(u/\Delta u - n)} \quad ; v/\Delta v = m \quad (\text{B13})$$

$$F(u, v) = \frac{1}{\pi} \sin(\pi v/\Delta v) \sum_{m=-N_v/2}^{N_v/2-1} (-1)^m \frac{F(u, m\Delta v)}{(v/\Delta v - m)} \quad ; u/\Delta u = n$$

Sampling Criteria

Equation B2 represents one period of a periodic function of the variable u . If the index m were allowed to go beyond the limits given in Equation B2 the function could be as shown in Figure B4. This figure shows a DFT and its neighboring periods. These neighboring periods have the same shape and form of the principle DFT and are called aliases. The separation between the aliases is $1/\Delta x$ and the DFT will be essentially zero past $u = \alpha$. When the sampling in $f(x)$ is too large the $1/\Delta x$ becomes smaller and the aliases near the desired DFT will begin to overlap causing distortion as shown in Figure B5. Obviously, in order to minimize this distortion selection of Δx should be made to satisfy

$$\alpha = 1/2\Delta x \quad (B14)$$

$$\Delta x = 1/2\alpha$$

where α is the highest (spatial) frequency of the DFT. For an antenna application, the maximum spatial frequency is $\alpha = 1$ where the aperture distribution is normalized to the wavelength λ and the typical u - v parameters are being used (Chapter 3). It can be seen that for the aliases of the antenna pattern to remain in imaginary space, the sampling interval in the aperture distribution must remain less than $1/2\lambda$.

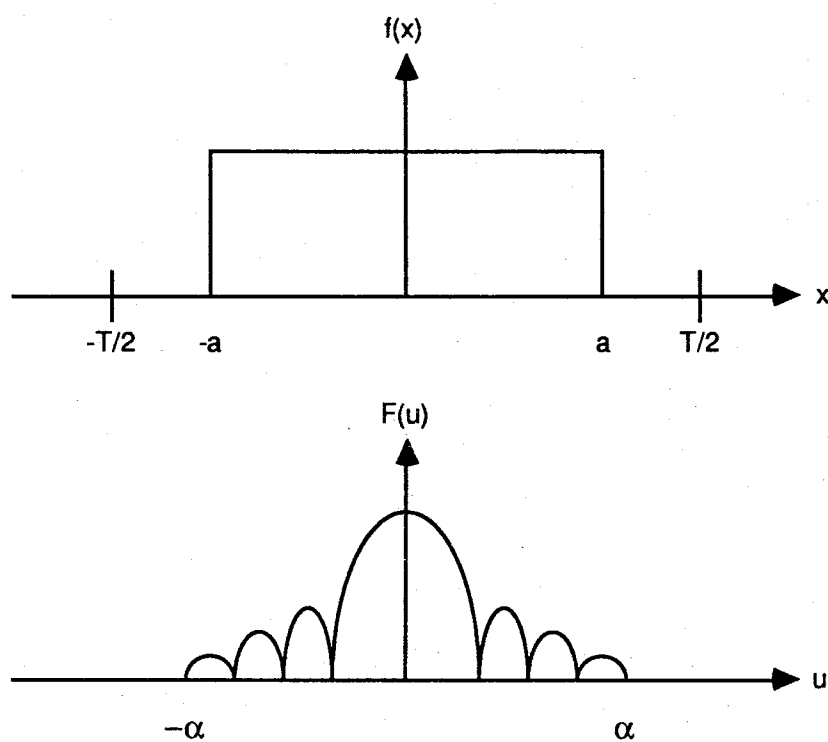


Figure B1. A Continuous Function $f(x)$ Limited in Range to $[-a,a]$ and its Continuous Fourier Transform, Essentially Bandlimited to $[-\alpha,\alpha]$

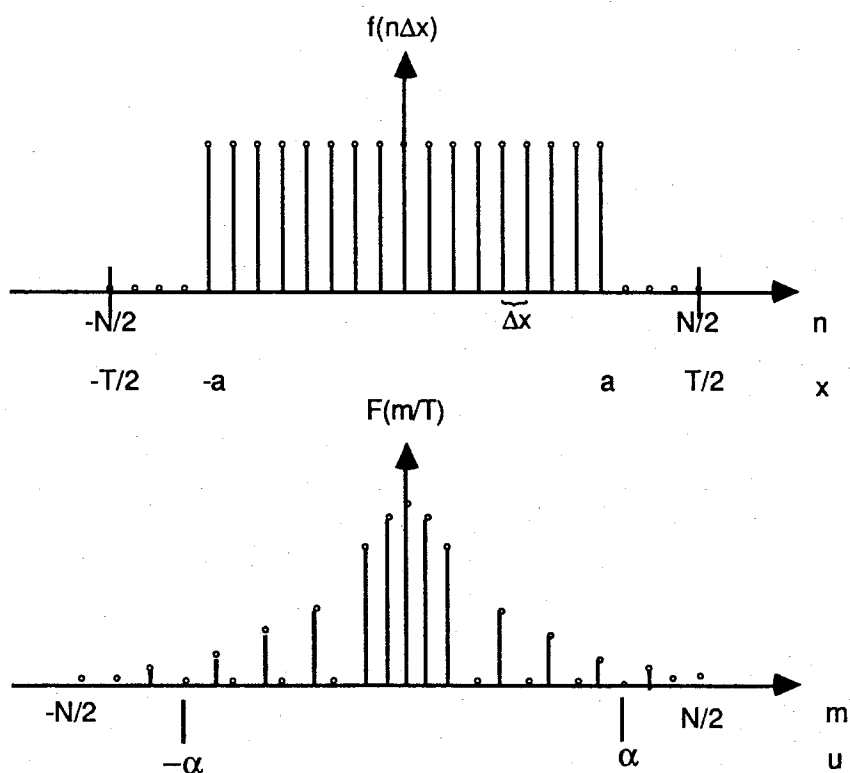


Figure B2. Sampled Versions of the Continuous Functions $f(x)$ and $F(u)$

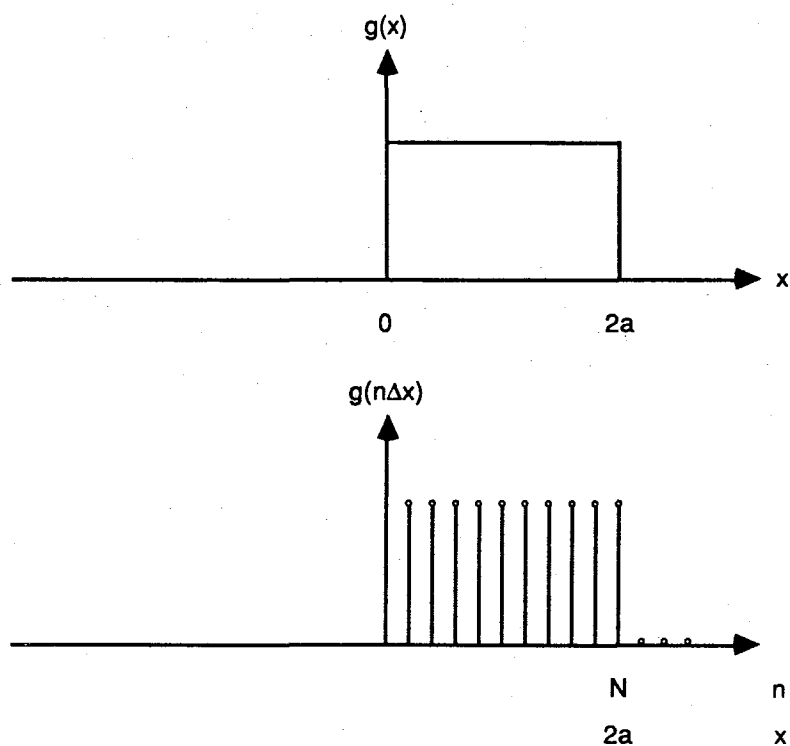


Figure B3. A Causal Function $g(x)$ and its Sampled Version $g(n\Delta x)$

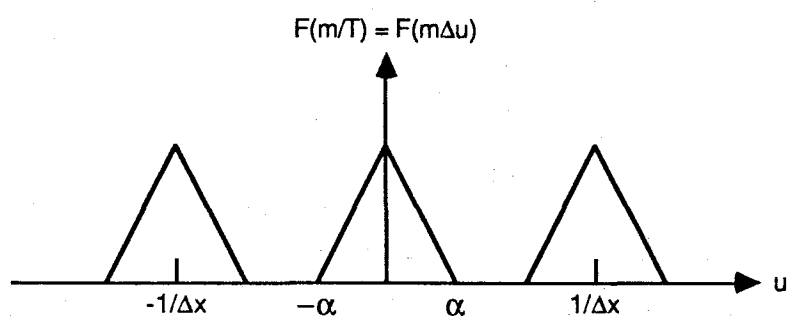


Figure B4. A Fourier Transform and its Neighboring Aliases

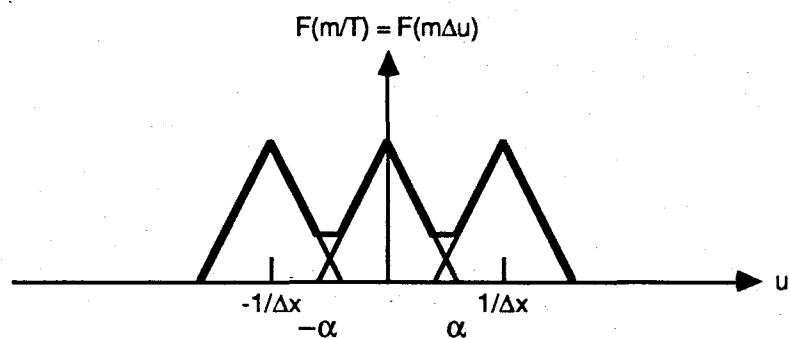


Figure B5. The Effects of Aliasing Error on a Fourier Transform Due to Large Sample Size Δx